e-ISSN: 2757-9077

Open Access

ENGINEERING PERSPECTIVE

CONTENTS

ENGINEERING PERSPECTIVE

Volume: 5 Issue: 1 31 March 2025

ENGINEERING PERSPECTIVE

An International Journal

Volume: 5 Issue: 1 31 March 2025

https://sciperspective.com

e-ISSN: 2757-9077 Open Access

ENGINEERING PERSPECTIVE

An International Journal

Volume: 5	Issue: 1	31 March 2025
Engineering Perspective publishes **four issues** per year.		

Correspondence Address :
Gazi University, Faculty of Technology, Department of Automotive Engineering, Teknikokullar - Ankara, TURKIYE

e-mail: engineering@sciperspective.com

Technical Editor:
Regaip Menküç
Gazi University

Layout Editors:
İrem Tanış, Gazi University
Zehra Ebrar Ağca, Gazi University

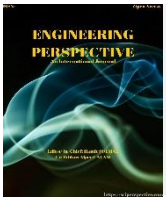

e-ISSN:2757-9077

ENGINEERING PERSPECTIVE

https://sciperspective.com/ Research Paper

Working Fluid Selection and Performance Analysis for the Afyon Geothermal Energy Plant

Ömer Faruk Güler[1*]

[1] *Mechanical Engineering Department, Faculty of Technology, Afyon Kocatepe University, Afyonkarahisar, 03200, Türkiye*

ABSTRACT

Renewable energy production has been steadily increasing in recent years. Generating energy from renewable sources and making them operational for use is essential. Alongside production, efficiently utilizing these resources is equally important. For efficient use, exploring various alternatives and conducting optimization processes are crucial. Organic Rankine Cycles (ORCs) allow energy production from low-enthalpy temperature sources. By using working fluids with low boiling points, it is possible to create a Rankine cycle at low temperatures. Each system operates under unique regional and environmental conditions, so careful selection of working fluids is necessary. Factors such as heat source temperature and pressure, ambient pressure and temperature, location, and purpose of use cause different fluids to exhibit varying behaviors. In this study, the effects of different working fluids were examined for the Afyon geothermal power plant. The active plant utilizes geothermal water at 110°C and a flow rate of 150 kg/s. The plant's capacity is approximately 2.7 MW. R-134a, a widely used working fluid, serves as the intermediary fluid. Additionally, fluids such as isopentane, n-pentane, isobutane, R-12, and R-32 were tested. Thermodynamic and thermoeconomic analyses of the system were conducted using these fluids. With R-134a, 2.75 MW of power was generated at a unit energy cost of $0.025/kWh. Among the alternative fluids, isobutane produced 2.95 MW of power with a unit energy cost of $0.016/kWh. The energy efficiencies of the system for R-134a and isobutane were 10.9% and 11.6%, respectively. Similarly, the exergy efficiencies for these fluids were 31.1% and 33.1%, respectively. Although better results can be achieved with certain alternative fluids, the data are insufficient to directly replace the current working fluid in the system. Performing a separate optimization study with these promising fluids will be a critical step in determining the final working fluid.

Keywords: Geothermal Energy; ORC; Thermo-Economic Analysis; Working Fluid Selection

History
Received: 04.05.2024
Accepted: 26.11.2024

Author Contacts
**Corresponding Author*
e-mail addresses : ofguler@aku.edu.tr,

How to cite this paper: Güler, Ö.F. (2025). Working Fluid Selection and Performance Analysis for the Afyon Geothermal Energy Plant. Engineering Perspective, 5 (1), 1-8. http://dx.doi.org/10.29228/eng.pers.80205

1. Introduction

Energy efficiency and renewable energy applications have made significant progress. These advancements, particularly in the efficient use of renewable resources for maximum utilization. Also, they are continuing to grow. One of these is the Organic Rankine Cycle (ORC). ORC enables the use of low-enthalpy energy sources. These sources may include waste heat from a heat-utilizing facility or heat derived from a renewable source such as solar or geothermal energy. Historically, high-enthalpy geothermal resources were the first to be utilized in Rankine Cycles [1]. Later, the idea of harnessing low-enthalpy sources led to the use of alternative working fluids instead of water vapor in Rankine cycles. These fluids, with lower boiling point temperatures, have rapidly increased the exploitation of low-temperature renewable resources. Organic fluids are used as the working medium in such systems. Various fluid types exist, each with diverse thermophysical properties. Choosing the most suitable working fluid for each system is important, and the literature includes various studies on this topic.

Optimizing waste heat recovery is an important research area for making renewable energy resources more productive. The working fluids used in ORC systems significantly influence system efficiency, environmental impact, and economic performance. Comparing different working fluids is thus a vital step toward improving ORC energy plant performance. Many studies emphasize using low-global warming potential (GWP) working fluids to reduce environmental impacts. Wang et al. [2] compared the thermodynamic performance of various low-GWP fluids used in ORC systems and highlighted the advantages of these fluids in recovering low-temperature waste

heat. They noted that fluids such as R245fa and isopentane are more environmentally friendly options [3]. Additionally, the use of fluid mixtures has been shown to provide more efficiency compared to pure fluids. These mixtures enable higher energy production and greater exergy efficiency in ORC systems while improving electricity generation costs.

Some of the other researches focus on Multi-objective optimization of the energy plant. Multi-objective optimization processes are employed to make ORC systems more economically and environmentally efficient. These optimizations are try to enhance both thermodynamic efficiency and economic performance. For instance, Li et al.[4] investigated the integration of LNG cold energy and geothermal energy to enhance ORC system performance, achieving a 43.3% efficiency improvement through multi-objective optimization. Such optimization processes improve the design and operational parameters of systems.

Another important application is the integration of ORC systems into reversible heat pump systems. These systems, often utilizing multiple energy sources, both hot and cold, offer multipurpose applications to improve heat recovery efficiency. For example, Daniarta et. al. [5] offer an ORC system integrated with a reversible heat pump that demonstrated significant efficiency improvements, depending on system design and working fluid selection. These kinds of systems are particularly effective in reducing energy production costs by utilizing waste heat recovery and low-temperature sources, as for example achieving energy savings of up to 50%, according to this study.

In optimizing ORC system performance, choosing working fluid plays an important role. Xia et al. [6] used multi-objective optimization approaches to analyze the performance of ORC-VCR (Organic Rankine Cycle-Vapor Compression Refrigeration) systems. They tried to demonstrate the significant impact of fluid mixtures on system efficiency. These studies also identified the necessary parameters for enhancing ORC systems' efficiency under different temperature and pressure conditions. Furthermore, economic performance analyses of ORC systems with various fluids are a major research area. Feng et al. [7] examined ORC systems in an economical way. They explained how fluid selection affects electricity generation and cost. They showed that fluid mixtures offer more cost-effective solutions than pure fluids, reducing energy generation costs. Similarly, Liang et al. [8] optimized ORC cycles in thermal integrated pumped thermal energy storage (TIPTES) systems using different working fluids, ultimately selecting the most suitable fluid for their system. They used R-245fa, Isobutane, Isopentane, MM and R1336mzz(Z)— as a working fluid. Similarly, in their study, Rachmat and colleagues [9] aimed to propose a new configuration for Unit 2 of the Wayang Windu geothermal power plant by integrating a double-flash separator with an ORC system. The analysis, conducted using R245fa as the working fluid, was evaluated both thermodynamically and economically and compared with the existing system. As a result of the optimization, the exergy efficiency was found to be 54.40%, the specific cost $1.86/GJ, and the payback period 0.32 years. This configuration offers some improvements over the existing system in both thermodynamic and economic terms. Also, another research topic is the optimization of hybrid systems. The hybrid systems integrate different energy sources or different power cycles. Li et al. [4] demonstrated the effectiveness of multi-objective optimizations in such hybrid systems by investigating ORC and LNG cold energy integration. These hybrid systems enhance the efficiency of the system, thus providing environmental and economic benefits.

Optimizing an ORC can help reduce the environmental side effects of energy plants. Hou et al. [10] optimized ORC technology for low-temperature waste heat recovery in ammonia synthesis plants, reducing cyclical water consumption and improving exergy performance. With optimal conditions, exergy efficiency increased by 35.53%, electricity production costs decreased by $0.043, and annual CO_2 emissions were reduced by 3,736.30 tons.

As a result, the importance of optimization studies cannot be ignored, as they have the potential to enhance the efficiency of ORC systems through improved system design and parameter adjustments. Exergoeconomic analyses are also valuable for optimizing both energy efficiency and economic performance. Numerous studies predict that the methods employed to improve the economic and environmental performance of ORC systems will increase their applicability in future projects [11].

Afyonkarahisar province is abundant in geothermal energy. Electricity is generated from the geothermal power plant established in the region. Lately, researchers have conducted various analyses of this power plant. Şahin performed the thermodynamic analysis of the Afyon geothermal power plant, which uses an ORC with R-134a as the working fluid [12]. Yılmaz later conducted a similar analysis of the same plant, modeling with three different working fluids: R-134a, n-Pentane, and Isobutane [13]. In another study, he used the results of his previous work and suggested that optimization could be achieved [14]. He tried to explain plant characteristics with some parametric results. However, the analysis of the fluids was not explored in detail in Yılmaz's studies. Building on these valuable contributions, the current study investigates the effects of different working fluids. Six different working fluids were tested: R-134a, Isopentane, n-Pentane, R-12, Isobutane, and R-32. The pressure and temperature values were carefully selected based on the properties of each fluid. The evaporation temperature was adjusted to be as close as possible to the maximum temperature achievable in the heat exchanger, while the condensation temperature was brought as close as possible to the cooling water temperature. This approach allows for a clearer assessment of the newly tested working fluids. The ability of these systems to adapt to a broader range of applications is crucial for achieving future energy transformation and sustainability goals.

2. Method

The thermodynamic model of the existing geothermal power plant in Afyonkarahisar province will be developed, and detailed analyses of this model will be conducted. Initially, a schematic representation of the power plant will be created, highlighting the essential components. Subsequently, calculations related to these components will be presented separately, addressing both thermodynamic and economic aspects. These are grouped under three subheadings; system description, thermodynamic analysis, thermo-economic analysis.

2.1 System description

The system consists of an ORC cycle stream, a geothermal water flow, and a cooling water flow. The ORC cycle includes a turbine, a condenser, a heat exchanger, and a pump.

Cooling water is used in the condenser, matching the current

power plant's data. The use of water ensures stable cooling at a constant temperature throughout the year, unlike air-cooled systems, which consume more energy. The region experiences significant temperature differences between summer and winter, as well as day and night. Using air for cooling creates additional challenges due to fluctuating temperatures. During the summer, when temperatures rise, the efficiency of the plant already operating at low temperatures can drop significantly with air cooling.

The system's heat input comes from a geothermal source. Although the source temperature varies slightly depending on the wells, it averages around 110°C. The water flow rate is 150 kg/s. Due to the high mineral content and low enthalpy of the water, direct usage is not feasible. Instead, a heat exchanger is used to transfer heat into the system. With the current setup, a temperature difference of 10°C (K) is achieved to transfer this heat in heat exchanger.

A pump is used to maintain system pressure, and a turbine is included for energy generation. The isentropic efficiencies of the turbine and pump are considered as 85% in calculations [15].

A schematic diagram of the system is presented in Figure 1. In the diagram, the red stream represents geothermal water, the green stream indicates the organic fluid flow, and the blue stream shows the cooling water flow. The system is modeled and analyzed as control volumes, with each control volume assigned a state number. The states are defined as follows: between the pump and condenser (1), between the pump and heat exchanger (2), between the heat exchanger and turbine (3), at the turbine outlet and condenser inlet (4), geothermal water inlet (5), geothermal water outlet from the heat exchanger (6), and cooling water inlet and outlet (7 and 8, respectively).

The analyses are divided into two main sections: thermodynamic and exergoeconomic analyses. The thermodynamic analysis includes energy and exergy assessments for each control volume. The exergoeconomic analysis builds on the thermodynamic results to perform economic evaluations.

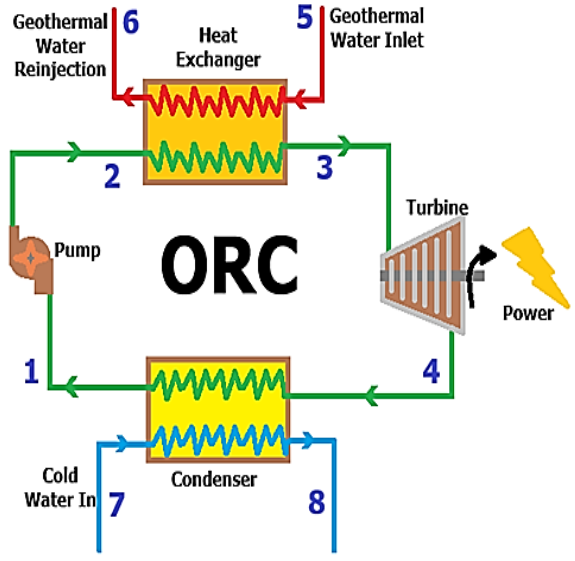

Figure 1. Schematic diagram of Afyon Geothermal Plant

2.2 Thermodynamic Analysis

In the thermodynamic analyses, energy and exergy calculations were performed for each component. EES software was used to perform these analyses. The energy equations for the equipment in the system, such as the pump, heat exchanger, turbine, and condenser, are presented sequentially according to their system state numbers.

The work required for pumping is calculated using Equation (1) [16].

$$\dot{w}_p = \frac{v_1 (P_2 - P_1)}{\eta_p} \quad (1)$$

After calculating pump work, h_2 value can be calculated be calculated by adding this work to h_1, as in Equation (2) [16].

$$h_2 = h_1 + \dot{w}_p \quad (2)$$

Enthalpy equity can be written for the heat transferred in heat exchanger like in Equation (3) [16].

$$m_{geo} (h_5 - h_6) = m_{wf} (h_3 - h_2) \quad (3)$$

Turbin work is calculated according to isentropic efficiency of the turbine (Equations (4),(5)) [16].

$$\dot{w}_T = h_3 - h_4 \quad (4)$$

$$\eta_T = \frac{\dot{w}_T}{\dot{w}_{T,iso}} = \frac{h_3 - h_4}{h_3 - h_{4,s}} \quad (5)$$

Finally, cycle waste heat is removed from the condenser. In Eqn. (6), again, the calculation is made like the heat exchanger [16].

$$m_{water} (h_8 - h_7) = m_{wf} (h_4 - h_1) \quad (6)$$

The exergy of a flow is calculated as in Equations (7) and (8) [16].

$$ex_i = (h_i - h_0) - T_0 (s_i - s_0) \quad (7)$$

$$\dot{Ex}_i = \dot{m}_i . ex_i \quad (8)$$

2.3 Thermo-economic analysis

In the economic analysis, the annual operating time is assumed to be 7,200 hours, equivalent to approximately 300 days of activity per year. The total lifespan of the facility is considered to be 10 years. An interest rate of 5% and maintenance and operating costs of 6% are assumed.

The cost recovery factor is calculated using the following Egn. (9) [17].

$$CRF = \frac{i.(i+1)^n}{(i+1)^n - 1} \quad (9)$$

The annual levelized cost of a component is found with Equation. (10) [17].

$$\dot{Z}_{CI,k} = CRF.C_{I,k} \quad (10)$$

Similarly, maintenance and repair costs are found from Equation (11) [17].

$$\dot{Z}_{OM,k} = CRF.C_{I,k}.\varphi \quad (11)$$

The total component levelized cost is found by the Equation (12) [17].

$$\dot{Z}_{Total,k} = \dot{Z}_{OM,k} + \dot{Z}_{CI,k} \quad (12)$$

The cost of a flow is obtained by multiplying the unit exergy cost of the flow by the exergy (Equation (13) [17].

$$\dot{C}_i = E\dot{x}_i.c_i \quad (13)$$

For any component, when the exergy flows entering and leaving the component, as well as the component-specific cost, are included, the economic equation takes the form of Equation (14). Its schematic can be seen in Figure 2. Here, there may be multiple inlets and outlets. For example, a heat exchanger has two inlet streams and two outlet streams. However, the method of the calculation will not change. The input costs and component costs will be written on one side, while the output costs will be written on the other side of the equation [17].

$$\dot{C}_{i,inlet} + Z_{Total,k} = \dot{C}_{i,outlet} \quad (14)$$

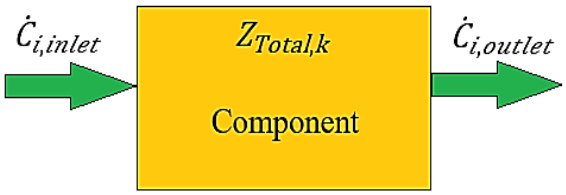

Figure 2. Economic analysis of a component

The cycle components can be adapted individually to Eguation (14). When applied to the pump, Equation (15) is obtained. Here, the $\dot{C}_1$ value used in the calculation of the c_1 value is determined based on the cost of the working fluid. Various values for different working fluids are available in the literature. However, most of these values exhibit variability. To avoid a significant manipulation on the unit cost, an average value of 6 $/GJ, which is the same for all fluids, has been adopted. This value largely reflects the cost data for all fluids [17].

$$\dot{C}_1 + Z_{Total,Pump} = \dot{C}_2 \quad (15)$$

When a similar calculation is performed for the heat exchanger, Equation (16) is obtained. In this case, there are two inputs and two outputs, with one of the inputs being the geothermal cost. This cost value has been updated to the present day in line with the literature and is accepted as 1.6 $/GJ. The geothermal energy output cost is assumed to be c_6=c_5. Since the flow remains unchanged, the exergy cost also remains the same. The value of c_2 is known, and c_3 will be calculated.

$$\dot{C}_5 + \dot{C}_2 + \dot{Z}_{Total,HEX} = \dot{C}_3 + \dot{C}_6 \quad (16)$$

For the turbine, the calculation follows a similar approach, leading to Equation (17) [18]. In this scenario, there is one input and two outputs. One of the outputs here is the electricity cost. The c_3 stream is known, and as in the heat exchanger, $c_3 = c_4$ is assumed since the stream remains unchanged. The unit cost of the output power ($c_{electric}$) is calculated.

$$\dot{C}_3 + \dot{Z}_{Total,Turbine} = \dot{C}_4 + W_{net}.c_{electric} \quad (17)$$

The final component is the condenser, where the unit exergy cost calculation is performed. This component is essentially a type of heat exchanger [18]. The value of c_1 serves as the starting point and is constant. Since the entering cooling water is at ambient conditions, its exergy cost is considered zero. In reality, this water does have a cost, but since it has zero exergy, it is assumed to be zero. The exergy cost of the output, however, is assumed to be the same as the electrical exergy. In this way, the cost of the discharged exergy is represented in parallel with the work produced.

$$\dot{C}_4 + \dot{C}_7 + \dot{Z}_{Total,Condenser} = \dot{C}_1 + \dot{C}_8 \quad (18)$$

The initial investment costs of the components are determined in proportion to their sizes using Equations (19), (20), and (21) below. The condenser and evaporator are considered two heat exchangers with similar flow configurations. For these systems, the heat transfer coefficient of the heat exchanger is assumed to be 0.25 kW/m², and the required areas are calculated accordingly.

$$\dot{Z}_{CI,Pump} = 1120\left(w_p\right)^{0.8} \quad [19] \quad (19)$$

$$\dot{Z}_{CI,Turbine} = 4405\left(w_T\right)^{0.7} \quad [20] \quad (20)$$

$$\dot{Z}_{CI,HEX} = 2681\left(A_{HEX}\right)^{0.59} \quad [21] \quad (21)$$

3. Results and discussions

Both thermodynamic and thermo-economic analyses were conducted, and for each case, the thermodynamic properties and unit exergy costs of the working fluids were calculated. The phase table for R-134a, the first of these fluids, is provided in Table 1. The system operates with a working fluid flow rate of 108 kg/s and a turbine inlet pressure of 2800 kPa. The condenser pressure is 500 kPa, and the cooling water flow rate in the condenser is calculated as 525.6 kg/s.

Table 1. R-134a state-property table

	m (kg/s)	T (K)	P (kPa)	h (kj/kg)	s (kJ/kg.K)	c ($/GJ)
1	108	288.9	500	73.328	0.2802	6.00
2	108	290.2	2800	75.509	0.2814	6.30
3	108	373.3	2800	309.324	0.9652	4.21
4	108	307.5	500	277.132	0.9838	4.21
5	150	383.1	143.3	461.331	1.4190	1.60
6	150	343.1	143.3	292.984	0.9549	1.60
7	525.6	284.1	100	46.228	0.1656	0.00
8	525.6	294.1	100	88.106	0.3104	6.94

Another fluid planned for use in the system is isopentane. The phase properties of this fluid are provided in Table 2. The turbine inlet pressure has been updated in parallel with the evaporation point. This adjustment aims to select the highest possible pressure that can be achieved by evaporating the geothermal water at 383 K using a heat exchanger. A value of 710 kPa has been accepted as the high pressure. In the developed model, the pinch temperature for the heat exchanger has also been calculated, ensuring the temperature variation curves for the heat exchanger are accurately formed. Similarly, the condenser inlet pressure has been modified and adjusted to suit the fluid, with 90 kPa being accepted as the low pressure. The working fluid flow rate corresponding to all these values is taken as 54.8 kg/s. The temperature, enthalpy, entropy, and unit exergy costs appropriate for these conditions can be obtained from the table. The condenser cooling water flow rate is calculated as 520.6 kg/s.

Table 2. Isopentane state-property table

	m (kg/s)	T (K)	P (kPa)	h (kj/kg)	s (kJ/kg.K)	c ($/GJ)
1	54.8	297.6	90	-351.240	-1.6940	6.00
2	54.8	297.9	710	-350.054	-1.6930	12.77
3	54.8	373.1	710	110.749	-0.4007	2.22
4	54.8	327.5	90	46.596	-0.3658	2.22
5	150	383.1	143.3	461.331	1.4190	1.60
6	150	343.1	143.3	292.984	0.9549	1.60
7	520.6	284.1	100	46.228	0.1656	0.00
8	520.6	294.1	100	88.106	0.3104	0.57

A phase property table for n-Pentane has been created. Within this temperature range, n-Pentane operates at lower pressures than other fluids. The turbine inlet pressure is set at 550 kPa, and the condenser inlet pressure is taken as 80 kPa. At a pressure of 80 kPa, the saturation temperature is sufficiently far from the pinch point temperature. Although it is technically possible to further reduce the pressure for n-pentane, operation under high vacuum conditions has not been deemed practical. In practice, while there are power plants operating under vacuum conditions, extremely high vacuum pressures were not considered for this case. The working fluid mass flow rate is assumed to be 53 kg/s. Data set was calculated and showed in Table 3. The condenser water inlet flow rate is calculated as 526.6 kg/s according to these assumptions.

Table 3. n-Pentane state-property table

	m (kg/s)	T (K)	P (kPa)	h (kj/kg)	s (kJ/kg.K)	c ($/GJ)
1	53	302.2	80	7.427	0.0257	6.00
2	53	302.5	550	8.324	0.0261	12.04
3	53	373	550	484.776	1.3610	2.22
4	53	332	80	423.551	1.3930	2.22
5	150	383.1	143.3	461.331	1.4190	1.60
6	150	343.1	143.3	292.984	0.9549	1.60
7	526.6	284.1	100	46.228	0.1656	0.00
8	526.6	294.1	100	88.106	0.3104	4.73

When a state and thermodynamic property table is created for the refrigerant R-12, Table 4 is obtained. The turbine inlet pressure and condenser inlet pressure are set at 3200 kPa and 670 kPa, respectively. The working fluid mass flow rate is determined to be 166 kg/s, while the condenser cooling water flow rate is calculated as 528 kg/s.

Table 4. R-12 state-property table

	m (kg/s)	T (K)	P (kPa)	h (kj/kg)	s (kJ/kg.K)	c ($/GJ)
1	166	299.2	670	60.712	0.2272	6.00
2	166	301.5	3200	62.989	0.2347	6.68
3	166	373	3200	215.110	0.6599	4.20
4	166	299.2	670	193.911	0.6724	4.20
5	150	383.1	143.3	461.331	1.4190	1.60
6	150	343.1	143.3	292.984	0.9549	1.60
7	528	284.1	100	46.228	0.1656	0.00
8	528	294.1	100	88.106	0.3104	6.91

R-32 is another refrigerant tested in the system. The optimal pressure range for R-32 is between 1600 kPa and 5400 kPa, which is higher compared to most other fluids. The boiling point at the same pressure is considerably lower than that of other fluids. The working fluid mass flow rate is 84 kg/s, and the condenser cooling water flow rate is calculated as 537.7 kg/s. All these detailed results are provided in Table 5.

Table 5. R-32 state-property table

	m (kg/s)	T (K)	P (kPa)	h (kj/kg)	s (kJ/kg.K)	c ($/GJ)
1	84	296.1	1600	241.736	1.1440	6.00
2	84	299.1	5400	246.348	1.1460	6.68
3	84	372.8	5400	546.967	2.0270	4.20
4	84	296.1	1600	509.794	2.0490	4.20
5	150	383.1	143.3	461.331	1.4190	1.60
6	150	343.1	143.3	292.984	0.9549	1.60
7	537.7	284.1	100	46.228	0.1656	0.00
8	537.7	294.1	100	88.106	0.3104	8.11

Isobutane is the final working fluid proposed for use in the system. The state-property results of this fluid can be obtained from Table 6. The turbine inlet pressure is set at 1900 kPa, and the condenser inlet pressure is 300 kPa. The working fluid mass flow rate in the cycle is 58.5 kg/s, and the cooling water mass flow rate is calculated as 519.9 kg/s.

Table 6. Isobutane state-property table

	m (kg/s)	T (K)	P (kPa)	h (kj/kg)	s (kJ/kg.K)	c ($/GJ)
1	58.5	292.9	300	246.725	1.1640	6.00
2	58.5	293.9	1900	250.108	1.1660	6.40
3	58.5	372.9	1900	681.766	2.3950	3.42
4	58.5	313.7	300	618.906	2.4300	3.42
5	150	383.1	143.3	461.331	1.4190	1.60
6	150	343.1	143.3	292.984	0.9549	1.60
7	519.9	284.1	100	46.228	0.1656	0.00
8	519.9	294.1	100	88.106	0.3104	5.89

Based on the data from the tables arranged for all these different fluids, the net energy and unit energy costs have been calculated separately. Additionally, the system's energy and exergy efficiencies are also presented. All these systems can be compared in Table 7. The systems that generate the most energy is those using isopentane and isobutane. The lowest unit energy cost is achieved with isopentane. Systems using either isobutane or isopentane stand out in terms of both energy and exergy efficiency. These results are consistent with those found by Yılmaz [13,14]. A very close value of 2.75 MW was obtained for R-134a.

Table 7. Comparative results, net power output, unit cost of energy, energy and exergy efficiency

	Net Power (kW)	Unit Cost of Energy ($/kWh)	Energy Effciency (%)	Exergy Effciency (%)
R-134a	2755	0.02497	10.91	31.09
Isopentane	2933	0.01644	11.61	33.10
N-Pentane	2718	0.01702	10.76	30.67
R-12	2670	0.02487	10.57	30.13
Isobutane	2958	0.02120	11.71	33.37
R-32	2325	0.02922	9.21	26.24

Fluctuations in geothermal water temperature can occur from time to time. Through parametric analysis, the response of the fluids to changing geothermal water temperatures can be observed. The first data to be examined in the parametric analysis is the graph showing the variation of net energy produced with changing geothermal water temperature. The graph created for six different fluids is shown in Figure 3. The geothermal water temperature ranges from 373 K to 403 K. As the geothermal water temperature increases, the net energy output also increases. On the left side of the graph, between 373-383 K, isobutane and isopentane are at the top. In the 383-395 K range, isobutane is at the highest position. At higher temperatures, R-12 generates the most energy.

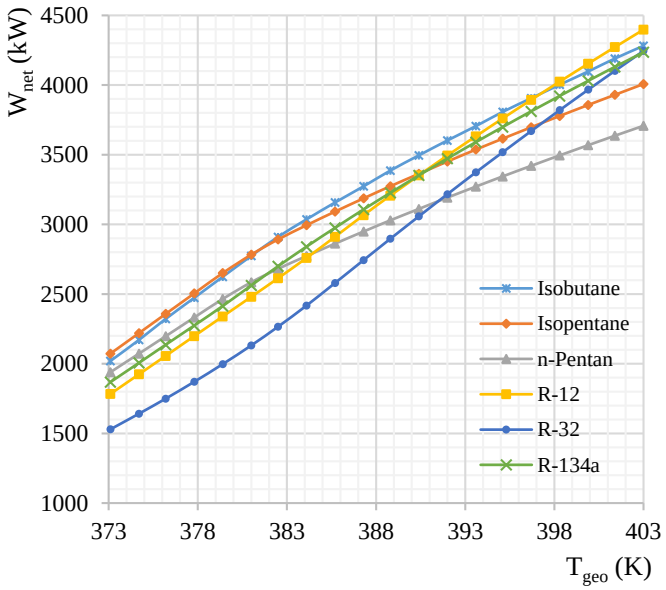

Figure 3. Net Energy Output of the Power Plant Versus Varying Geothermal Water Temperature

A similar graph has been created for the cost analysis. The variation of unit electricity cost with changing geothermal water temperature for different fluids can be observed in the graph in Figure 4. In this graph, the lowest cost is achieved with isopentane and n-pentane, while the highest cost is obtained with R-32.

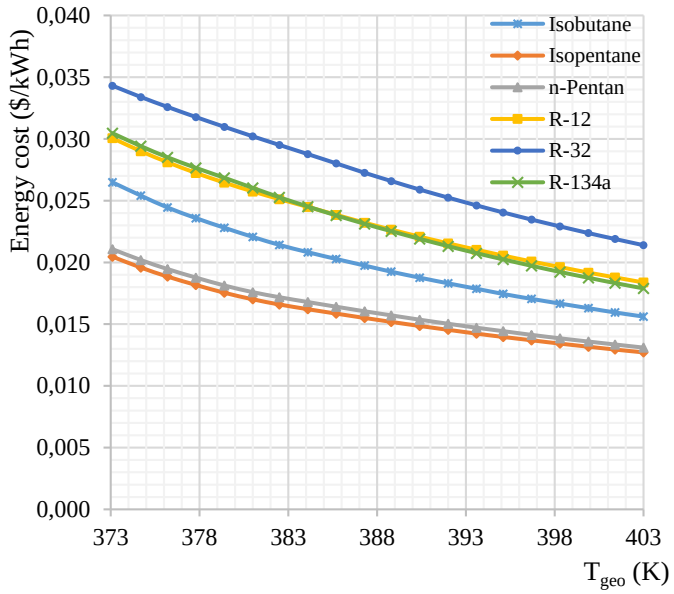

Figure 4. Unit Energy Cost Versus Varying Geothermal Water Temperature

4. Conclusions

The study investigates how different fluids react within the operational range for potential use in the Afyon geothermal power plant. R-134a is an actively used fluid. Additionally, fluids like isopentane, n-pentane, isobutane, R-12, and R-32, which can operate at similar

temperatures, were evaluated for the model.

Isobutane ranks among the top performers across all temperature values. Fluids with lower mass flow rates and smaller pressure differences appear more efficient, producing more energy. Moreover, as the mass flow decreases, costs are reduced. However, as the mass flow rate decreases, the system's sensitivity increases significantly, leading to larger responses to minor changes and fluctuations. This highlights the necessity for highly precise control units in real-world system designs.

R-134a, the fluid currently in use, provides an average response. Its performance data are not at the extremes for either mass flow or operating pressures compared to other fluids. However, geothermal water wells in the region with higher temperatures (~430 K) are occasionally encountered. If the system is modified for slightly higher temperatures, fluids like R-12 and R-32 could be considered. Furthermore, fluids like R-245fa could also be tested. This study is expected to guide future modification plans. However, detailed optimization for each fluid is essential if deemed necessary.

In this study, evaporation and condensation temperatures were kept as close to the limits as possible. However, greater energy production could be achieved by optimizing intermediate temperatures, which could be a significant step for better decision-making and system improvement in the future. clarity of all figures is extremely important.

Nomenclature

A_{HEX}	Heat exchanger Area
$\dot{c}_i$	Unit cost of exergy flow per mass
$\dot{C}$	Total cost of exergy flow
CRF	Cost recovery factor
$e\dot{x}$	Exergy flow per mass flow rate
$E\dot{x}$	Exergy of a flow
η_p	Pump isentropic efficiency
η_T	Turbine isentropic efficiency
h_i	Enthalpy of i-th state
i	Interest rate
$\dot{m}_i$	Mass flow rate of i-th state
n	Number of period
ORC	Organic rankine cycle
P_i	Pressure of the i-th state
φ	Maintenance factor
v_i	Specific volume
$\dot{w}_P$	Pump work
$\dot{w}_T$	Turbine work

Subscript

geo	Geothermal
k	Component
s	Entropi
iso	Isontropic
wf	Working fluid

Conflict of Interest Statement

Author declares that there is no conflict of interest in the study.

References

1. Lund, J. W., Huttrer, G. W., & Toth, A. N. (2022). Characteristics and trends in geothermal development and use, 1995 to 2020. Geothermics, 105, 102522. https://doi.org/10.1016/j.geothermics.2022.102522
2. Wang, E. H., Zhang, H. G., Fan, B. Y., Ouyang, M. G., Zhao, Y., & Mu, Q. H. (2011). Study of working fluid selection of organic Rankine cycle (ORC) for engine waste heat recovery. Energy, 36(5), 3406-3418. https://doi.org/10.1016/j.energy.2011.03.041
3. Liu, Y., Sun, W., & Liu, X. (2024). Greening the organic Rankine cycles: low-global warming potential working fluids for low-temperature waste heat recovery. International Journal of Exergy, 45(1-2), 126-143. https://doi.org/10.1504/IJEX.2024.141686
4. Li, B., Xie, H., Sun, L., Gao, T., Xia, E., Liu, B., ... & Long, X. (2024). Advanced exergy analysis and multi-objective optimization of dual-loop ORC driven by LNG cold energy and geothermal energy. Renewable Energy, 122164. https://doi.org/10.1016/j.renene.2024.122164
5. Daniarta, S., Imre, A. R., & Kolasiński, P. (2024). A novel approach to district heating: using a two-phase expander in reversible heat pump-Organic Rankine Cycle system. In Proceedings of the 7th International Seminar on ORC Power System:(ORC2023) (pp. 169-175). Editorial Universidad de Sevilla. https://dx.doi.org/10.12795/9788447227457
6. Xia, X., Zhang, H., Wang, Z., Yang, C., Sun, T., & Peng, B. (2024). Performance comparison of two ORC-VCR system configurations using pure/mixture working fluids based on multi-objective optimization. Applied Thermal Engineering, 255, 124027. https://doi.org/10.1016/j.applthermaleng.2024.124027
7. Feng, J., Yan, Y., Zhao, L., & Dong, H. (2024). Energy, Exergy, and Economic Performance Comparison and Parametric Optimization of Organic Rankine Cycles Using Isobutane, Isopentane, and Their Mixtures for Waste Heat Recovery. Energies (19961073), 17(23). https://doi.org/10.3390/en17235893
8. Liang, Z., Zheng, G., Wu, G., Pan, Z., Hu, Z., Xu, M., & Chen, H. (2024). Thermodynamic performance of organic Rankine cycle based pumped thermal energy storage system with different working fluids. Heliyon. https://doi.org/10.1016/j.heliyon.2024.e41052
9. Rachmat, A., Pansawati, I. S., Agustin, Y., Surachman, A., Sutardi, T., & Suyanto, S. (2024, November). Multi-Objective optimization of a combined double flash–Binary cycle for Wayang Windu geothermal power plant based on exergy and economics. In AIP Conference Proceedings (Vol. 3215, No. 1). AIP Publishing. https://doi.org/10.1063/5.0235648
10. Hou, Z., Imechoui, I., Chong, P. L., Guo, P., Deng, Y., & Gao, Y. (2024). Enhancing exergy and economical performance of a waste heat power generation system: Multi-objective optimization and comparative analysis. Journal of Cleaner Production, 482, 144235. https://doi.org/10.1016/j.jclepro.2024.144235
11. Özcan, Z., & Ekici, Ö. (2021). A novel working fluid selection and waste heat recovery by an exergoeconomic approach for a geothermally sourced ORC system. Geothermics, 95, 102151. https://doi.org/10.1016/j.geothermics.2021.102151
12. Şahin, C. (2016). Düşük sıcaklıklı jeotermal sahalarda organik rankin çevrimi (ORC) ile elektrik enerjisi üretiminde Afyon Jeotermal Elektrik Üretim AŞ modellemesi (Master's thesis, Fen Bilimleri Enstitüsü).

13. Yılmaz, C. (2020). Performance Evaluation of Afyon Geothermal Power Plant with Low Grade Energy Sources. Konya Journal of Engineering Sciences, 8(3), 448-465. https://doi.org/10.36306/konjes.627174
14. Yılmaz, C. (2020). Improving performance and thermoeconomic optimization of an existing binary geothermal power plant: A case study. Isı Bilimi ve Tekniği Dergisi, 40(1), 37-51.
15. Sen, O., Guler, O. F., Yilmaz, C., & Kanoglu, M. (2021). TherModynamic Modeling and Analysis of a Solar and Geothermal Assisted Multi-Generation Energy System. Energy Conversion and Management, 239, 114186. https://doi.org/10.1016/j.enconman.2021.114186
16. Cengel, Y. A., Boles, M. A., & Kanoğlu, M. (2011). *Thermodynamics: an engineering approach* (Vol. 5, p. 445). New York: McGraw-hill.
17. Bejan, A., Tsatsaronis, G., & Moran, M. J. (1995). Thermal design and optimization. John Wiley & Sons.
18. Guler, O. F., Sen, O., Yilmaz, C., & Kanoglu, M. (2022). Performance evaluation of a geothermal and solar-based multigeneration system and comparison with alternative case studies: Energy, exergy, and exergoeconomic aspects. Renewable Energy, 200, 1517-1532. https://doi.org/10.1016/j.renene.2022.10.064
19. Özahi, E., & Tozlu, A. (2020). Optimization of an adapted Kalina cycle to an actual municipal solid waste power plant by using NSGA-II method. Renewable Energy, 149, 1146-1156. https://doi.org/10.1016/j.renene.2019.10.102
20. Mahmoudi, S. M. S., Pourreza, A., Akbari, A. D., & Yari, M. (2016). Exergoeconomic evaluation and optimization of a novel combined augmented Kalina cycle/gas turbine-modular helium reactor. Applied Thermal Engineering, 109, 109-120. https://doi.org/10.1016/j.applthermaleng.2016.08.011
21. Mosaffa, A. H., Mokarram, N. H., & Farshi, L. G. (2017). Thermoeconomic analysis of a new combination of ammonia/water power generation cycle with GT-MHR cycle and LNG cryogenic exergy. Applied Thermal Engineering, 124, 1343-1353. https://doi.org/10.1016/j.applthermaleng.2017.06.126

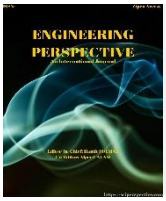

e-ISSN:2757-9077

ENGINEERING PERSPECTIVE

https://sciperspective.com/ Research Paper

Magnetocaloric Cooling for Hybrid/Hydrogen and Electric Vehicle Cabin and Powertrain Components

Mohand Ouyahia Bousseksou[1*], Kamal Nouri[1], Thomas Bartoli[1], Wassim Bouzidi[1], Lotfi Bessais[2]

[1]*Capgemini engineering, Ile de France, Division APA, 12 rue de la Verrerie, 92190 Meudon, France*
[2]*CNRS-UPEC, Université Paris Est, ICMPE (UMR 7182), F-94320 Thiais, France*

ABSTRACT

The magnetocaloric cooling system is a promising alternative to traditional refrigeration systems that rely on the compression and expansion of harmful refrigerant gases. Utilizing the magnetocaloric effect, these systems can efficiently provide heating and cooling for a wide range of applications. One particularly significant application of this technology is in the air conditioning of electric vehicles and the thermal management of powertrain components.

This study presents a Matlab Simulink model of the powertrain, alongside a COMSOL model of the permanent magnet, specifically designed for hybrid and electric car applications. The Matlab Simulink model simulates the dynamic behavior of the vehicle's powertrain, integrating the magnetocaloric cooling system to analyze its impact on performance and efficiency. This allows for a comprehensive evaluation of how the system can improve energy efficiency and thermal regulation in electric vehicles. Additionally, the COMSOL model focuses on the detailed behavior of the permanent magnet used in the magnetocaloric cooling system. This model provides insights into the magnetic field distribution and its interaction with the magnetocaloric materials, which are critical for optimizing the cooling cycle and enhancing overall system performance.

To ensure the accuracy and reliability of the simulations, some interpolated experimental data were used. This data helps in refining the models, ensuring that they closely represent real-world scenarios and behaviors. By combining these advanced modeling techniques, the study aims to demonstrate the feasibility and benefits of implementing magnetocaloric cooling systems in electric and hybrid vehicles, potentially leading to more sustainable and efficient automotive thermal management solutions.

Keywords: Magnetocaloric; Cooling system; Matlab Simulink; COMSOL; Automotive.

History
Received: 31.07.2024
Accepted: 16.12.2024

Author Contacts
*Corresponding Author
e-mail addresses : mohand-ouyahia.bousseksou@capgemini.com

How to cite this paper: Bousseksou, M.O., Nouri, K., Bartoli, T., Bouzidi, W., Bessais, L., (2025). Magnetocaloric Cooling for Hybrid/ Hydrogen and Electric Vehicle Cabin and Powertrain Components. Engineering Perspective, 5 (1), 9-20. http://dx.doi.org/10.29228/eng.pers.77695

1. Introduction

The automotive industry is facing a technological revolution to achieve high global environmental goals. The use of new drive concepts such as pure electric or hybrid drives is a considerable success factor for more sustainable transportation. In a vehicle with these new concepts, the hybrid or 100% electric powertrain is of great technological importance [1].

The hybrid powertrain is made up of three components: the combustion engine, the electric motor powered by an energy storage system (such as a battery or fuel cell) and the power electronics that generate heat and require cooling. Several techniques have been implemented to recover heat sources and optimize energy harvesting. The development of innovative materials explored is to ensure and optimize the thermal management of all the organs of the hybrid powertrain of vehicles. The selection of magnetocaloric materials depends on the desired application. Taking gadolinium [2] as an example, to have a significant magnetocaloric effect (MCE), a temperature range of about 25 K before and after the curie transition (CT) is required. For the automotive sector, the range is 270 K to 340 K under a magnetic field of 0-1.5 T. Gd-based alloys may therefore be an ideal colling choice for various vehicle components.

Today, magnetic cooling has attracted considerable interest in scientific research, and many prototypes have been built by laboratories and companies such as Toshiba, Toyota, Astronautics, or even COOLTECH Applications [3] [4]. Magnetic cooling is

based on the MCE, which results in the heating of a material following its magnetization, also in its cooling during its demagnetization [5][6][7][8]. In the case of conventional refrigeration, a gas is used that undergoes cycles of compression / expansion. To put it another way, heating, or cooling. An equivalent principle is applied for magnetic cooling; it is a system in which a material with a magnetocaloric effect is subjected to a magnetization and demagnetization cycle. New multifunctional materials for magnetic cooling are produced that possess great magnetocaloric effects, such as compounds like gadolinium (Gd), manganese (Mn), oxides, intermetallic [9][10][11]perovskites, ceramics... etc. For applications below 270 K, other materials must be used. Pecharsky and Jr. Gschneidner [12] discovered a "giant" magnetocaloric effect in the alloy (Gd5(Si2Ge2)). Based on these studies, scientists and the refrigeration industry are beginning to seriously consider magnetic cooling at room temperature for industrial applications. There are also other materials with a giant magnetocaloric effect, such as MnAs1-xSbx [13], La(Fe1-xSix)13 [14]or MnFePxAs1-x [15].

This ecological process could ensure the cooling of the different components of the hybrid-electric powertrain. This new approach will reduce vehicle weight, fuel consumption, increase vehicle range, and improve environmental impact. This paper develops a new technology to efficiently cool the hybrid-electric powertrain.

The aim of this work is to develop a 1D model on MATLAB and a 2D model on COMSOL. These modelling were conducted to study the magnetocaloric effect and the cooling power to efficiently cool the hybrid-electric powertrain and the cabin.

2. Thermodynamic approach and simulation equations

In this section, the thermodynamic approach of the magnetocaloric effect has been developed, as well as the equations necessary for the theoretical modelling and numerical simulations of the magnetic cooling system. A thermodynamic system can be described in terms of variables states. There are two types: extensive, which depend on the size of the system studied, and intensive, which do not. The entropy of a magnetic material at constant pressure depends on the applied magnetic field H and the temperature T. It is defined as the sum of the contributions of the entropies, magnetic ($S_M(T,H)_P$), lattice ($S_R(T)_P$) and electronic ($S_E(T)_P$):

$$\boldsymbol{S(T,H) = S_M(T,H)_P + S_R(T)_P + S_E(T)_P} \quad (1)$$

The thermodynamic properties of a system, where T and P are fixed, and described by the Gibbs free energy G. The magnetic system is defined at constant pressure as a function of the temperature T, the pressure P, and the applied field H:

$$\boldsymbol{G(P,H,T) = U + PV - TS - \mu_0 MH} \quad (2)$$

Where μ_0 is the magnetic permeability of the vacuum, U is the internal energy of the system, P, H and T are intensive variables (pressure, magnetic field and temperature) and V, M and S are the extensive variables (volume, magnetization and entropy).

The total differential of G is given by:

$$\boldsymbol{dG(P,H,T) = dU + PdV + VdP - TdS - SdT - \mu_0 MdH - \mu_0 HdM} \quad (3)$$

On the other hand, we can write:

$$\boldsymbol{dG(P,H,T) = \left(\frac{\partial G}{\partial P}\right)_{T,H} dP + \left(\frac{\partial G}{\partial T}\right)_{P,H} dT + \left(\frac{\partial G}{\partial H}\right)_{P,T} dH} \quad (4)$$

By identifying the two equations (3) and (4), the variation of the internal energy is written:

$$\boldsymbol{dU = TdS + \mu_0 HdM + PdV} \quad (5)$$

Therefore, dG reduces to:

$$dG(P,H,T) = VdP - \mu_0 MdH - SdT \quad (6)$$

Using equations (4) and (6), we have:

$$\boldsymbol{V = \left(\frac{\partial G}{\partial P}\right)_{T,H}} \quad (7)$$

$$\boldsymbol{\mu_0 M = -\left(\frac{\partial G}{\partial H}\right)_{P,T}} \quad (8)$$

$$\boldsymbol{S = -\left(\frac{\partial G}{\partial T}\right)_{P,H}} \quad (9)$$

By deriving equations (7) and (8), we obtain Maxwell's relation [16]:

$$\mu_0\left(\frac{\partial M}{\partial T}\right) = -\left(\frac{\partial}{\partial T}\right)\left(\frac{\partial G}{\partial H}\right) = -\left(\frac{\partial}{\partial H}\right)\left(\frac{\partial G}{\partial T}\right) = \left(\frac{\partial S}{\partial H}\right) \quad (10)$$

Therefore,

$$\mu_0\left(\frac{\partial G}{\partial T}\right)_{P,H} = \left(\frac{\partial S}{\partial H}\right)_{P,T} \quad (11)$$

3. Thermodynamic approach and simulation equations

To determine the variation of the maximum magnetic entropy, we integrate the previously established relationship between two magnetic field values, assuming an isothermal transformation:

$$\int_{H1}^{H2} \mu_0\left(\frac{\partial M}{\partial T}\right)_{P,H} dH = \int_{H1}^{H2} \left(\frac{\partial S}{\partial H}\right)_{P,T} dH = \Delta S(T,\Delta H) \quad (12)$$

This entropy variation is noted as magnetic entropy variation since we assumed from the beginning that the application of a magnetic field affects only the magnetic order, and we can therefore write:

$$\int_{H1}^{H2} \mu_0\left(\frac{\partial M}{\partial T}\right)_{P,H} dH = \Delta S_M(T,\Delta H) \quad (13)$$

Equation (12) shows that the change in magnetic entropy Δ (T,

ΔH) is proportional to the derivative of the magnetization with respect to temperature at constant field and the change in the magnetic field. If the field varies between 0 and H, then equation (12) is written:

$$\Delta S_M(T, \Delta H) = \int_0^H \mu_0 \left(\frac{\partial M}{\partial T}\right)_{P,H} dH \quad (14)$$

The variation in magnetic entropy can be determined by integrating the magnetization isotherms. It is important to highlight that based on the measurements of the material's magnetization as a function of temperature M (T) and magnetic field M (H), it is possible to obtain the value of ΔS, at different fields and temperatures, after numerical integration according to the following formula [17]:

$$\Delta S_M(T_i, \Delta H) = \mu_0 \sum_i \frac{M_{i+1} - M_i}{T_{i+1} - T_i} \Delta H_i \quad (15)$$

With:

μ_0: magnetic permeability of the vacuum.

M_i, M_{i+1} : magnetization measured at T_i, T_{i+1} to the variation of the applied field ΔH_i.

We recall that ΔS and RCP are the two main quantities of the magnetocaloric effect (MCE). The value of enables us to characterize magnetocaloric materials by the relative cooling power (RCP). It corresponds to the amount of heat that can be transferred from the hot source to the cold source of a cooling system. It can be described for a given magnetic field by the following relation:

$$RCP = -\Delta S_M^{max} \times \delta T_{FWHM} \quad (16)$$

Or ΔS_M^{max} is the maximum value of the magnetic entropy change and δT_{FWHM} the maximum half-height width of the corresponding ΔS_M.

4. Result and discussions

A 1D model on Matlab-Simulink is used to model the magnetocaloric effect, the cooling of the powertrain components and the driver cabin, and a 2D model on COMSOL is established to determine the characteristics of the permanent magnet.

4.1 Matlab Simulink model

The Simulink model of the cooling system provide the use of a thermodynamic cycle based on the magnetocaloric effect for the cooling of the powertrain and cabin (or even the heating of the cabin if we use the reversibility of the system).

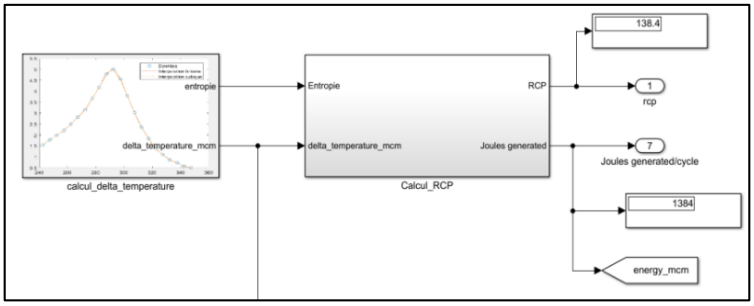

Figure 1. Simulink Block of the MCM and Permanent magnet

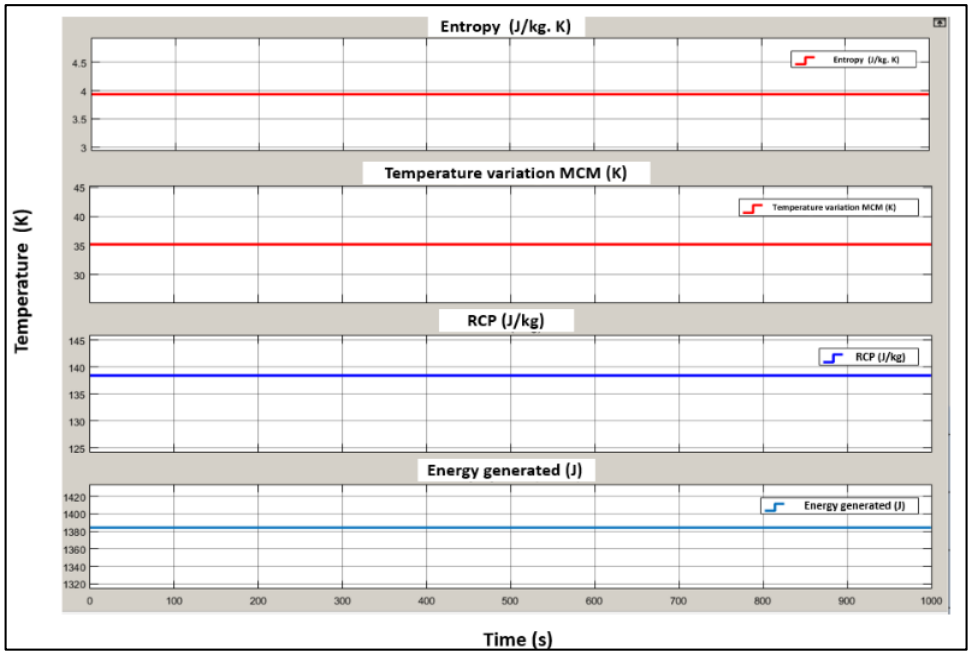

Figure 2. The simulation result vs time of the following parameters: Entropy, temperature variation, Relative cooling power and the energy produced

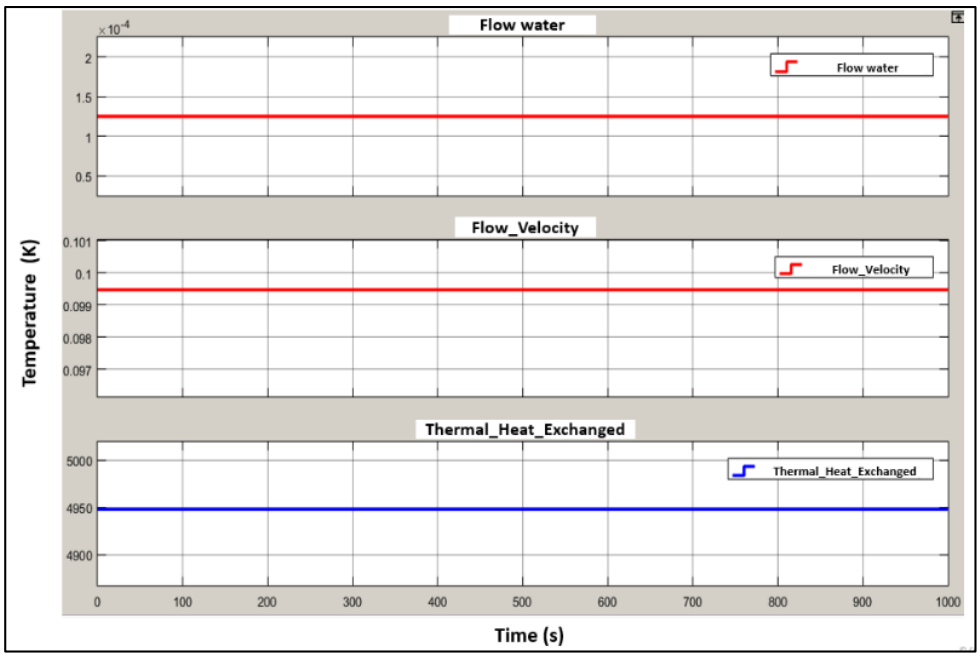

Figure 3. The simulation result vs time of the following parameters: mass flow rate of water, flow velocity and the thermal heat ex-changed

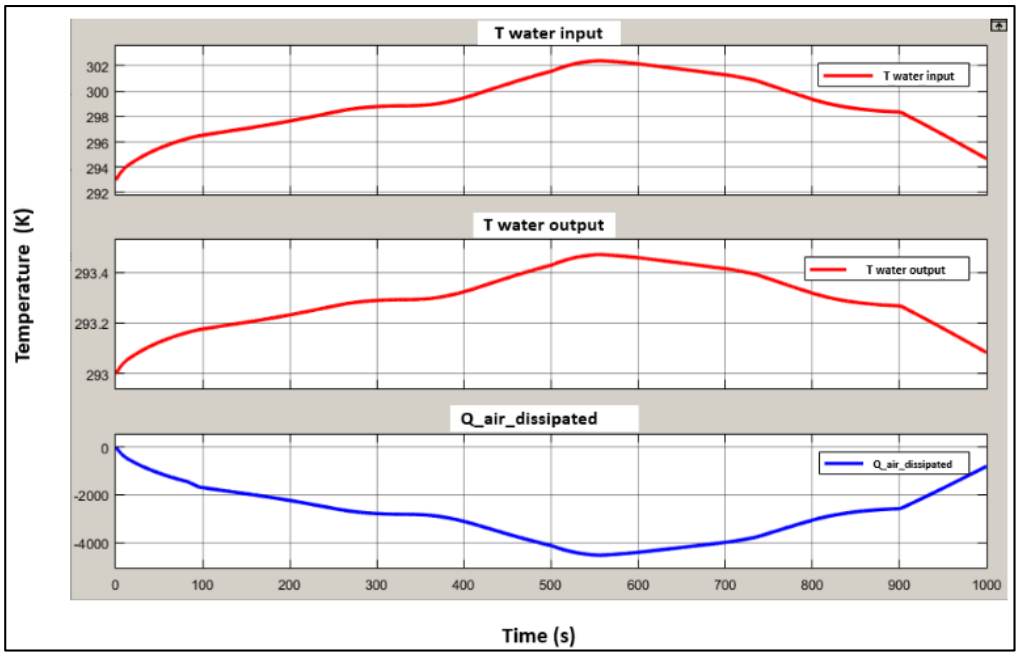

Figure 4. The simulation result vs time of the following parameters: water at radiator inlet, water at radiator outlet and dissipated energy of the air

Part 1: Magnetocaloric material (MCM) & Permanent Magnet block

Using the Matlab script, two magnetic entropy variation maps (0–1 T & 0–2 T) which are averaged to calculate the magnetic entropy ΔS and the temperature variation ΔT at a magnetic field applied of 1.5 T (Figure 1). The Gd is taken as a reference for the magnetocaloric around room temperature. The value of the maximum magnetic entropy of Gd is equal to 3.8 J/kg. K [18]. The relative cooling power (RCP) is calculated as follows:

$$\mathrm{RCP} = \Delta S_{\max} \times \Delta T = 138.5 \ \mathrm{J/kg} \quad (17)$$

The energy generated depends on the mass of magnetocaloric material (MCM) (10 kg for this use case). The energy generated (Figure 2):

$$Q = \mathrm{RCP} \times \mathrm{mass\ of\ MCM} = 1385 \ \mathrm{J} \quad (18)$$

The external convection was used for the calculation of heat transfer, this approximation is used for uniform plates with a laminar regime for the heat transfer fluid (Water). For the convection study, we are used the same thermodynamic simulation cited in this [2].

The energy Q1 transported in the heat transfer fluid (water) is calculated based on the water flow rate and the flow velocity. For a flow rate of 0.000125 m^3/s = 7.5 l/min, this fluid flow generates energy Q1 = 4950 J (Figure 3). This Q1 energy is greater than Q (Q1 > Q), the flow rate of 7.5 l/min is therefore sufficient to absorb the energy generated by the MCM.

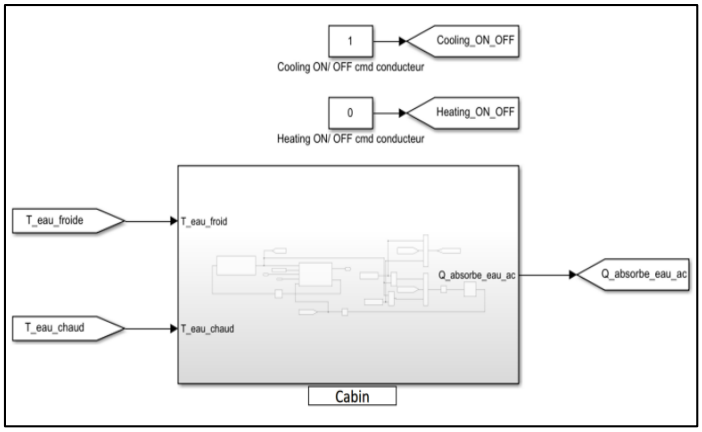

Figure 5. The Simulink block of the driver's cabin

Part 2: Radiator block of Powertrain components (PWT)

The radiator is essential to ensure that the hot or cold water leaving the PWT is reduced to room temperature before entering the tank. As in the radiator, we have the interaction of water with air, so the modeling is based on a thermal exchange between them.

For PWT cooling, cold water is circulated around the components before it is transferred to the radiator. The inlet temperature of the water is higher than the ambient temperature because the water absorbs heat from the PWT components. In the radiator, the water is reduced back to ambient (T water output) before returning to the tank (Figure 4).

Part 3: Cooler Block

The cold radiator is used to control the temperature of the passenger compartment. In the cold radiator there is an interaction between the cold/hot water and the air in the driver's cabin, for cooling or heating the driver's cabin. The modelling of the cold radiator was done in the same principle as the PWT radiator. A temperature controller was modelled to simulate the driver's choice of cabin temperature.

a. Driver's cabin: Model of an air tank with fixed volume/mass to simulate the driver's cab.

b. Cabin radiator: The model of the radiator is based on the same principle as the hot radiator explained above.

c. Controller: It is a controller which makes the request of water mass according to the difference of temperature between the cabin and the wished set point ('error' of temperature). This control is created with the help of a well-calibrated 1-D carto, to output the cold/hot water mass according to the temperature difference (or error) to cool/heat the air.

For the thermal management of the cabin simulation, the radiator is used to control the temperature of the passenger compartment.

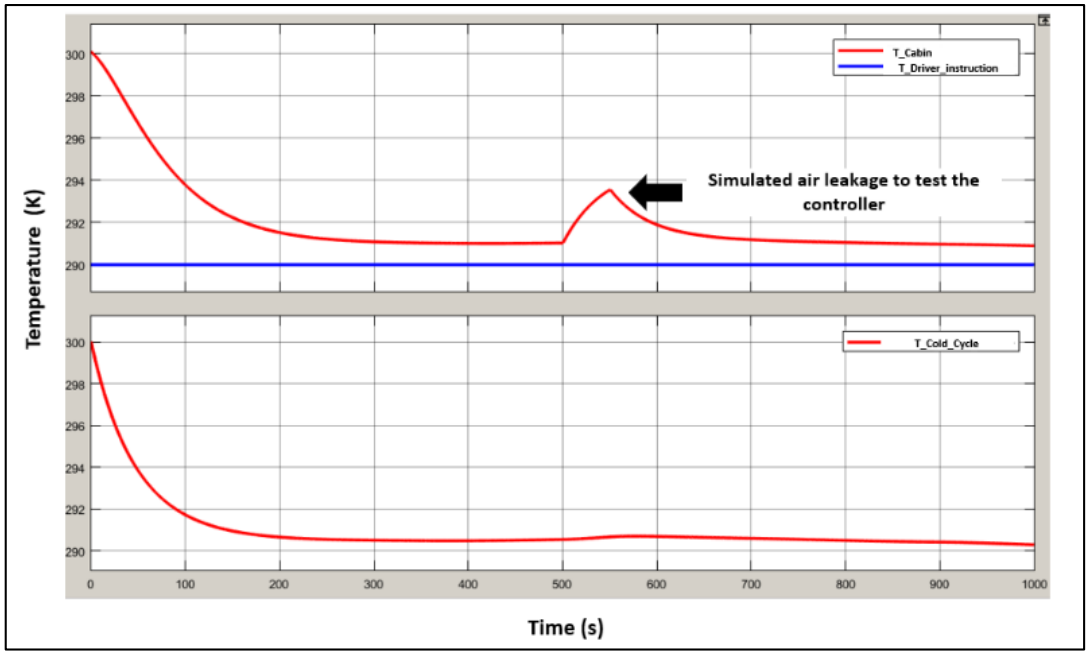

Figure 6. The simulation results of the cabin temperature and the air leakage

This model (Figure 5) takes account of an air tank with fixed volume and mass to simulate the driver's cab. This model radiator is based on the same principle of the Hot Radiator explained previously (see PWT radiator). The temperature set point given by the driver for heating/cooling is controlled within a defined temperature range. A controller for requesting the water mass based on the temperature difference between the cabin and the desired set point has been added to the model. This allows the temperature of the cabin to be regulated. The air temperature is calculated based on the weighted average:

- Total air mass = m_air.
- Air mass interacting with radiator = m_air_cycle.
- Air leakage mass = m_air_leakage.

Each air part is weighted with its temperature and the three parts were added to divide by total air mass to get the cabin temperature. The cabin temperature is reduced to close to the driver's desired setting. The small temperature difference is due to the efficiency of the radiator. It should also be noted that the possible cooling limit is related to the temperature of the cold water (Figure 6).

Part 4: PWT heat exchanger block

In this part, we performed the modelling for the heat exchange between hot water and PWT when the system needs to be heated. The hot water exchanger control of the PWT were analysed. The heat exchanger is activated or deactivated based on the need for heating or not for the PWT components. The control is based on continuing to heat the PWT components until all components reach room temperature (293 K). Then, when the heat exchanger is active, and one component needs more heating or reaches the temperature of 293 K before the other. In this case, the heating of all components is controlled separately. We calculate the heat absorbed by each PWT component battery, internal combustion engine and electric motor. And at the end, we calculate the decrease of the hot water temperature.

In addition, the modelling of energy absorbed by battery/ thermal or electric motor have been conducted. The heat exchange of all PWT components is modelled in the same direction as the temperature input corresponding to that component, T_battery / T_motor /T_elec. The heat exchange between the PWT components and the water is by convection:

$$Q = h \times A \times \Delta T \quad (19)$$

With:
A: the surface.
h: heat transfer coefficient.
ΔT: temperature variation.

Part 5: PWT cold exchanger block

This part is dedicated to the heat exchange model between cold water and PWT when the system needs to be cooled. When the system temperature is equal or higher than the ambient temperature and the PWT components start to work, there is a need to cool them to avoid a temperature increase that would exceed the limit. The objective is to ensure optimal operation of PWT components. As explained in the case of the hot exchanger, the operating principle for the cold exchanger is the same, but instead of heating, this exchanger is active when the PWT components need to be cooled. Therefore, the use of the hot or cold exchanger depends directly on the need of the PWT.

The activation of the cold exchanger is done when the temperature of all the PWT components are higher than 293 K. Therefore, if we start the simulation with an initial temperature of 293 K, the cold exchanger will be activated from the beginning. To control the cooling for each component based on its need, we have the same principle as for the heat exchanger. The water distribution is based on which component needs more energy to cool it.

Modelling of a cold exchanger of the PWT components was simulated. The modelling of the cold exchanger follows the same logic as for the hot exchanger. We calculate the heat dissipated by each component of the PWT (battery, internal combustion engine and electric motor). In general, the hybrid powertrain includes three components: the combustion engine, an electric motor powered by energy storage (such as a battery or fuel cell), and power electronics that produce heat and need to be cooled.

Part 6: PWT components model

The complete modelling of the battery, the electric motor and the combustion engine has been done by us (Figure 7). This part shows the outputs of these components necessary for the thermal management by the magnetocaloric system. The temperatures and the heat dissipated of these powertrain components during operation have been studied to perform a real time simulation. To test this magnetic cooling system model and the heat exchange between the water and the PWT car's drive train (to simulate heating or cooling), the PWT component model was added. The heat generated by the PWT components will be considered by the cooling system, which will adapt to either heat or cool, as needed. To calculate the temperature of each component, we use the heat generated by the component and add/decrease the heat added/dissipated by the hot/cold exchanger. Overall model is seen on Figure 8.

Total energy requirement (Q_{tot}) = Energy requirement for combustion engine (Q1) + Energy requirement for electric motor (Q2) + Energy requirement for battery (Q3)

Total water mass = m_water

Hot water mass for the heat engine = Q1 / Q_{tot} × m_water

Hot water mass for the electric motor = Q1 / Q_{tot} × m_water

Hot water mass for engine and battery = Q1 / Q_{tot} × m_water

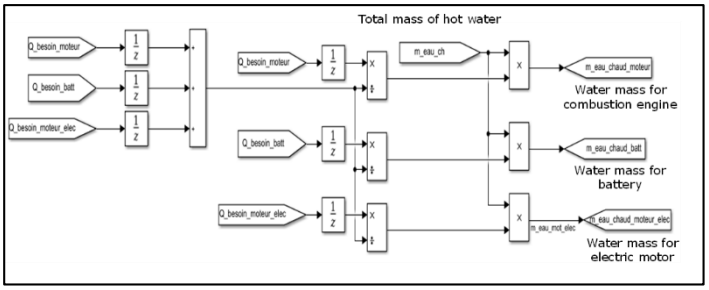

Figure 7. The simulation block of PWT components model

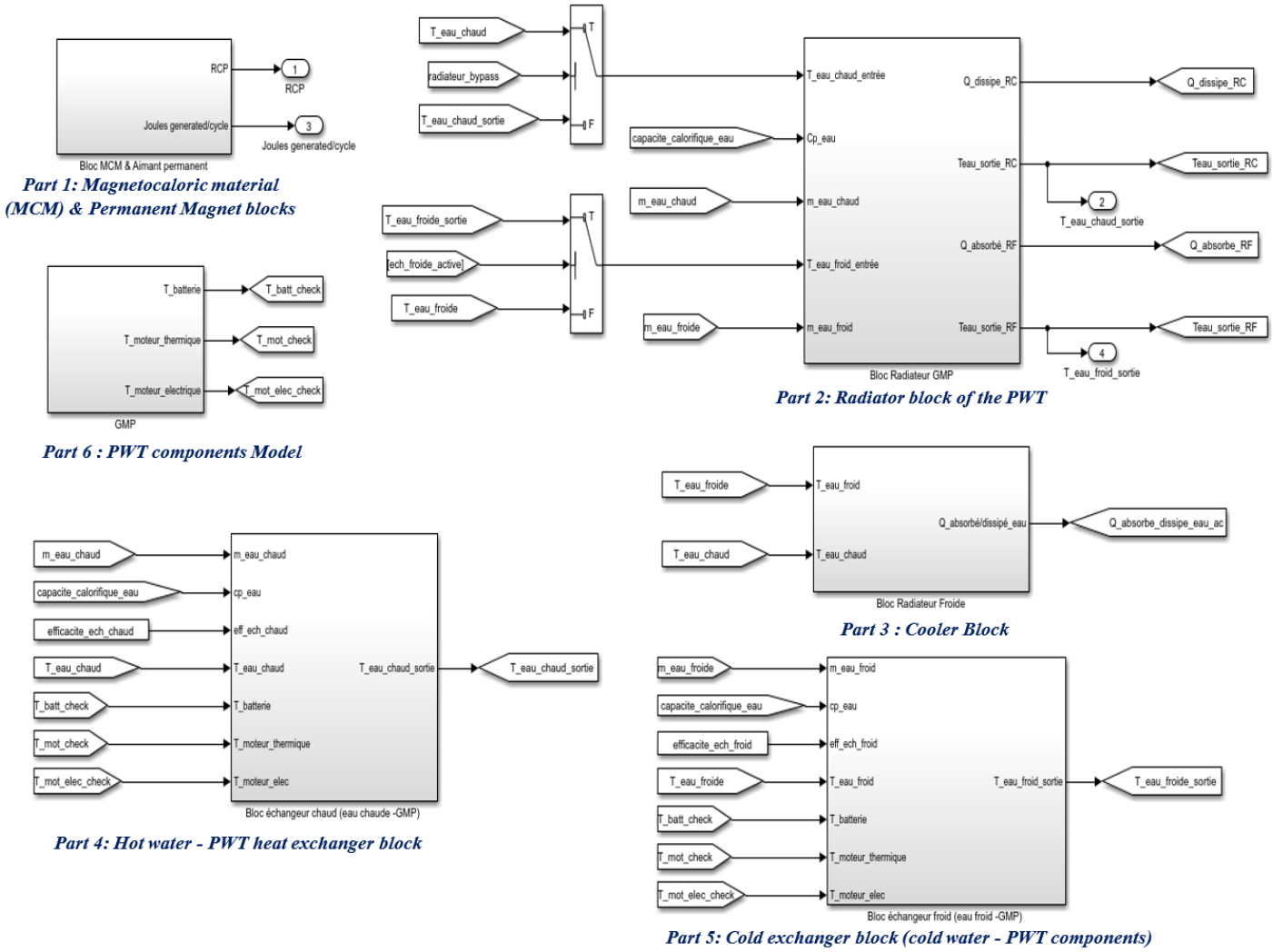

Figure 8. Interface of the global model of the magnetic cooling system and the powertrain components in Matlab-Simulink.

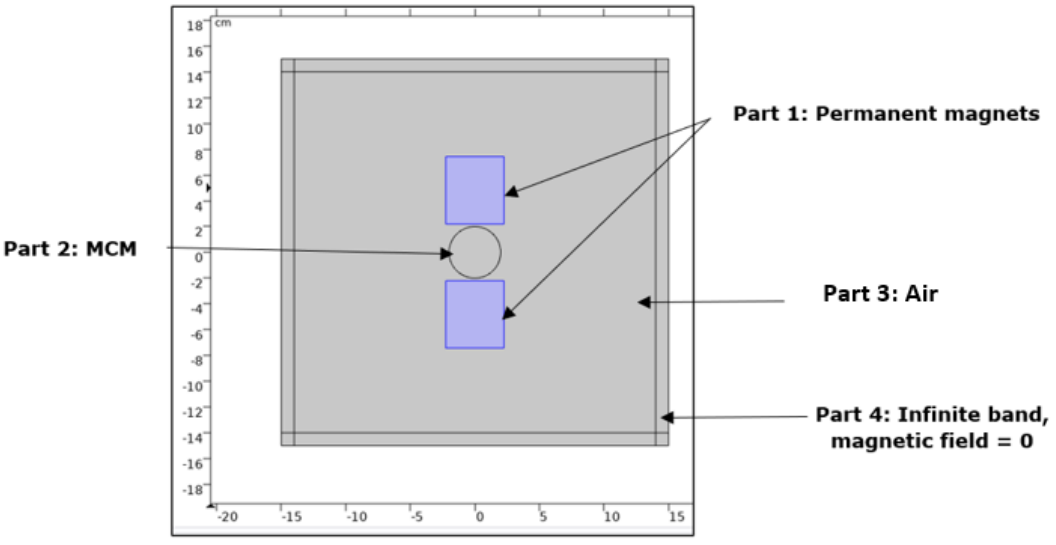

Figure 9. 2 Dimension COMSOL model of the MCM and permanent magnet.

4.2 COMSOL model

The COMSOL model enables to size and characterise the permanent magnet according to the magnetic field undergoes by the MCM block, as the distribution of the magnetic field lines changes according to the shape of the magnets.

The COMSOL model focuses on the study of the magnetic field generated by two parallel plate magnets in the magnetocaloric system.

There are four main parts to have the magnetic field simulated (Figure 9). For the part 1: Two magnetic blocks, whose properties have been defined to obtain the necessary magnetic field intensity. The part 2: the magnetocaloric material (MCM) block (circle of desired size), with the relative permeability defined to behave like Gadolinium (Gd). In the part 3: air of standard relative permeability

1 around the magnet and MCM. And finally, part 4: Infinite band around the borders to ensure zero magnetic field away from the magnets, to make the calculations converge.

The main parameters in the COMSOL model are defined. The relative air permeability was defined as 1. The square boundary was defined with a magnetic node point, i.e., the magnetic field at the edges is 0 T. The relative permeability of the MCM was defined as 100, based on several reviewed papers [19] and the magnetic property for permanent magnet blocks was assigned based on the method chosen for modelling. We tested three methodologies as mentioned below:

Method 1
Flux standard of remanent density = 1.4 T

Method 2
Magnetic flux density standard = 1.5 T (max 1.6 T)
Coercive field = 1500 kA/m
Magnetic energy density = 413 kJ/m

Method 3
Magnetization (Ms) = 1.6 T = 1276320 Amps/m

The third method based on the value of the magnetization, was chosen to make the simulation on COMSOL.

All other parameters have been fixed and the dimension only changes for permanent magnets. The distance between the MCM and the magnet has been fixed at 2 mm. The radius of the MCM has been fixed to 20 mm. The size of the permanent magnets varies based on two test cases, as explained below. So, to analyse all geometrical configurations, we studied two global use case based on the length of the permanent magnet (Table 1).

It should be noted that the mass and volume of the magnet have been set according to the operating characteristics of the magnetic cooling system. In each use case, we calculate the width and thickness according to the fixed length. The volume of a magnet plate is 188.3 cm^3 and the length of the plate are 9 cm and 8 cm: Table 2 summarises the characteristics of the permanent magnet and the magnetocaloric material.

$$\text{Width} \times \text{Thickness} = \text{Volume/Length} = 20.9\ cm^2 \quad (20)$$

Table 1. The use cases used for COMSOL simulation for the permanent magnet.

Use case 1 – Length = 9 cm	Use case 2 – Length = 8 cm
n combination of Width (cm) × Thickness (cm)	n combination of Width (cm) × Thickness (cm)
1st combination of 8 × 2.61	1st combination of 8×2.94
2nd combination of 7 × 2.98	2nd combination of 7×3.36
3rd combination of 6 × 3.48	3rd combination of 6×3.92
4th combination of 5.5 × 3.80	4th combination of 5.5×4.30
5th combination of 5 × 4.18	5th combination of 5×4.70
6th combination of 4.5 × 4.64	6th combination of 4.5×5.23

Table 2. Characteristics of the permanent magnet and the MCM.

Mass of the permanent magnet	2.9 kg
Mass density of Gadolinium	7700×10^{-6} kg/cm^3
Total volume of the permanent magnet	376.6 cm^3
Volume of a magnet plate	188.3 cm^3

In the two use cases, (9 cm and 8 cm long), we observe that the magnetic field strength increases by decreasing the width of the permanent magnet and increasing its thickness. (Figures 10 and 11).

After an analysis of the COMSOL study of permanent magnet and magnetocaloric material, the better combination is described in the Table 3 (use case 2). The value of the magnetic field intensity produced by the permanent magnet in this COMSOL simulation is about 1.48 T.

Table 3. Characteristics of the permanent magnet and the MCM.

Use case	Total mass (kg)	Length (cm)	Width (cm)	Thickness (cm)	Magnetic field max (Tesla)
Use Case 1	2.9	9	4.5	4.64	1.47
Use case 2	2.9	8	4.5	5.23	1.48

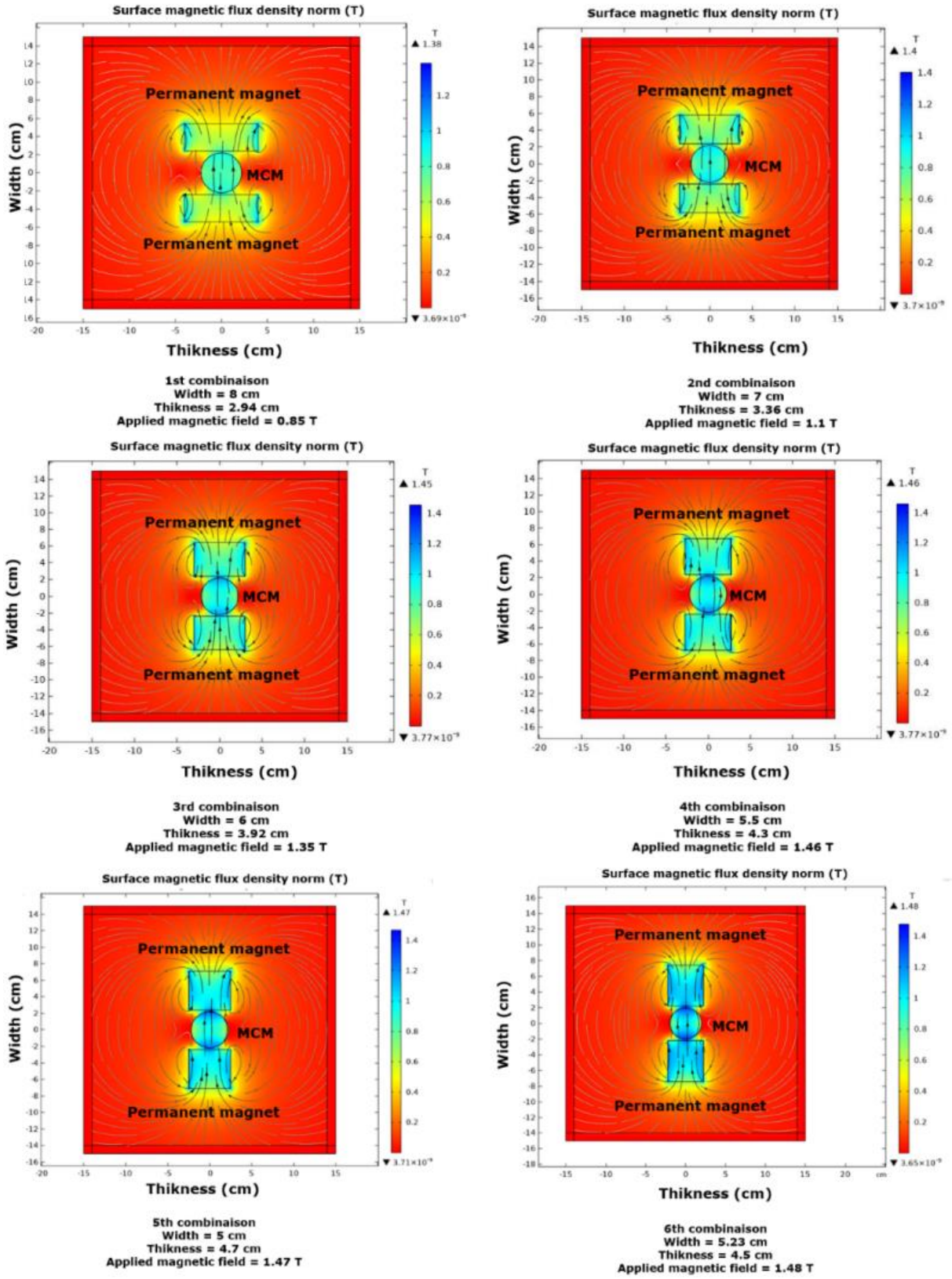

Figure 10. Evolution of the magnetic field intensity versus the width and thickness of the magnet (use case 1 - length 9 cm)

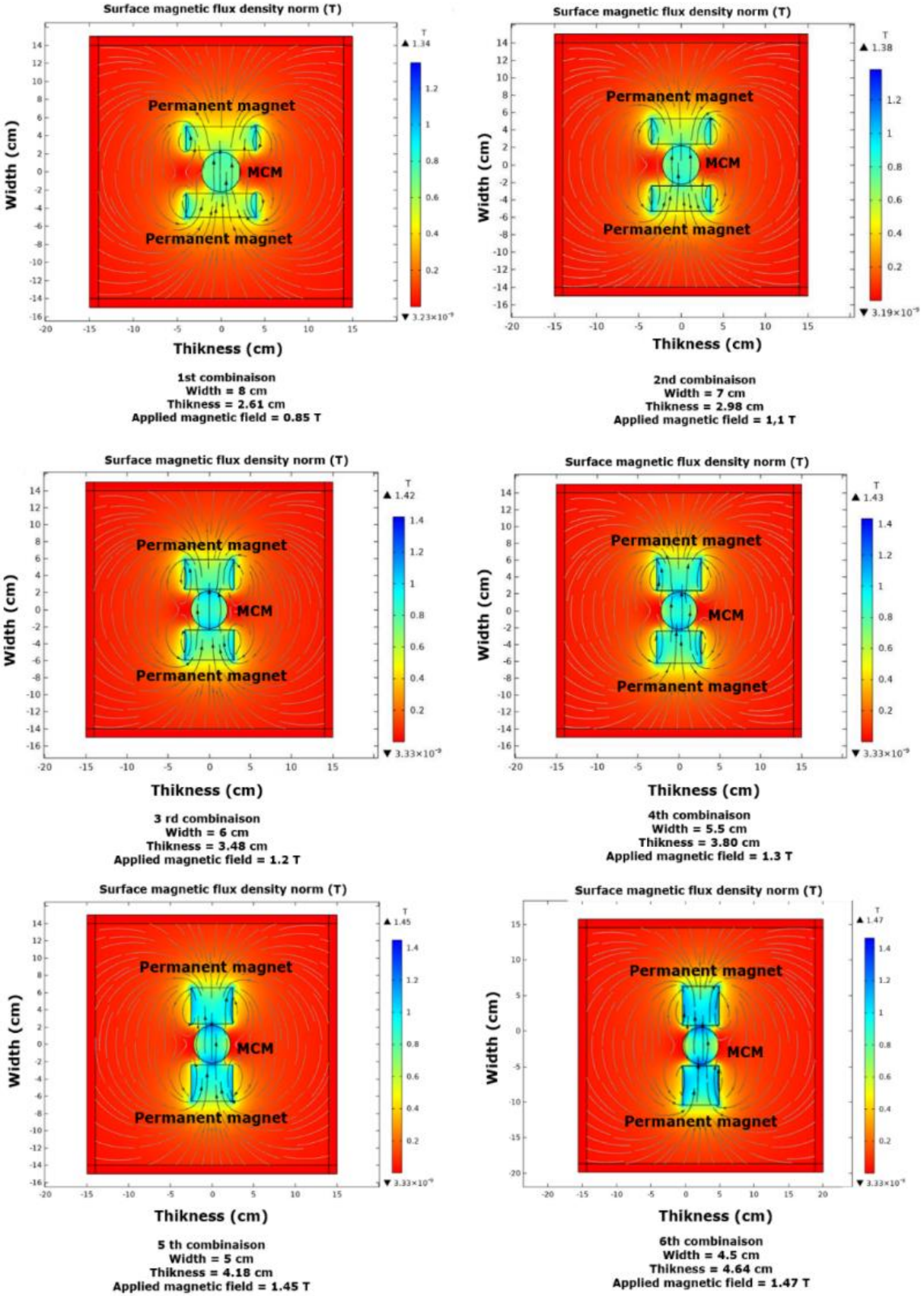

Figure 11. Evolution of the magnetic field intensity versus the width and thickness of the magnet (use case 2 - length 8 cm)

5. Conclusions

The objective of this paper was to study and understand the behavior of a magnetic cooling system at room temperature and to investigate and demonstrate the efficiency of this new technology.

To achieve this objective, a Matlab Simulink model was built of the permanent magnet, magnetocaloric material, the hybrid powertrain components as well as the water tanks, heat exchanger and radiators. In addition, to ensure the thermal management of the driver's cabin, a Simulink block has been added. This study was coupled with a two-dimensional model on the COMSOL software. This model allows to evaluate the behavior of the magnetocaloric material and the magnetic field intensity to improve the design and the energy consumption. The model developed in this study enables simulate a magnetic cooling system. The heat source which represents the magnetocaloric equation and approach is modelled based on the data obtained from experimental measurements.

Acknowledgment

This work was supported by Capgemini engineering-France (Innovative and Intelligent Powertrain Research & Innovation Department). The authors would like to thank the other members of the team, Fatima Haidar, Chayma Mohsni, Racha Bayzou and Thierry Bertau. The authors would also like to thank the interns of the iPowertrain project.

Nomenclature

MCE	magnetocaloric effect
CT	curie transition
H	magnetic field (T)
T	temperature (K)
P	pressure
G	Gibbs free energy
U	internal energy of the system
V	Volume (m^3)
M	magnetization
S	entropy
μ_0	magnetic permeability of the vacuum
RCP	relative cooling power (J/kg)
Q	energy (J)
PWT	powertrain
m_air	total air mass (kg)
m_air_cycle	air mass interacting with radiator (kg)
m_air_leakage	air leakage mass (kg)
A	Surface (m^2)
h	heat transfer coefficient (W/(m.K))
m_water	total water mass (kg)
MCM	magnetocaloric material
T_ini	initial temperature of PWT/ tank (K)

Conflict of Interest Statement

All authors have given approval to the final version of the manuscript. The authors declare that there is no conflict of interest in the study.

CRediT Author Statement

Mohand-Ouyahia Bousseksou: Writing- review & editing, supervision, project leader, methodology & software, **Kamal Nouri:** Writing original draft & editing, **Thomas Bartoli:** Formal analysis, **Wassim Bouzidi:** Formal analysis **Lotfi Bessais:** Review & editing.

References

1. Torregrosa-Jaime, B., Corberán, J. M., Vasile, C., Muller, C., & Risser, M. (2014). Sizing of a reversible magnetic heat pump for the automotive industry. International Journal of Refrigeration, 37, 156-164. https://doi.org/10.1016/j.ijrefrig.2013.06.018
2. Achkar, G. E., B. Liu, & R. Bennacer. (2019). Numerical study on the thermohydraulic performance of a reciprocating room temperature active magnetic regenerator. E3S Web Conf, 128, 07001. https://doi.org/10.1051/e3sconf/201912807001
3. Broughton, J., Vanessa Smet, Rao R. Tummala, & Yogendra K. Joshi. (2018). Review of Thermal Packaging Technologies for Automotive Power Electronics for Traction Purpose. Journal of Electron Packaging, 140, 040801. https://doi.org/10.1115/1.4040828
4. C Vasile, & C Müller. (2006). Innovative design of a magnetocaloric system. International Journal of Refrigeration, 29, 1318-1326. https://doi.org/10.1016/j.ijrefrig.2006.07.016
5. T. Lehy et G. Willems. (1976). Population Kinetics of Antral Gastrin Cells in the Mouse. Gastroenterology, 71, 614-619. https://doi.org/10.1016/S0016-5085(76)80552-5
6. Lionte, S., Carmen Vasile, & Monica Siroux . (2014). La réfrigération magnétique : technologie innovante. COFRET'14- PF3-041, 14. https://doi:10.13140/2.1.3946.5767
7. Lee, S. J., J. M. Kenkel, V. K. Pecharsky, & D. C. Jiles . (2002). Permanent magnet array for the magnetic refrigerator. Journal of Applied Physics, 91, 8894. http://doi.org/10.1063/1.1451906
8. Okamura, T., Kazuhiko Yamada, Naoki Hirano, Naoki Hirano, & Shigeo Naga. (2006). Performance of a room-temperature rotary magnetic refrigerator. International Journal of Refrigeration, 29, 1327-1331. http://10.1016/j.ijrefrig.2006.07.020.
9. Nouri, K., M. Saidi, L. Bessais, & M. Jemmali. (2021). Structural, magnetic and magnetocaloric study of Sm 2 Fe 17−x Ni x (x = 0, 0.25, 0.35 and 0.5) compounds. Applied Physics, 127, 442. https://doi.org/10.1007/s00339-021-04546-1
10. Nouri, K., T. Bartoli, A. Chrobak, J. Moscovici , & L. Bessais . (2018). Magnetism and Hyperfine Parameters in Iron Rich Gd2Fe17-xSix Intermetallics. Journal of Electronic Materials, 47, 3836–3846. https://doi.org/10.1007/s11664-018-6256-z
11. Bouzidi, W., Bartoli, T., Sedek, R., Bouzidi, A., Moscovici, J., & Bessais, L. (2021). Low-field magnetocaloric effect of NdFe _ 11 Ti NdFe 11 Ti and SmFe _ 10 V _ 2 SmFe 10 V 2 compounds. Journal of Materials Science: Materials in Electronics, 32, 10579-10586. https://doi.org/10.1007/s10854-021-05713-z
12. Pecharsky, V. K., & K. A. Gschneidner, Jr. (1997). Giant Magnetocaloric Effect in Gd5(Si2Ge2). Physical Review Letters, 78, 4494-4497. https://doi.org/10.1103/PhysRevLett.78.4494
13. WadaY, H., & Y. Tanabe. (2001). Giant magnetocaloric effect of MnAs1−xSbx. 79, 3302-3304. https://doi.org/10.1063/1.1419048
14. Hu, F.-x., Bao-gen Shen, Ji-rong Sun, Zhao-hua Cheng, Guang-hui Rao, & Xi-xiang Zhang. (2001). Influence of negative lattice expansion and

metamagnetic transition on magnetic entropy change in the compound LaFe11.4Si1.6. Applied Physics Letters, 78, 3675-3677. https://doi.org/10.1063/1.1375836

15. Tegus, O., E. Brück, K H J. Buschow, & F R de Boer. (2002). Transition-metal-based magnetic refrigerants for room-temperature applications. 415, 150–152. https://doi.org/10.1038/415150a
16. Zou, J. D., H. Wada, B. G. Shen, J. R. Sun, & W. Li. (2008). Giant magnetocaloric effect and soft-mode magneto-structural phase transition in MnAs. Europhysics Letters, 81, 47002. https://doi:10.1209/0295-5075/81/47002
17. Duchoň, F., Andrej Babinec , Martin Kajan, Peter Beňo , Martin Florek, Tomáš Fico, & Ladislav Jurišica. (2014). Path Planning with Modified a Star Algorithm for a Mobile Robot. Procedia Engineering, 96, 59-69. https://doi.org/10.1016/j.proeng.2014.12.098
18. Jaballah, H., Kamel Nouri, Najeh Mliki, Lotfi Bessais, & Mosbah Jemmali. (2022). Investigation of Magnetic Entropy Change in Intermetallic Compounds SmNi3–xFex Based on Maxwell Relation and Phenomenological Model. Crystals, 12, 481. https://doi.org/10.3390/cryst12040481
19. Fraga, G. L., Paulo Pureur, & Lisandro Pavie Cardoso. (2010). Impedance and initial magnetic permeability of gadolinium. Journal of Applied Physics, 107, 053909. https://doi.org/10.1063/1.3288696

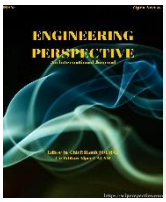

e-ISSN:2757-9077

ENGINEERING PERSPECTIVE

https://sciperspective.com/ Research Paper

Design and Optimisation of a Double Wishbone Independent Suspension System for an L6 Electric Vehicle: A Response Surface Methodology Based Design Application

Mohammad Nassar [1], Kübra Polat[1*], Yağmur Koçlu[1], Mehmet Murat Topaç[1]

[1] *Mechanical Engineering Department, Faculty of Engineering, Dokuz Eylül University, İzmir, 35397, Turkey*

ABSTRACT

Suspensions are vital vehicle subsystems that provide ride comfort, stability and handling while absorbing shocks caused by road irregularities. Their designs require careful consideration of structural integrity, weight reduction and performance optimisation. In light electric vehicles, such as those in the L6 class, the design and optimisation of suspension systems becomes even more critical due to design compactness and functionality. The aim of this study is to design a front independent suspension system for an electric L6 class vehicle and to outline an optimisation-based design process of this design by Finite Element Analysis (FEA). In the first stage of the study, various load cases and the effects of these loads on the connection points were determined and force analyses were performed. Then, a preliminary design was built to withstand the types of loading to which it will be subjected. Afterwards, FEA was performed on the preliminary design using the data obtained from the force analysis. As a result of this analysis, critical load case and critical regions were identified. In the optimisation stage, the outer diameter (D), wall thickness (t) and radius of curvature (R) were defined as input parameters, while mass, equivalent stress and total deformation were selected as output parameters. As a result of the optimisation-based design, a stress reduction of approximately 43% was observed at the critical region. In addition, the percentage of the influence was investigated in order to better understand the effects of the basic design parameters. Among the parameters, the wall thickness was found to be the design parameter which has the highest effect on stress distribution and part mass.

Keywords: Electric vehicles; Electromobility; Design optimisation; Independent suspension; Vehicle component design

History
Received: 28.10.2024
Accepted: 15.01.2025

Author Contacts
**Corresponding Author*
e-mail addresses : k.polat@ogr.deu.edu.tr

How to cite this paper: Nassar, M., Polat, K., Koçlu, Y., Topaç, M.M., (2025). Design and Optimisation of a Double Wishbone Independent Suspension System for an L6 electric Vehicle: A Response Surface Methodology Based Design Application. Engineering Perspective, 5 (1), 21-30. http://dx.doi.org/10.29228/eng.pers.79569

1. Introduction

The global population is increasing by 240,000 people per day and 90 million people per year, leading to an increasing demand for vehicles [1]. As technology continues to improve, mobility demand is projected to grow three times faster than population growth [2]. This increase in the number of vehicles contributes significantly to air pollution, which increases exhaust emissions and poses serious risks to public health. In many countries, the automotive sector is responsible for 48% of the total carbon dioxide (CO_2) emissions [3]. Furthermore, modern cities are facing a traffic crisis, leading to more noise and traffic congestion. The energy crisis, which is worsening due to decreasing fossil fuel resources, is becoming more serious over time [4]. The European Commission's Roadmap to a Single European Transport Area Towards aims to reduce traffic and pollution problems as one of its objectives towards a competitive and clean transport system [5]. In order to achieve this goal, vehicle manufacturers have had to realise a series of improvements in order to adapt to competitive conditions. There is also a need to provide safer and more economical options to effectively address environmental and population issues. As a result, the use of light electric vehicles is growing rapidly. Many cities have started to use light vehicles for urban transport. This plays an important role in solving various problems, especially in the freight transport sector [6].

The lower centre of gravity of electric vehicles makes their suspension design extremely important for traction and stability. Small electric vehicles, especially those classified in the L6 category, are increasingly incorporating independent suspension systems in their design to improve ride quality and handling. There are also different types of suspension systems for such vehicles in the literature [6]. Independent suspension is a widely used system in automotive engineering, characterised by the ability of each wheel to move vertically independently of the other; this design feature is essential in improving the overall stability and dynamic behaviour of the vehicle, contributing to handling and ride comfort.

The double wishbone suspension system is essentially considered to be a four-bar mechanism; one side is connected to the chassis, considered to be the ground, and the other side is connected to the wheel via a steering knuckle [7]. The double wishbone suspension system has several advantages over other suspension systems.

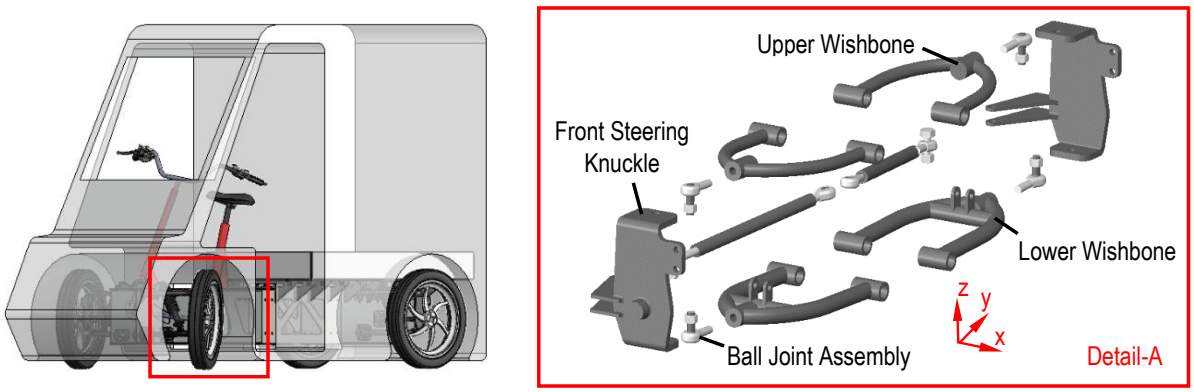

a b

Figure 1. Suspension system components and their integration in the vehicle

Due to its many design parameters, it is more flexible and versatile, allowing the kinematics of the vehicle to be controlled and adapted to specific applications. It can also reduce the weight of the unsprung mass, improving the vehicle's dynamic characteristics, although it is more complex to design than other suspension systems [8]. There are several methods in the literature for designing and analysing double wishbone suspension systems for light electric vehicles. The double wishbone suspension system consists of an upper wishbone, lower wishbone, shock absorber, steering system and steering knuckle as shown in Figure 1.

The shock absorber is mounted on the upper or lower arm and is responsible for absorbing road inputs to provide ride comfort. The wishbone holding the shock absorber carries/bears more load, so it is called the carrier wishbone, while the other wishbone is called the control wishbone [9]. Double wishbone suspension system is also called short-long suspension system, with the upper arm being the shorter arm and the lower arm the longer arm [7]. In general, when designing wishbones, it is important to provide a difference in length between the control and carrier arms as they affect the wheel angle change, camber change and to some extent the track width change during the vertical movement of the wheel. Reducing the length of the control arm will result in a positive camber in rebound and a negative angle when compressed, which is desirable when designing a suspension system [10].

Response Surface Methodology (RSM) is widely used in various industries, one of the most important of which is the automotive industry [11-13]. RSM is a method used to determine the effect of independent variables in a system on dependent parameters. This approach allows for efficient design modifications and ensures that structural rigidity is maintained. In a study using ANSYS® Workbench, a mass reduction analysis of a motor mounting bracket was performed using RSM method and a mass reduction of 4.31% was achieved by keeping the failure load constant [14]. In another study, the crash analysis of the bumper beam and energy absorber was carried out and then the RSM method was used for the optimal design [15]. A RS-based design of a multi-link steering mechanism is carried out to reduce the deviation in toe angle duo to wheel travel and optimum steering error during the steering angle range [16].

In a study focusing on the design of a lightweight solar-powered vehicle suspension, a double wishbone suspension system was designed and Finite Element Analysis (FEA) was performed to investigate the differences between Macpherson and double wishbone suspension systems via static analysis [17]. In another study, ANSYS® Workbench was used for steering knuckle design and topology optimisation to reduce unspring mass [18]. Furthermore, kinematic analysis was performed on double wishbone suspension to determine camber and toe changes depending on kingpin using analytical methods [19]. Moreover, a half-car model with five Degrees of Freedom (DoF) was designed in another study where a vibration model for an electric mini off-road vehicle was built using MATLAB® software to investigate the frequency response and optimise ride comfort [20].

In this study, the design and optimisation of a front independent suspension for an L6e vehicle is carried out. Firstly, a joint force analysis was performed to determine the forces acting on the hardpoints of the system. Then, a parametric modelling process was carried out using SOLIDWORKS® software. FEA was performed on the lower wishbone under specified load conditions using ANSYS® Workbench. Design of Experiments (DoE) - Response Surface (RS) optimisation methods were used to find the optimum design in terms of weight and stress. Finally, in order to check the

safety of the obtained optimal geometry under operating conditions, an assembly model was created and a FEA was performed on this model again.

The design parameters that should be taken into consideration in front independent suspension design have been determined. The effects of these design parameters on component performance were also analysed in this study, and it is aimed to guide the designer. In general, the component design steps are summarised.

To the best of the authors' knowledge, there is no study in the open literature that provides a roadmap for the mechanical design of the suspension elements used in this class of vehicles. This study aims to fill this lack to some extent.

2. Material and method

2.1 Method

In this research, DoE and RS methods are employed to determine the optimum design of the system by modifying desired parameters within specified ranges and constraints. DoE is the examination of the system during processing by applying several tests and changing input parameters to study the system's response [21]. RS is also carried out, which involves using mathematical equations to develop and optimize the system, especially considering various parameters that affect system performance [22]. In this study, DoE and RS are performed using the ANSYS® Workbench response surface optimization tool. For a second-order response surface model, the model is defined as [23]:

$$y = \beta_0 + \sum_{i=1}^{k} \beta_i x_i + \sum_{i \le j}^{k} \beta_{ij} x_i x_j + \varepsilon \quad (1)$$

This model can also be expressed as a matrix.

$$y = X\beta + \varepsilon \quad (2)$$

Here, y is the vector of observations, X is the model matrix, β is the vector which includes the intercept parameter β_0 and the partial regression coefficients, and ε is the vector of random errors that directly affect β [21].

Central Composite Design (CCD), a method for determining optimal parameter values, is used in this study, which is available as an option in the DoE module's design table definition. This method is commonly used in the DoE studies. The main objective of CCD is to determine the effects of factors affecting a system and the optimum levels of these factors. It provides a design structure that evaluates the linear, quadratic and interactional effects of these factors. [21,22,24]. The advantages of CCD include the ability to estimate the dependent variables nonlinearity, efficiently obtain maximum information with minimum experimental data, and reduce the number of experiments required to estimate the quadratic terms in a quadratic model [25]. It is widely used for solving complex multifactorial problems. With its capability to develop accurate and reliable second-order regression models, CCD provides a deeper understanding of data and enables meaningful explanation [26]. The summary scheme of the optimisation study is summarised in Figure 2.

3. Design Steps

3.1 Load model

In the analyses performed within the scope of this study, the loads acting on the suspension system specified in the literature were used for FEA in the stress state evaluation and optimisation process of the mechanical design. In addition to the vertical load, driving, braking and lateral forces acting on a vehicle wheel in the most general driving condition [7]. These loads are shown in Figure 3 as vertical load P, side load S and braking or driving load B. These load combinations on the suspension system are applied to the wheel contact point shown as R [27]. In the literature, there are 16 main load conditions for the suspension system [28]. Bumping, brake-in- turn and cornering load conditions are considered as critical scenarios of the suspension system.

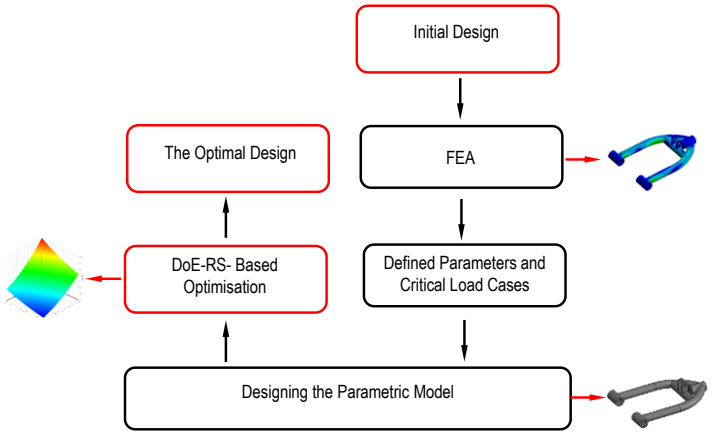

Figure 2. Summary structural optimization process of the lower wishbone

3.2. Joint Forces

FEA was performed to determine the reaction loads acting on the suspension system joints. The joint loads for three different load cases were calculated using the vector analysis. The forces applied to the contact area of the wheel are resisted and carried by the spring, control or carrier wishbones, and the steering knuckle on the load condition.

The joint forces are calculated according to the hardpoints of the suspension. The hardpoints of the system are evaluated by considering two main factors. The first one is that the instantaneous centre of the suspension arms should be near the ground to reduce the effect of camber and track width variation. Another critical factor is the distance between the centre of mass and the instantaneous centre. This distance is of crucial importance for the roll dynamics of the vehicle, especially in roll angle calculations [27,29]. Since gravity and suspension component self-weights are negligible compared to the vehicle loads, these effects are neglected in the calculations. The free body diagram of the main components of the suspension system is presented in Figure 4. Equivalent forces and moments were applied to each body within the framework of the action response principle in accordance with [29]. According to force balance:

$$\{F_{D43}\} = -\{F_{D34}\} \quad (3)$$

$$\{F_{G42}\} = -\{F_{G24}\} \quad (4)$$

$$\{F_{H45}\} = -\{F_{H54}\} \quad (5)$$

$$\{F_{C37}\} = -\{F_{C73}\} \quad (6)$$

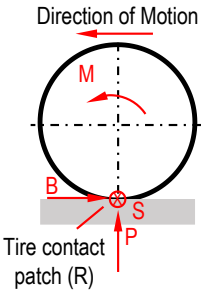

	P	S	B
Bumping	2 g	0	0
Cornering	1 g	1.25 g	0
Brake-in-Turn	1 g	0.75 g	0.75 g

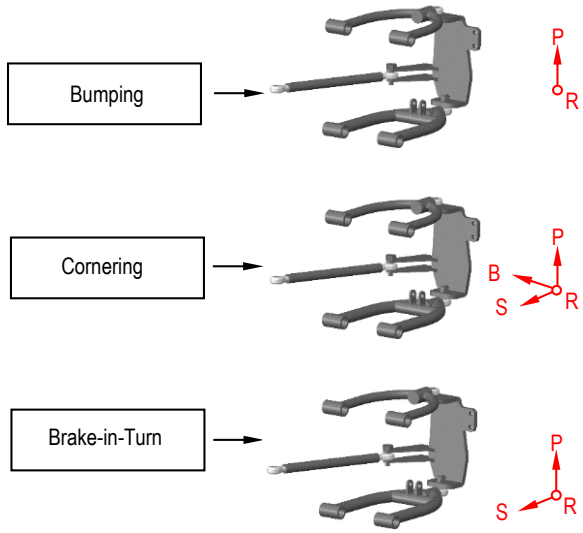

Figure 3. Critical load cases acting on the suspension system

The equivalent forces (F) and moment (M) from the lower wishbone free body diagram:

$$\sum \{F_2\} = \{0\} \quad (7)$$

$$\{F2\} = \begin{bmatrix} FFx \\ FEx \\ FGx \end{bmatrix} + \begin{bmatrix} FFy \\ FEy \\ FGy \end{bmatrix} + \begin{bmatrix} FFz \\ FEz \\ FGz \end{bmatrix} = \begin{bmatrix} 0 \\ 0 \\ 0 \end{bmatrix} \quad (8)$$

$$\sum \{F_2\} = \{0\} \quad (9)$$

$$\sum \{M_{G2}\} = \{0\} \quad (10)$$

$$\sum \{M_{G2}\} = \{RFG\}x\{F2\} + \{REG\}x\{FE\} \quad (11)$$

$$\{RFG\} = \begin{bmatrix} 0 & -RFGz & RFGy \\ RFGz & 0 & -RFGx \\ -RFGy & RFGx & 0 \end{bmatrix} \quad (12)$$

$$\{REG\} = \begin{bmatrix} 0 & -REGz & REGy \\ REGz & 0 & -REGx \\ -REGy & REGx & 0 \end{bmatrix} \quad (13)$$

The above calculations were also performed for the other bodies of the suspension. When the general calculations of the whole system are analysed, it is seen that there are 18 equations and 20 unknowns in total. Two equations are defined for the connections between the upper and lower wishbones and the chassis. In addition, it is possible to write the following two equations in accordance with [29].

$$\{FF\} \cdot \{REF\} = \{0\} \quad (14)$$

$$\{FB\} \cdot \{RAB\} = \{0\} \quad (15)$$

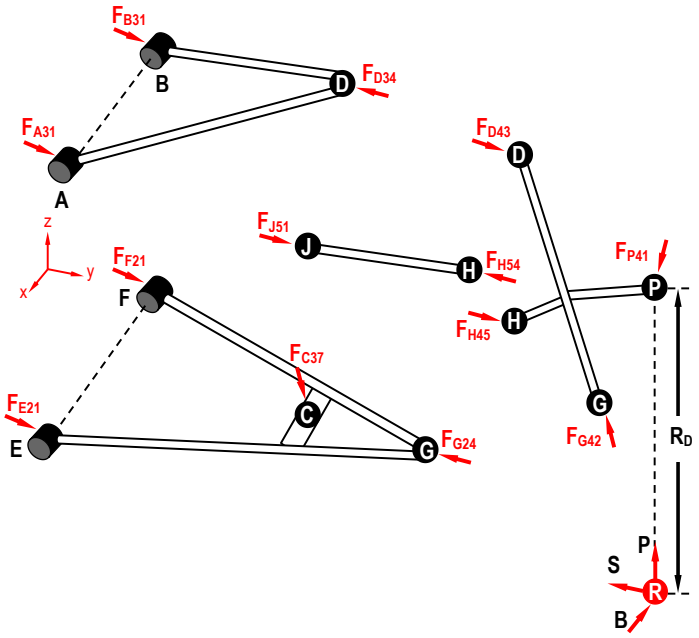

Figure 4. Free body diagram and reaction joint forces

Finally, a 19 x 19 matrix was formed as shown in Figure 5. By taking the inverse of this matrix and multiplying it with the load matrix, the equations of the free body diagram were solved [29].

The changes in the x, y and z components of the reaction forces of the carrier arm and control arm are shown in Figure 6. In the lateral load condition, it is observed that the lower wishbone spherical joint is subjected to approximately twice as much load as the upper spherical joint. In the vertical load scenario, it was found that most of the applied force was carried by the lower wishbone.

3.3 Design criteria of the lower wishbone

For the initial design of the lower wishbone, the structure was assumed as a beam. The cross-sectional dimensions were determined by elementary stress analysis. The lower wishbone is subjected to bending by the vertical component of the spring force and shearing due to the braking force. Additionally, the horizontal component of the spring force applies a compressive load on the lower wishbone. The calculations were carried out according to the condition where the spring force at the spring connection point shown as C reaches

its maximum value. With these calculations, the initial design was built by determining the value for both the outer radius (D) and the inner radius (d), which ensures the safety and durability of the lower wishbone. The initial configuration shown in Figure 7.

These bending and shear stresses are calculated by the following equations:

$$\sigma_{Bending}=\frac{M_{max}\times D}{2*I} \quad (16)$$

$$W=\pi\frac{D^4-d^4}{64} \quad (17)$$

$$\sigma_{Normal}=\frac{Fc_y}{A} \quad (18)$$

$$\sigma_B+\sigma_N<\sigma_{Safety} \quad (19)$$

In the brake-in-turn case, the stress concentration on the welding joint is critical due to the shear normal and bending loads. The forces acting on the system were taken from the analytical joint matrix given in Figure 5 and applied to the lower wishbone arm to determine the minimum thickness of the weld joint radius.

For safety reasons, the lower wishbone arm is assumed as a cantilever beam. Weld thickness value represented by “a” in Figure 8 is calculated. The safety factor used in the whole system was determined as 1.6. The normal, shear and bending stress equations:

$$\sigma_N=\frac{F}{A}=\frac{F_{Cy}-F_{Gy}}{\pi\frac{((R+2a)^2-R^2)}{4}} \quad (20)$$

$$\tau_S=\frac{F}{A}=\frac{F_{Gz}-F_{Cz}}{\pi\frac{((R+2a)^2-R^2)}{4}} \quad (21)$$

$$\tau_B=\frac{M}{W}=\frac{F_{Gz}*Lg-F_{Cz}*Lc}{\pi\frac{((R+2a)^3-R^3)}{32}} \quad (22)$$

$$\sigma_c=\sqrt{\sigma^2+\Sigma\tau^2}\leq\sigma_{yield}* \text{ Factor of Safety} \quad (23)$$

1	0	0	1	0	0	0	0	0	0	0	0	0	0	0	0	0	0	fcx	-FGx
0	1	0	0	1	0	0	0	0	0	0	0	0	0	0	0	0	0	fcy	-FGy
0	0	1	0	0	1	0	0	0	0	0	0	0	0	0	0	0	0	fcz	-FGz
0	0	0	0	-RCGy	RCGz	0	0	0	0	0	0	0	0	0	0	0	0	(RhG*fc)x	-FDx
0	0	0	RCGx	0	-RCGz	0	0	0	0	0	0	0	0	0	0	0	0	(RhG*fc)y	-FDy
0	0	0	-RCGx	RCGy	0	0	0	0	0	0	0	0	0	0	0	0	0	(RhG*fc)z	-FDz
-1	0	0	0	0	0	0	0	1	0	0	0	0	0	0	0	0	0	0	FFy
0	-1	0	0	0	0	1	0	0	1	0	0	0	0	0	0	0	0	0	FFz
0	0	-1	0	0	0	0	1	0	0	1	0	0	0	0	0	0	0	0	FEx
0	0	0	0	0	0	-RFGy	RFGz	0	-REGy	REGz	0	0	0	0	0	0	0	0	FEy
0	0	0	0	0	0	0	-RFGz	REGx	0	-REGz	0	0	0	0	0	0	0	0	FEz
0	0	0	0	0	0	RFGy	0	-REGx	REGy	0	0	0	0	0	0	0	0	0	FBx
0	0	0	-1	0	0	0	0	0	0	0	1	0	0	1	0	0	fHx	0	FBy
0	0	0	0	-1	0	0	0	0	0	0	0	1	0	0	1	0	fHy	0	FBz
0	0	0	0	0	-1	0	0	0	0	0	0	0	1	0	0	1	fHz	0	FAx
0	0	0	0	0	0	0	0	0	0	0	0	-RBDy	RBDz	0	-RADy	RADz	MHDx	0	FAy
0	0	0	0	0	0	0	0	0	0	0	RBDx	0	-RBDz	RADx	0	-RADz	MHDy	0	FAz
0	0	0	0	0	0	0	0	0	0	0	-RBDx	RBDy	0	-RADx	RADy	0	MHDz	0	FC
0	0	0	0	0	0	0	0	0	0	0	RBAx	RBAy	RBAz	0	0	0	0	0	FH

Figure 5. Reaction joint force matrix

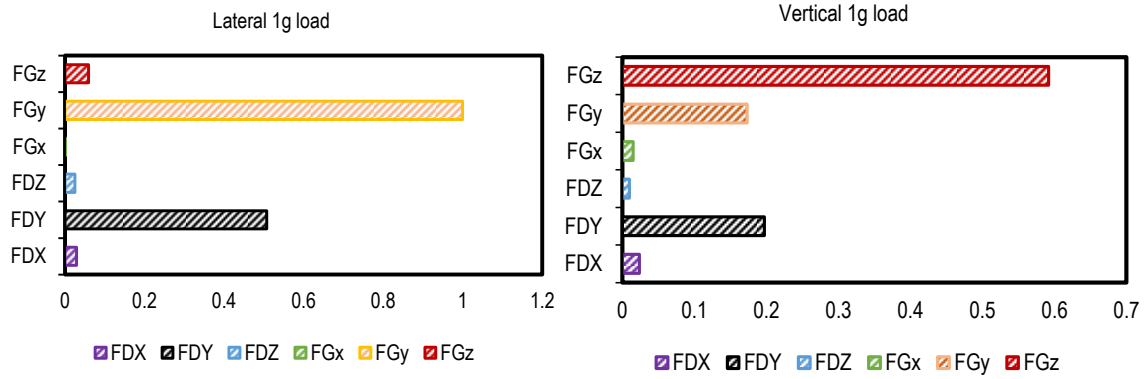

Figure 6. Reaction joint forces for load cases

In the brake-in-turn case, the stress concentration on the welding joint is critical due to the shear normal and bending loads. The forces acting on the system were taken from the analytical joint matrix given in Figure 5 and applied to the lower wishbone arm to determine the minimum thickness of the weld joint radius.

For safety reasons, the lower wishbone arm is assumed as a cantilever beam. Weld thickness value represented by “a” in Figure 8 is calculated. The safety factor used in the whole system was determined as 1.6. The normal, shear and bending stress equations:

$$\sigma_N=\frac{F}{A}=\frac{F_{Cy}-F_{Gy}}{\pi\frac{((R+2a)^2-R^2)}{4}} \quad (20)$$

$$\tau_S=\frac{F}{A}=\frac{F_{Gz}-F_{Cz}}{\pi\frac{((R+2a)^2-R^2)}{4}} \quad (21)$$

$$\tau_B = \frac{M}{W} = \frac{F_{Gz}*Lg - F_{Cz}*Lc}{\frac{\pi((R+2a)^3 - R^3)}{32}} \quad (22)$$

$$\sigma_c = \sqrt{\sigma^2 + \Sigma\tau^2} \leq \sigma_{yield} * \text{Factor of Safety} \quad (23)$$

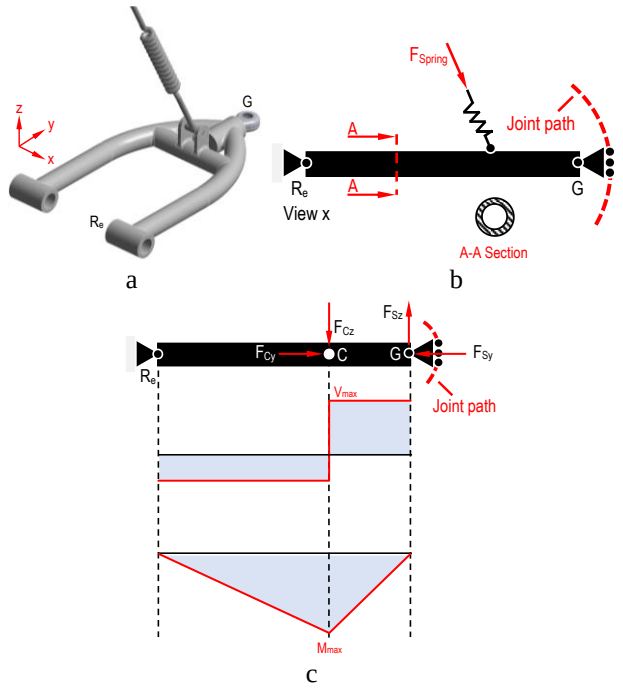

Figure 7. Load model of the lower wishbone

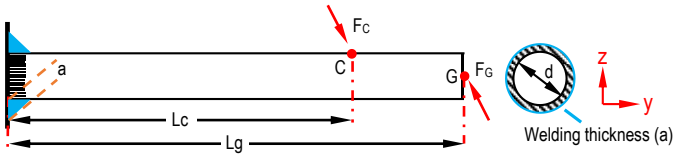

Figure 8. Defining the welding thickness of the lower wishbone arm

4. FEA model of the suspension system

The CAD model built parametrically in SOLIDWORKS® was transferred to ANSYS® Workbench for FEA. In the suspension system, the lower wishbone is considered as a critical component since the vertical force due to the vehicle weight is transferred from the spring to the lower wishbone. In the FEA model, a mesh structure consisting of 441,031 nodes and 254,729 elements was created using the SOLID187 element consisting of ten nodes. The mesh structure is shown in Figure 9. Some of the structural elements utilised in the analysis have been simplified due to the confidentiality policy of the project partner company.

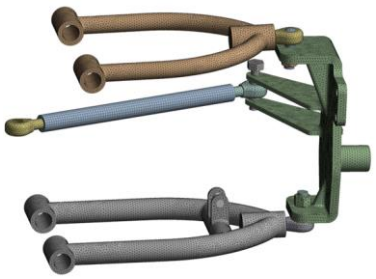

Figure 9. The mesh structure of FEA model

Firstly, in order to determine the stress conditions of the lower wishbone, two FEA models, a single component and a quarter vehicle, were built. The single component model is fixed through the wishbone bushings and the force is applied through the spherical and the spring joint of the lower arm. Then, to verify the stress values obtained from the single-component analysis, a quarter vehicle analysis was carried out by adding a revolute joint to the wishbone bushings, a ball joint to the knuckle linkages and a spring element. The spring is modelled with a pin joint in the bushing to transfer its force to the lower wishbone. In this analysis, the force was applied at the wheel contact point (R). The analysis models are given in Figure 10. Here, Fixed Joint "F", Revolute Joint (Ground) "R_e", Spherical Joint "S", Spherical Joint (Ground) "S_e", Contact Patch "R" and Dynamic Radius of the Tire "R_d" are named.

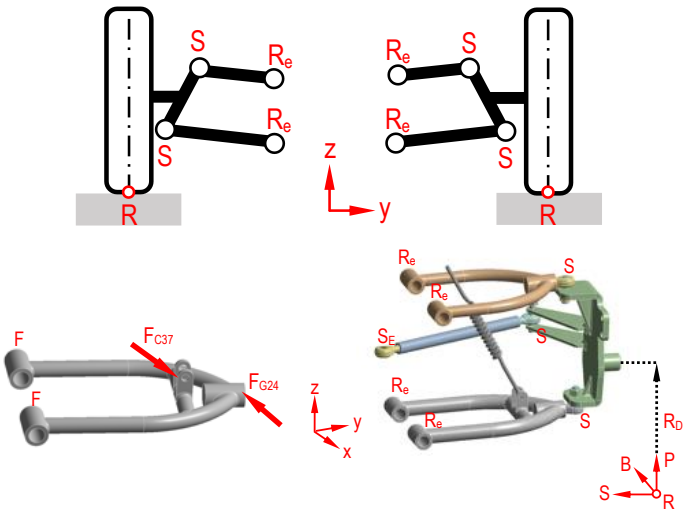

Figure 10. Boundary conditions used in FEA models

5. Result and Discussion

5.1 Critical load cases

The FEA of the quarter vehicle model was performed for three different load cases: bumping, cornering and brake-in-turn. In the analyses results shown in Figure 11, the stress values obtained are represented as the ratio of the maximum equivalent stress values occurring in the critical stress concentration regions. The brake-in-turn load condition was identified as the critical load case because of the braking force in addition to the spring load that supports and transmits the vehicle weight.

5.2 DoE based optimisation

The DoE-RS module of ANSYS® Workbench was used to determine the optimal arm design that is lightweight and at the same time stress safe. Firstly, the critical region was determined according to the FEA result. In this region, it was determined that both the stress value is maximum and it is subjected to tensile stress as shown in Figure 12.

Then, a parametric model of the initial design was built using SolidWorks®. For the DoE-based optimisation, the outer diameter (D), wall thickness (t) and tube curvature radius (R) were selected as design parameters as shown in Figure 13.

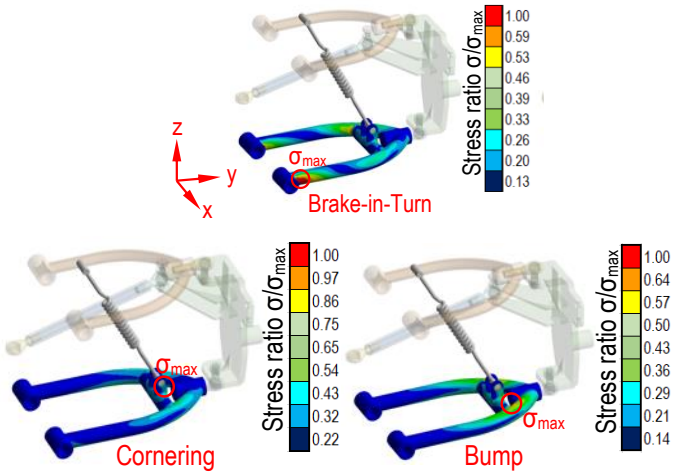

Figure 11. FEA of the lower wishbone for the load cases in quarter vehicle model

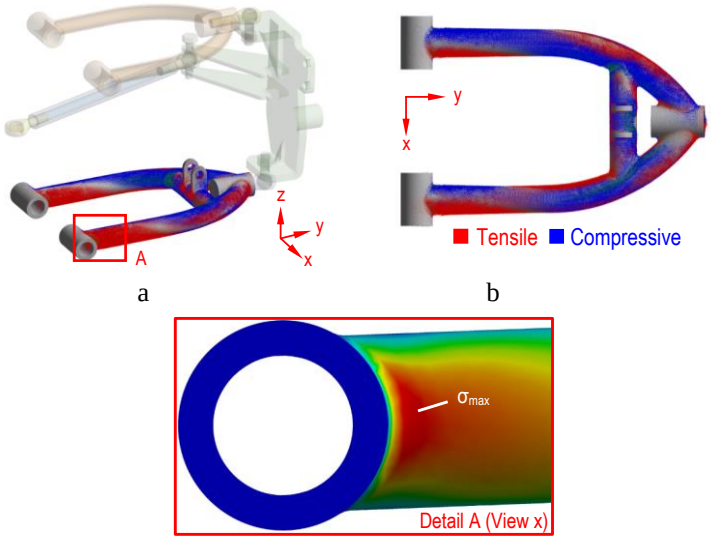

Figure 12.a and b. principal stress of the lower wishbone, c. the critical area

The current state of all parameters is considered as a unit and the maximum and minimum values are shown in Table 1 as multiples of this value in accordance with the confidentiality policy of the company. Mass, maximum equivalent stress and total deformation were defined as output parameters. As a result of the DoE performed over the critical load condition, RS graphs were obtained with these parameters.

Figure 14 shows the effect of the design parameters on the output values. When the graph is analysed, it was seen that the outer diameter (D) has the greatest effect especially on the maximum equivalent stress. As the diameter increases, the structural strength increases while the total deformation decreases. Thickness (t) was found to have the most sensitive effect on weight. Increasing the thickness significantly increases the mass but has a minimal effect on the equivalent stress. The curvature radius (R) has similar effects on both mass and maximum equivalent stress, but its effect on deformation is more pronounced. Increasing the curvature radius may affect the elastic behaviour of the structure, making it more sensitive to deformation.

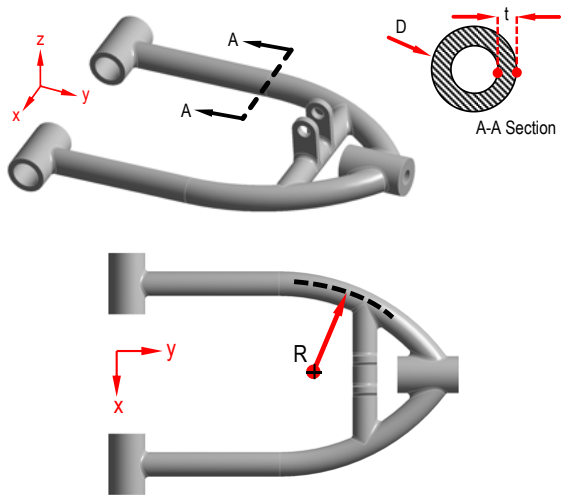

Figure 13. The design parameters of the lower wishbone arm

Table1. Parameters variation range

Parameters	Variation Range
t	1.5t < t < 2.2t
D	20D < D < 25D
R	130R < R < 165R

As a result, ensuring the equilibrium between design parameters is critical to achieve the desired performance. For example, while the outer diameter can be increased to minimise deformation, this must be balanced with weight optimisation.

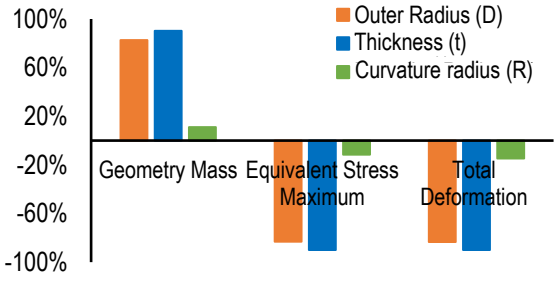

Figure 14. Effective percentage of the design parameters effecting the lower wishbone

The RS plots generated for mass, equivalent stress and total deformation using the defined input parameters are shown in Figure 15. These graphs provided the optimum design points to be determined in the optimisation module. In the optimisation process, minimising the equivalent stress and mass was determined as the main design objective.

A final design was created by using the values obtained as a result of the optimisation. FEA was applied to this final model again. Six points (P_1-P_6) were randomly selected from this region in order to examine the stress variation in the critical region. The stress change between the initial design and the final design is shown in Figure 16. In this graph, point P_6 of the final design is selected as reference.

Other point's stresses were calculated by ratio to the stress at this point. When the graph is examined, it was observed that the stress values of the final design were lower than the initial design at all points. The percentage decrease values from P_1 to P_6 were determined as 42.94%, 33.75%, 26.92%, 32.01%, 41.32% and 40.31%, respectively.

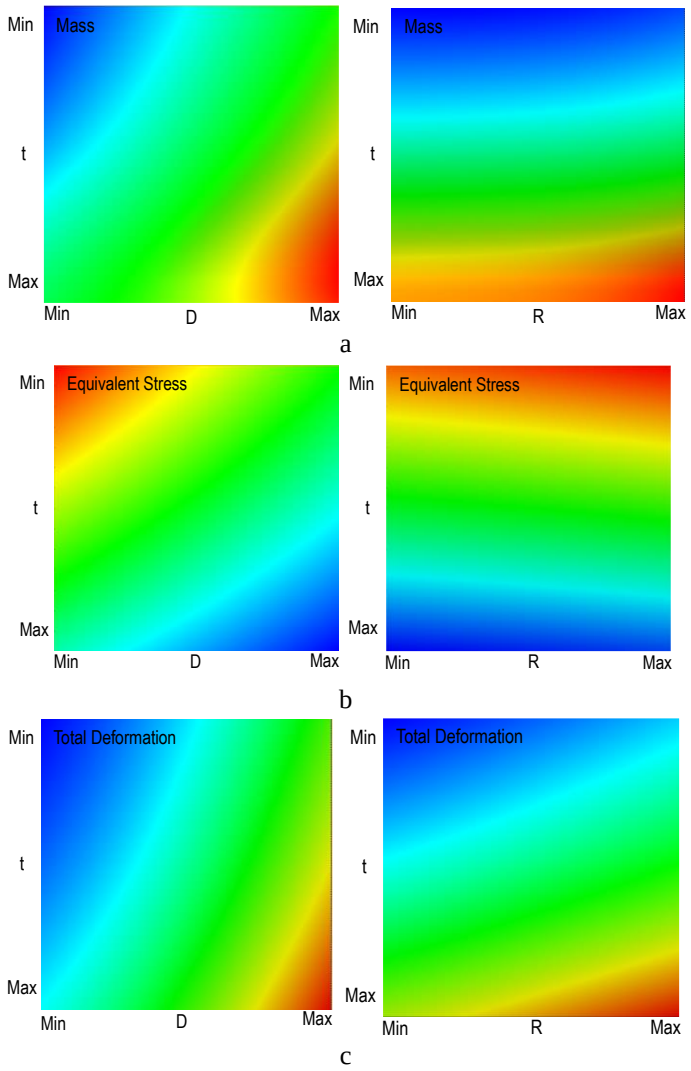

Figure 15. Response surfaces of the parameters, a- mass (kg), b- Equivalent Stress (MPa), c- Total Deformation (mm)

A final design was created by using the values obtained as a result of the optimisation. FEA was applied to this final model again. Six points (P_1-P_6) were randomly selected from this region in order to examine the stress variation in the critical region. The stress change between the initial design and the final design is shown in Figure 16. In this graph, point P_6 of the final design is selected as reference. Other point's stresses were calculated by ratio to the stress at this point. When the graph is examined, it was observed that the stress values of the final design were lower than the initial design at all points. The percentage decrease values from P_1 to P_6 were determined as 42.94%, 33.75%, 26.92%, 32.01%, 41.32% and 40.31%, respectively.

The analysis results of the quarter vehicle model and the single component- based analysis model built with the final design are compared. According to Figure 17, the maximum stress values were represented as a percentage and an error rate of approximately 2.27% was determined. In addition, the critical zone identified as Region A in the quarter vehicle model analysis was found to match the critical Region B in the component-based analysis.

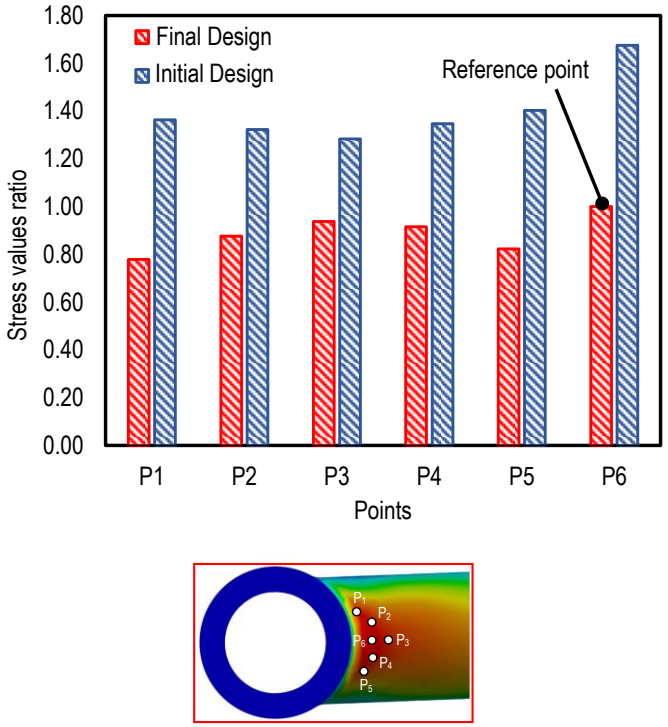

Figure 16. Response surfaces of the parameters, a- mass (kg), b- Equivalent Stress (MPa), c- Total Deformation (mm)

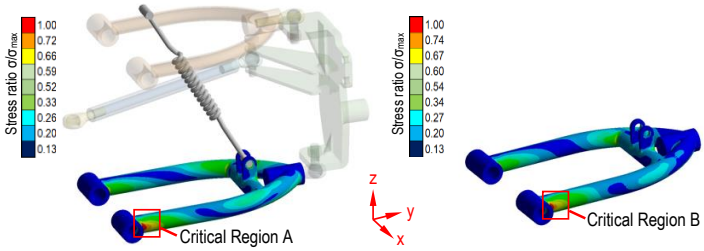

Figure 17. Comparison of the optimization singular and quarter vehicle model

6. Conclusion

In this study, the design, analysis and optimisation of the front independent suspension system of an electric L6 class vehicle were investigated. Firstly, different load cases and their effects at the joint points are analysed. Then, two models were built for FEA to be performed in ANSYS® Workbench using SOLIDWORKS® software. As a result of the FEA, the critical load model was identified. Also, the region subjected to both tensile and maximum stress was defined as the critical region. In the optimisation stage, the outer diameter (D), wall thickness (t) and radius of curvature radius (R) were selected as input parameters, while mass, equivalent stress and total deformation were chosen as output parameters. For optimal values, low mass and low stress design constraints were defined for the software and new parameter values were obtained for the final design.

Among these points, the highest stress reduction was obtained at point P_1 with approximately 43%. The results of the study also highlight the critical design parameters that should be taken into account in the design of independent suspension for electric L6 vehicles. The effects of these design parameters on the output parameters are also analysed. Thickness was found to have the highest effect on all output parameters. This study provides guidelines for the design of suspension systems for similar class vehicles.

Conflict of Interest Statement

The authors must that there is no conflict of interest in the study.

Acknowledgment

This study was supported by TÜBİTAK (The Scientific and Technological Research Council of Türkiye) within the framework of 2209-B program. The Authors acknowledge the technical support of Mr. Decan Alpargun, the founder of AZR Engineering. The authors also acknowledge Mr. Sefa Temur for the contribution to Figure 1.

CRediT Author Statement

Mohammad Nassar: Data curation, Formal analysis, Software, Writing - original draft, **Kübra Polat:** Software, Writing - review & editing, Visualization, **Yağmur Koçlu:** Solid Modelling, Data curation, **Mehmet Murat Topaç:** Conceptualization, Supervision, Writing - review & editing

References

1. Shaw, R. P. (1992). The impact of population growth on environment: The debate heats up. Environmental Impact Assessment Review, 12(1-2), 11-36.
2. Schafer, A. (1998). The global demand for motorized mobility. Transportation Research Part A: Policy and Practice, 32(6), 455-477.
3. Teixeira, A. C. R., da Silva, D. L., Machado Neto, L. D. V. B., Diniz, A. S. A. C., & Sodré, J. R. (2015). A review on electric vehicles and their interaction with smart grids: the case of Brazil. Clean Technologies and Environmental Policy, 17, 841-857. https://doi.org/10.1007/s10098-014-0865-x
4. Borowski, P. F. (2022). Mitigating climate change and the development of green energy versus a return to fossil fuels due to the energy crisis in 2022. Energies, 15(24), 9289. https://doi.org/10.3390/en15249289
5. European Commission. (2011). A roadmap for moving to a competitive low carbon economy in 2050 (COM/2011/144 final). European Union. Retrieved April 3, 2024, from https://eur-lex.europa.eu/LexUriServ/LexUriServ.do?uri=COM:2011:0144:FIN:EN:PDF
6. Ewert, A., Schmid, S., Brost, M., Davies, H., & Vinckx, L. (2021). Small electric vehicles: An international view on light three- and four-wheelers (p. 189). Springer Nature. https://doi.org/10.1007/978-3-030-65843-4
7. Jazar, R. N. (2008). Vehicle dynamics (Vol. 1). Springer.
8. Sancibrian, R., Garcia, P., Viadero, F., Fernandez, A., & De-Juan, A. (2010). Kinematic design of double-wishbone suspension systems using a multiobjective optimisation approach. Vehicle System Dynamics, 48(7), 793–813. https://doi.org/10.1080/00423110903156574
9. Littman, M. L. (1996, April). Simulations combining evolution and learning. In Santa Fe Institute Studies in the Sciences of Complexity-Proceedings Volume (Vol. 26, pp. 465–478). Addison-Wesley Publishing Co.
10. Reimpell, J., Stoll, H., & Betzler, J. (2001). The automotive chassis: Engineering principles. Elsevier.
11. Mahla, S. K., Safieddin Ardebili, S. M., Mostafaei, M., Dhir, A., Goga, G., & Chauhan, B. S. (2024). Multi-objective optimization of performance and emissions characteristics of a variable compression ratio diesel engine running with biogas-diesel fuel using response surface techniques. Energy Sources, Part A: Recovery, Utilization, and Environmental Effects, 46(1), 15737–15754. https://doi.org/10.1080/15567036.2020.1813847
12. Ardebili, S. M. S., Calam, A., Solmaz, H., Böğrek, A., & Haşimoğlu, C. (2024). Improving the combustion process of a homogeneous charge compression ignition engine running with triple fuel blend using response surface methodology. Journal of the Brazilian Society of Mechanical Sciences and Engineering, 46(8), 486. https://doi.org/10.1007/s40430-024-05060-0
13. Kocakulak, T., Arslan, T. A., Şahin, F., Solmaz, H., Ardebili, S. M. S., & Calam, A. (2023). Determination of optimum operating parameters of MWCNT-doped ethanol fueled HCCI engine for emission reduction. Science of The Total Environment, 895, 165196. https://doi.org/10.1016/j.scitotenv.2023.165196
14. Bildirici, D., Topaç, M. M., Polat, K., Zavrak, T., & Arman, Y. (2024). Failure analysis-based mass reduction of an aluminium alloy engine mounting bracket using Design of Experiments approach. Engineering Failure Analysis, 166, 108927. https://doi.org/10.1016/j.engfailanal.2024.108927
15. Yildirim, A., Demirci, E., Karagöz, S., Özcan, Ş., & Yildiz, A. R. (2023). Experimental and numerical investigation of crashworthiness performance for optimal automobile structures using response surface methodology and oppositional based learning differential evolution algorithm. Materials Testing, 65(3), 346–363. https://doi.org/10.1515/mt-2022-0304
16. Topaç, M. M., Deryal, U., Bahar, E., & Yavuz, G. (2015). Optimal kinematic design of a multi-link steering system for a bus independent suspension: An application of response surface methodology. Mechanics, 21(5), 404–413. https://doi.org/10.5755/j01.mech.21.5.11964
17. Odabaşı, V., Maglio, S., Martini, A., & Sorrentino, S. (2019). Static stress analysis of suspension systems for a solar-powered car. FME Transactions, 47(1), 70–76. https://doi.org/10.5937/fmet1901070o
18. Li, J., Tan, J., & Dong, J. (2020). Lightweight design of front suspension upright of electric formula car based on topology optimization method. World Electric Vehicle Journal, 11(1), 15. https://doi.org/10.3390/wevj11010015
19. Tanik, E., & Parlaktaş, V. (2015). Design of a very light L7e electric vehicle prototype. International Journal of Automotive Technology, 16, 997–1005. https://doi.org/10.1007/s12239-015-0102-6
20. Yu, B., Wang, Z., Zhu, D., Wang, G., Xu, D., & Zhao, J. (2020). Optimization and testing of suspension system of electric mini off-road vehicles. Science Progress, 103(1), 0036850419881872. https://doi.org/10.1177/0036850419881872
21. Montgomery, D. C. (2000). Design and analysis of experiments (5th ed.). John Wiley & Sons.
22. Myers, R. H., Montgomery, D. C., & Anderson-Cook, C. M. (2009). Response surface methodology: Process and product optimization using design of experiments (3rd ed.). John Wiley & Sons.

23. Han, H., & Park, T. (2004). Robust optimal design of multi-body systems. Multibody System Dynamics, 11, 167–183. https://doi.org/10.1023/B:MUBO.0000025414.28789.34
24. Aydın, M., & Ünlüsoy, Y. S. (2012). Optimization of suspension parameters to improve impact harshness of road vehicles. International Journal of Advanced Manufacturing Technology, 60, 743–754. https://doi.org/10.1007/s00170-011-3589-7
25. Rodriguez, R., Mazza, G., Zalazar-García, D., Fernandez, A., & Fabani, M. P. (2023). Polyphenol extraction from bio-wastes: Optimization and kinetic analysis. Studies in Natural Products Chemistry, 79, 317–339. https://doi.org/10.1016/B978-0-443-18961-6.00010-X
26. Gregor, M., Grznar, P., Mozol, S., & Mozolova, L. (2023). Design of simulation experiments using Central Composite Design. Acta Simulatio, 9(2). https://doi.org/10.22306/asim.v9i2.99
27. Topaç, M. M., Olguner, C., & Bahar, E. (2022). Development of an independent front suspension for truck tractors. Mechanics, 28(2), 121–129. https://doi.org/10.5755/j02.mech.29092
28. Heißing, B., Ersoy, M., & Gies, S. (Eds.). (2011). Fahrwerkhandbuch (738 p.). Vieweg+Teubner Verlag, Springer Fachmedien Wiesbaden GmbH.
29. Blundell, M., & Harty, D. (2004). The multibody systems approach to vehicle dynamics. Elsevier.

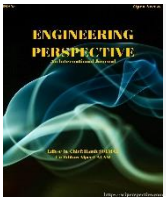

e-ISSN:2757-9077

ENGINEERING PERSPECTIVE

https://sciperspective.com/ Research Paper

Effect of Different Benzoylthiourea Additives to Gasoline on Engine Noise and Vibration in a Spark Ignition Engine

Sertaç Coşman[1*], Samet Çelebi[2,3]

[1]*Mechanical Engineering Department, Faculty of Engineering-Architecture, Burdur Mehmet Akif Ersoy University, Burdur, 15200, Turkey*

[2]*Motor Vehicles and Transportation Technologies Department, Arifiye Vocational School, Sakarya University of Applied Sciences, Sakarya, 54580, Turkey*

[3]*Automotive Technologies Application and Research Center, Sakarya University of Applied Sciences, Sakarya, 54580, Turkey*

ABSTRACT

This study investigates the effects of dichloromethane (DCM) and benzoylthiourea derivatives (LH1 and LH2) at co ncentrations of 25 ppm, 50 ppm, and 100 ppm on engine noise and vibration across various load conditions. The res ults reveal that noise and vibration levels increased with engine load for all fuel blends, with significant variations de pending on the additive type and concentration. Adding DCM to gasoline caused slight increases in both noise (up to 1.29%) and vibration (up to 6.14%) due to its higher density and altered combustion dynamics. LH1 consistently incr eased noise and vibration levels, with the highest increases observed at 100 ppm (6.77% noise and 23.38% vibration at no load), likely due to its volatile nature and destabilizing effects on combustion. Conversely, LH2 significantly red uced noise and vibration, particularly at 25 ppm and 50 ppm concentrations. At 100 ppm, LH2 reduced noise by 1.9 8% and vibration by 6.85% at full load compared to gasoline, attributed to its superior knock resistance and stabilizin g effects on combustion. The findings highlight LH2 as a promising additive for applications requiring reduced engine noise and vibration, particularly at higher loads. In contrast, LH1's tendency to amplify noise and vibration suggests a need for optimization before practical implementation. This study underscores the critical role of additive composition and concentration in influencing engine performance, providing valuable insights for developing fuel blends with impr oved acoustic and operational characteristics.

Keywords: Benzoylthiourea; Dichloromethane; Engine noise, Engine vibration; Gasoline engine

History
Received: 17.09.2024
Accepted: 12.01.2025

How to cite this paper: Coşman, S., Çelebi, S., (2025). Effect of Different Benzoylthiourea Additives to Gasoline on Engin e Noise and Vibration in a Spark Ignition Engine. Engineering Perspective, 5 (1), 31-40. http://dx.d oi.org/10.29228/eng.pers.79928

Author Contacts
**Corresponding Author*
e-mail addresses : scosman@mehmetakif.edu.tr, scelebi@subu.edu.tr

1. Introduction

The growing demand for high-performance internal combustion (IC) engines has intensified efforts to optimize engine efficiency [1-4]. However, alongside advancements in engine performance, addressing challenges such as noise and vibration, both of which have mechanical and environmental implications, remains a critical concern. Excessive noise and vibration not only diminish passenger comfort but also contribute to environmental noise pollution. Moreover, they accelerate engine wear and adversely affect operational efficiency. These challenges become increasingly significant as modern engines aim for higher power outputs and improved fuel efficiency while adhering to stricter environmental regulations [5-8].

Engine noise and vibration are complex phenomena influenced by a variety of factors, including combustion processes, mechanical imbalances, and fuel properties. Researchers are actively exploring strategies to mitigate these effects, with one promising approach being the modification of fuel composition through alternative fuel additives. These additives have the potential to alter combustion dynamics, providing a means to reduce noise and vibration while pre-

serving or even enhancing engine performance. Given the significance of noise and vibration in IC engines, fuel additives have become a key area of focus for researchers, particularly in recent years.

The literature includes significant studies on the impact of fuel additives used in IC engines on engine noise and vibration levels. Elkelawy et al. conducted a review study examining the effects of organic compound additives on biodiesel fuel blends to assess diesel engine vibration and noise characteristics. The study reported reductions of up to 5% in engine vibration levels and up to 7% in noise levels [9]. Bharath and Selvan carried out experimental research to evaluate the impact of isobutanol addition to methanol-gasoline blends on the noise, vibration, and emission characteristics of an unmodified automotive spark ignition (SI) engine. Their findings indicated that the blended fuels produced higher overall noise levels but lower accelerations in the vertical and longitudinal directions compared to pure gasoline [10]. Wirawan et al. performed experimental analyses to investigate the effect of adding methanol as a non-fossil fuel mixture to RON 88 gasoline. The results showed that the highest engine vibration occurred in the vertical radial direction, measuring 36 m/s² with methanol and 34 m/s² without methanol, at engine speeds of 1200 to 1600 rpm. Engine noise was higher for methanol-blended fuel, with a maximum value of 86.4 dB, compared to 85.7 dB for pure gasoline [11]. Ağbulut et al. studied the effects of blending waste cooking oil methyl ester with various metal oxide-based nanoparticles on the emissions, performance, vibration, and noise characteristics of a single-cylinder diesel engine. The results suggested that the addition of nanoparticles to B10 slightly reduced noise and vibration levels [12]. Xu et al. investigated the vibration, wear, and emission characteristics of three types of composite additives with detergent and synergist functions in a diesel engine. Their findings revealed that Type III additives exhibited moderate combustion intensity and mechanical stress, demonstrating an effective capability for vibration control, with a slight 7.6% reduction in mechanical vibration during the running-in period [13]. Wei et al. found that methanol-diesel blends, particularly those incorporating nanoparticle additives, can increase maximum in-cylinder pressure and slightly shorten the ignition delay, both of which influence noise and vibration. However, these blends also tend to result in higher NO_x emissions [14]. Similarly, Rao et al. observed that methanol and biodiesel blends in diesel engines exhibit smoother combustion and reduced vibration, suggesting improved torque conversion and reduced combustion heterogeneity [15]. Sani et al. conducted an experimental study on a four-cylinder gasoline engine powered by a methanol-gasoline fuel blend. Their results revealed that the methanol-gasoline mixture produced the highest levels of vibration and noise within the 1200–1400 rpm range, whereas pure gasoline exhibited the lowest vibration and noise levels between 1000 and 1400 rpm. The tests further demonstrated that the engine's operation with the methanol-gasoline blend led to significant frequency variations, ranging from 148 to 173 Hz [16]. Sharma et al. carried out a study using a single-cylinder gasoline direct injection (GDI) research engine to examine its noise and vibration characteristics. Their findings revealed that methanol-gasoline blends produced notably higher in-cylinder pressure, increased heat release rates, greater rates of pressure rise, and elevated cumulative heat release compared to pure gasoline. These factors had a significant impact on the engine's noise and vibration behavior [17]. Borg et al. investigated methods to reduce noise and vibration in the high-pressure fuel system of a GDI system, focusing on optimizing the mechanical design features of the outlet valve. Their findings demonstrated noise reductions ranging from 2 to 6 dBA across various characteristic frequency levels of the GDI system. [18]. Keskin investigated the vibration characteristics and noise emissions of a two-stroke SI engine fueled with ethanol-gasoline blends. The study revealed significant changes in engine vibration behavior at 1500 and 2500 rpm when using the blended fuels. The vibration amplitudes and noise emissions of the engine exhibited an increasing trend compared to those observed with pure gasoline [19]. Faraji et al. examined the impact of magnetized ethanol-gasoline fuel blends on the vibration and sound characteristics of a single-cylinder gasoline engine. Their findings showed that the highest average sound pressure level (88.41 dB) was observed with pure gasoline at a magnetic intensity of 7000 G, while the lowest value (78.94 dB) was recorded with a 10% ethanol blend and a magnetic intensity of 5300 G. Additionally, vibration levels were found to decrease as the ethanol concentration increased up to 10% [20]. Uyumaz et al. carried out an experimental investigation to evaluate the impact of adding lacquer thinner to gasoline on the performance and emission characteristics of a SI engine. The findings revealed a reduction in HC emissions by 3.4%, 5.6% and 12.13% with lacquer thinner concentrations of 10%, 20% and 30% (LT10, LT20, and LT30), respectively, compared to pure gasoline. Similarly, CO emissions decreased by 1.09%, 2.18% and 3.56% for the same lacquer thinner concentrations [21]. Aydoğan performed a study to explore the influence of ethanol on the combustion, performance, and emission characteristics of a single-cylinder homogeneous charge compression ignition (HCCI) engine. The results demonstrated a reduction in HC emissions with the use of a fuel blend comprising 15% ethanol and 85% n-heptane [22]. Overall, fuel additives have the potential to enhance engine performance and mitigate unavoidable emissions, although they may slightly increase noise and NO_x emissions. Additionally, blends containing biofuels have shown promise in reducing vibration and noise, making them attractive candidates for achieving cleaner and quieter engine operations.

In recent years, extensive research has been conducted on fuel additives with varied chemical compositions for use in IC engines. These studies focus on improving combustion efficiency and engine performance by employing fuel additives with high oxygen content. Among the chemicals being explored are benzoylthiourea and its derivatives, which have garnered significant attention for their contributions to advancements in medicinal and coordination chemistry [23–25]. Thiourea derivatives and their transition metal complexes exhibit a wide array of biological and medicinal properties, including antibacterial, antifungal, antiviral, and antitumor activities [26,27].

Numerous studies on the use of benzoylthiourea derivatives as fuel additives have been documented in the literature. While limited, research suggests that benzoylthiourea derivatives can enhance fuel properties in IC engines. Keskin et al. investigated the effects of adding bis-(N,N-dimethyl-N'-2-chlorobenzoylthioureato) palladium (II) (PdL_2) and bis-(N,N-dimethyl-N'-2-chlorobenzoylthioureato) nickel (II) (NiL_2) complexes as metal-based additives to diesel fuel. The findings revealed that while PdL_2 and NiL_2 did not significantly alter the fundamental fuel properties, they reduced the pour point and increased the flash point of the diesel. Emission reductions were significant, with CO decreasing by 68.15%, NOx by 34.93%, and

smoke by 50.24%. Additionally, the brake-specific fuel consumption (BSFC) decreased by approximately 7.75% [28]. In another study, Keskin et al. examined the impact of diesel-biodiesel blends containing palladium-based and acetylferrocene additives on engine performance and emissions. Bis-(N,N-dimethyl-N'-2-chlorobenzoylthioureato) palladium (II) (PdL_2) was synthesized as a palladium-based additive and added to the blended fuels at a concentration of 25 ppm. The study assessed the additives' effects on emissions, performance, and vibration. The results indicated that the viscosity, density, and pour point of the blended fuels increased, while the cetane number and calorific value decreased. Although the metal-based additives did not significantly affect cylinder pressure, they substantially reduced particulate matter (PM) and CO emissions by up to 60.07% and 51.33%, respectively [29]. Gao et al. explored the application of urea-thiourea complexation as a method to enhance the octane number of FCC gasoline by extracting n-alkanes. The addition of thiourea proved highly effective in isolating n-alkanes from FCC gasoline, markedly decreasing their concentration in the remaining liquid phase. Their findings highlighted the remarkable efficacy of the urea-thiourea complexation process in improving the octane quality of gasoline [30].

Thiourea and its derivatives play a crucial role in the fields of medicine and healthcare. This study focuses on examining the effects of two specific compounds, N-((5-chloropyridin-2-yl)carbamothioyl)furan-2-carboxamide (HL1) and N-((2-chloropyridin-3-yl)carbamothioyl)thiophene-2-carboxamide (HL2) on the noise and vibration levels of a gasoline-powered engine. These benzoylthiourea derivatives and their complexes with cobalt(II), nickel(II), and copper(II) were synthesized following the method previously reported by Yeşilkaynak et al. [31,32]. For experimental evaluation, the additives were dissolved in dichloromethane and blended with gasoline at concentrations of 25 ppm, 50 ppm and 100 ppm. The noise and vibration levels of the single-cylinder gasoline engine were then analyzed to determine the effects of these fuel additives.

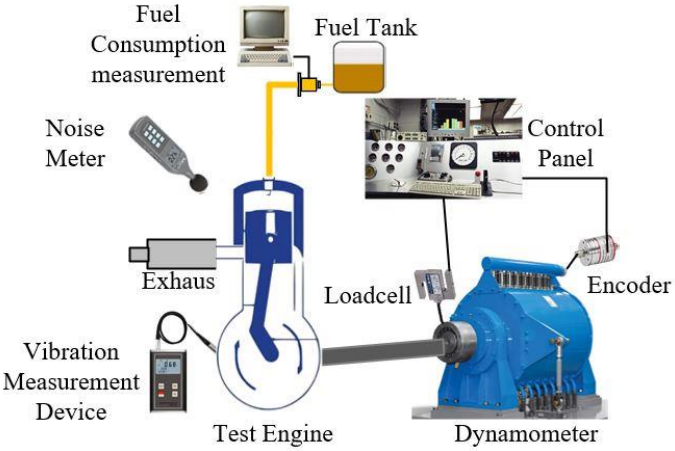

Figure 1. Experimental test setup

2. Materials and Methods

The experiments were performed on a single-cylinder, air-cooled, four-stroke gasoline engine to assess the impact of various fuel mixtures on engine noise and vibration. The engine was operated at a steady speed of 2500 rpm under varying load conditions, ranging from 0% to 100%. An engine dynamometer was employed to accurately control and monitor the engine load throughout the testing process. The experimental setup also incorporated systems for noise measurement and vibration analysis to record essential performance metrics. A schematic representation of the experimental setup is provided in Figure 1.

Noise levels were measured using a calibrated sound level meter positioned 1 meter from the engine. The meter was configured to record in the A-weighted decibel (dBA) scale, which closely reflects the human ear's sensitivity to various frequencies. Measurements were taken at each load level, with data recorded every second and averaged over a 2-minute period. Vibration levels were assessed using a three-axis accelerometer mounted on the engine block. The accelerometer was connected to a data acquisition system, recording vibration in terms of acceleration (m/s^2). Measurements were taken along the X, Y, and Z axes to capture the engine's overall vibration behavior. The vibration data from all three axes were averaged to provide a single overall vibration level for each fuel mixture and load condition. The testing procedure for each fuel mixture was as follows: The engine was pre-warmed for 10 minutes using G fuel to stabilize operating conditions. Throughout the experiment, the engine speed was maintained at a constant 2500 rpm. Fuel mixtures were tested under engine loads of 0%, 25%, 50%, 75%, and 100%. Noise and vibration levels were recorded after a 2-minute stabilization period at each load level. To prevent cross-contamination between fuel mixtures, the engine was run on pure gasoline between tests. Each fuel mixture was tested three times to ensure the repeatability and reliability of the results. Test engine properties are provided in Table 1.

Table 1. Test engine specifications

Brand&Model	Honda GX200
Bore x stroke (mm x mm)	68 x 54
Cylinder volume (cm^3)	196
Number of cylinders	1
Cooling type	Air cooled
Max. power (Hp, @3600 rpm)	6.5
Max. torque (Nm, @2500 rpm)	13.24
Compression ratio	8.5:1

A series of fuel mixtures, detailed in Table 2, range from G, which serves as the baseline fuel, to various blends containing different additive ratios. These blends were carefully prepared in the laboratory using precise volume measurements and thorough mixing to ensure uniform consistency. Initially, benzoylthiourea derivative additives (HL1: $C_{11}H_8ClN_3O_2S$ and HL2: $C_{11}H_8ClN_3OS_2$) were dissolved in 5 mL of DCM at a concentration of 25 ppm, 50 ppm and 100 ppm. The resulting solutions were then added to 1000 mL of G. DCM serves as a versatile solvent for dissolving a wide range of organic compounds in numerous chemical processes. It is produced through two primary methods: the hydrochlorination of methanol and the direct chlorination of methane [33]. The chemical structures of HL1 and HL2 are given in Figure 2 and Figure 3.

Table 2. Test fuel mixtures

Test Fuels	Mixing Ratios
G	100% Gasoline (1000 mL)
G+ DCM	100% Gasoline + 5 mL DCM
G+ DCM + HL1 (25 ppm)	100% Gasoline + 5 mL DCM with HL1 (25 ppm)
G+ DCM + HL2 (25 ppm)	100% Gasoline + 5 mL DCM with HL2 (25 ppm)
G+ DCM + HL1 (50 ppm)	100% Gasoline + 5 mL DCM with HL1 (50 ppm)
G+ DCM + HL2 (50 ppm)	100% Gasoline + 5 mL DCM with HL2 (50 ppm)
G+ DCM + HL1 (100 ppm)	100% Gasoline + 5 mL DCM with HL1 (100 ppm)
G+ DCM + HL2 (100 ppm)	100% Gasoline + 5 mL DCM with HL2 (100 ppm)

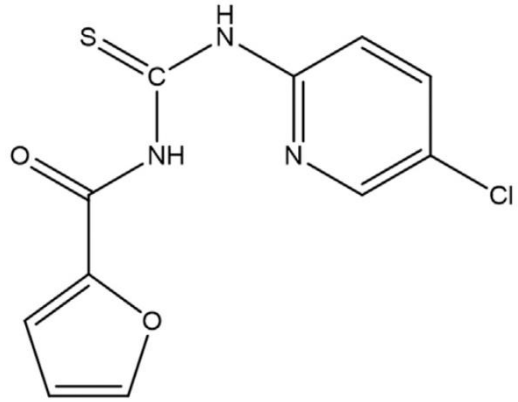

Figure 2. Chemical structure of N-((5-chloropyridin-2-yl)carbamothioyl)furan-2-carboxamide (HL1) [31]

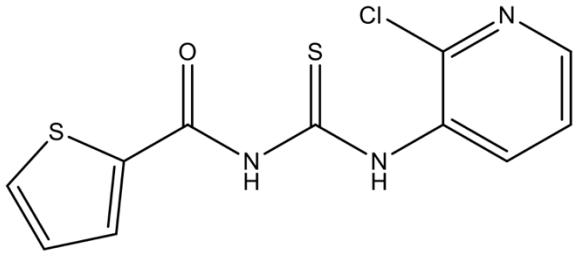

Figure 3. Chemical structure of N-((2-chloropyridin-3-yl)carbamothioyl) thiophene-2-carboxamide (HL2) [32]

Table 3 provides an overview of the fuel properties of gasoline and DCM, including parameters such as density, lower heating value (LHV), viscosity, and other key characteristics essential for evaluating engine performance and emissions. These properties are crucial for analyzing overall fuel efficiency and effectiveness.

Noise and vibration data were processed and analyzed to evaluate the impact of each fuel blend under varying load conditions. The average noise levels (measured in dBA) and vibration levels (measured in m/s²) for each blend were calculated and compared to those of pure gasoline. Full-load conditions were particularly emphasized as they provided the most pronounced insights into each blend's performance in reducing or amplifying noise and vibration. Statistical analyses were conducted to identify significant differences among the fuel blends. Uncertainties and ranges for measurement devices are presented in Table 4.

Table 3. Physicochemical properties of the test fuels [33-35]

Properties	Gasoline	DCM
Chemical Formula	$C_{6\text{-}12}H_{14\text{-}26}$	CH_2Cl_2
Energy Content-LHV (MJ/kg)	43.594	13
Flash Point (°C)	-43	-
Boiling Point (°C)	27-225	40
Freezing Point (°C)	-52	-95
Density (kg/m3)	746	1330
Viscosity (mPa.s)	0.4-0.8	0.413
Autoignition Temperature (°C)	257	605

Table 4. Uncertainties and ranges for the measurement devices

Measurement	Instrument	Accuracy	Uncertainty (%)
Fuel Consumption	Precision Scale (0.1 g)	±0.1 g	±1%
Exhaust Emissions	Bilsa Emission	CO: ±0.1%,	±2%
Exhaust Emissions	Bilsa Emission	CO_2: ±0.1%,	±2%
Exhaust Emissions	Bilsa Emission	NO_x: ±5 ppm	±2%
Exhaust Emissions	Bilsa Emission	HC: ±2 ppm	±2%
Noise Levels	PCE 322A	±0.1 dBA	±1.5%
Vibration	UNI-T UT315A	±0.01 m/s²	±1%
Engine Load	Dynamometer	±0.01 Nm	±1%
Engine Speed	Tachometer	±10 rpm	±0.5%

3. Results and Discussions

Figure 2 illustrates the noise levels produced by the engine, measured in dBA, for four different fuels and four different engine loads, including the no-load condition. Under the no-load condition, the noise level was measured at 91.24 dBA during engine tests using pure gasoline, whereas it increased to 91.61 dBA when DCM was added to the gasoline. For fuels with HL1 and HL2 additives (25 ppm each) dissolved in DCM and blended with gasoline, the noise levels under no-load conditions were 92.62 dBA and 88.91 dBA, respectively. This represents a 1.51% increase in noise level for the DCM+25 ppm HL1 blended fuel compared to pure gasoline, while the DCM+25 ppm HL2 blended fuel resulted in a 2.55% decrease in noise level.

The noise level measured during the test with pure gasoline at 25% engine load was 92.05 dBA, rising to 98.24 dBA when the engine load increased to 100%. This indicates that pure gasoline generates significant noise, particularly under high-load conditions. Overall, all engine tests demonstrated an increase in noise levels as the engine load increased. This trend highlights a direct relationship between engine load and noise generation, with higher loads resulting in elevated noise levels across all fuel blends.

The DCM-blended fuel mixture resulted in a slight increase in noise levels compared to pure gasoline across all engine loads, including the no-load condition. At full load, the noise level was 5.8% higher than at 25% load. This can be attributed to the slightly lower boiling point of DCM compared to gasoline. Additionally, DCM's higher density relative to gasoline is believed to cause a greater mass of the mixture to enter the cylinder, participating more actively in combustion reactions and intensifying the noise level due to the increased reaction activity.

Engine tests with the DCM + 25 ppm HL1 blended fuel recorded the highest noise levels across all engine loads and the no-load condition compared to all other fuels tested. At 25% load, the noise level reached 93.5 dBA, while at 100% load, it peaked at 99.8 dBA—the highest value observed in all tests. The DCM + 25 ppm HL1 blend appears to significantly increase noise generation, particularly under high-load conditions, likely due to the more volatile nature of the fuel mixture. Conversely, engine tests with the DCM + 25 ppm HL2 blended fuel recorded the lowest noise levels at all engine loads and the no-load condition compared to all fuels tested. At 100% load, the noise level was 95.8 dBA, while at 25% load, it dropped to 88.9 dBA, the lowest value recorded in all tests.

The results indicate that the addition of DCM and DCM + 25 ppm HL1 to gasoline generally increases noise levels. While DCM caused a slight increase, the effect of DCM + 25 ppm HL1 was more pronounced, particularly at higher engine loads. At no load and 25% engine load, the differences in noise levels between the fuel blends were relatively minor, with all fuels producing comparable noise levels. However, as engine load increased, the differences in noise levels became more distinct, highlighting the critical role of fuel composition in noise generation under high-load conditions. The most notable finding from the noise level measurements is that the fuel blend containing DCM + 25 ppm HL2 additive produced significantly lower noise levels across all load conditions compared to pure gasoline. This suggests that the DCM + 25 ppm HL2 blend promotes more stable combustion and slows the reaction rate and activation process. The additive's impact on the calorific value and activation energy of the mixture likely alters the combustion reactions and oxidation rate of the fuel. Consequently, the DCM + 25 ppm HL2 additive is considered a promising option for applications where noise reduction is a critical requirement.

Figure 3 illustrates the variation in engine vibration values for four different fuels and four engine loads, as well as the no-load condition. During the no-load engine test with pure gasoline, the vibration value was measured at 33.4 m/s², which increased to 34.1 m/s² when DCM was added to the gasoline. For fuels with HL1 and HL2 additives (25 ppm each) dissolved in DCM and blended with gasoline, the no-load vibration values were measured at 42.6 m/s² for the DCM + 25 ppm HL1 fuel and 32.5 m/s² for the DCM + 25 ppm HL2 fuel. Compared to pure gasoline, the DCM + 25 ppm HL1 blend increased vibration by 27.54%, while the DCM + 25 ppm HL2 blend reduced vibration by 2.69%.

The vibration values produced by the DCM-blended fuel mixture are slightly higher compared to pure gasoline across all engine loads and in the no-load condition. At full load, the vibration level is 171.85% higher than at 25% load. This increase in vibration can be attributed to the high density, elevated auto-ignition temperature, and low energy content of DCM. The high auto-ignition temperature of DCM likely causes a delay in the combustion process, complicating the combustion conditions by adversely affecting the environment necessary for oxidation reactions within the combustion chamber. Additionally, DCM's higher density compared to gasoline may lead to a greater mass of the mixture being drawn into the cylinder. However, the high density may also reduce DCM's ability to form homogeneous mixtures with gasoline and air, potentially resulting in locally rich mixture zones within the combustion chamber. These localized zones may cause the gas temperature to rise unevenly in certain areas of the chamber, leading to sudden and rapid combustion, which contributes to increased vibration levels. Fuel additives influence the fuel mixture's chemical composition and alter the combustion process's thermodynamic conditions, further impacting engine performance and vibration characteristics.

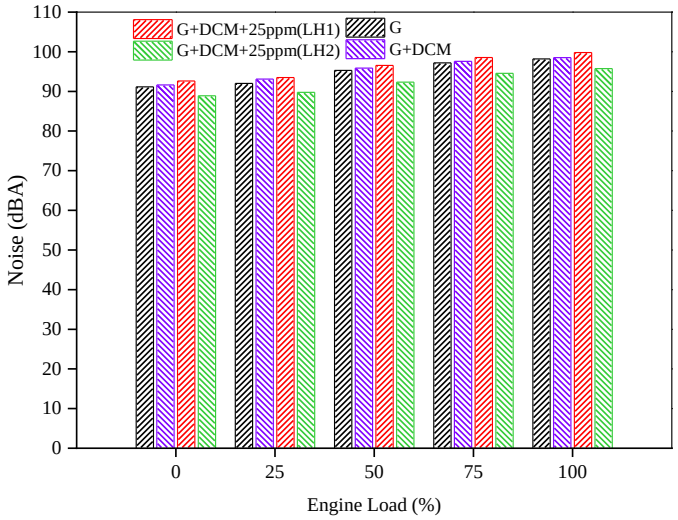

Figure 2. Variation of noise for various test fuels at different load conditions (25 ppm additive)

Engine tests using the DCM + 25 ppm HL1 blended fuel recorded the highest vibration values across all engine loads and in the no-load condition compared to all other fuels tested. At 25% load, the vibration level reached 47.2 m/s², increasing to 94.5 m/s² at 100% load, the highest value observed in all tests. The presence of the DCM + 25 ppm HL1 additive appears to affect the combustion process, leading to rapid combustion reactions. This suggests that the engine operates less stably with this blend than with pure gasoline. It is also anticipated that pressure fluctuations in the combustion chamber increase with this fuel additive during the combustion process, contributing to elevated vibration levels in the engine. In contrast, engine tests using the DCM + 25 ppm HL2 blended fuel measured the lowest vibration levels across all engine loads and in the no-load condition compared to all other fuels tested. At 100% load, the vibration level was 80.5 m/s², decreasing to 32.5 m/s² at 25% load, the lowest value recorded in all tests. The DCM + 25 ppm HL2 additive is believed to promote more uniform and stable combustion. As the flame front progresses more smoothly and combustion remains consistent, vibration levels are thought to be reduced.

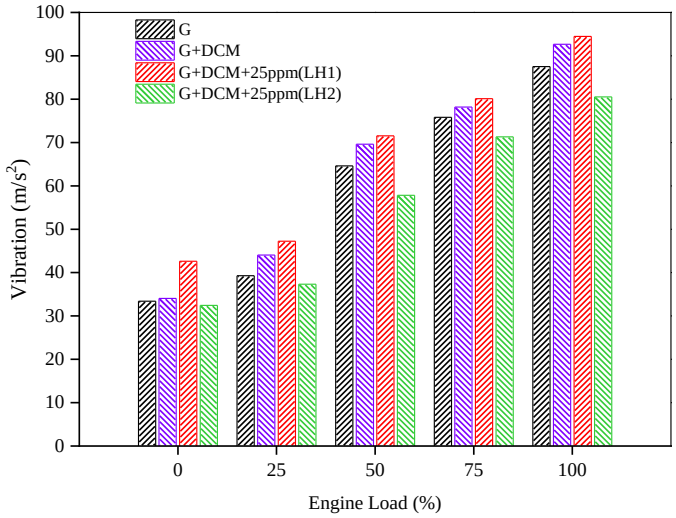

Figure 3. Variation of vibration for various test fuels at different load conditions (25 ppm additive)

The noise levels for different fuel blends and engine loads are summarized in Figure 4. Based on the experimental results, noise levels increased with engine load for all fuel blends, reflecting the higher combustion pressures and mechanical stresses at higher loads. At 0% engine load, the lowest noise level was observed with pure gasoline at 91.15 dBA. The closest result to gasoline was recorded with LH2, which showed a slight increase of 0.23%, producing a noise level of 91.36 dBA. The highest noise level at 0% load was observed with LH1, reaching 95.31 dBA, which represented a 4.56% increase compared to gasoline. At 25% engine load, the noise level for gasoline was measured at 92.01 dBA. The addition of LH1 resulted in the highest noise level at this load, reaching 96.26 dBA. On the other hand, LH2 produced a noise level of 93.09 dBA, which was closer to the value for gasoline. At 50% engine load, the lowest noise level was achieved with LH2, producing a value of 94.21 dBA, which represented a 1.15% reduction compared to gasoline. In contrast, the highest noise level at this load was recorded with LH1 at 97.98 dBA. At 75% engine load, LH1 again resulted in the highest noise level, measuring 99.48 dBA. In comparison, LH2 produced the lowest noise level at 96.75 dBA. At 100% engine load, LH2 provided the lowest noise level of 96.69 dBA, which was a 1.51% reduction compared to gasoline at 98.18 dBA. The highest noise level at full load was recorded with LH1 at 99.35 dBA. Adding DCM to gasoline generally increased noise levels compared to pure gasoline. This increase can be attributed to the effects of DCM on combustion characteristics, such as increased knocking tendencies and changes in flame propagation. Combining DCM with LH1 further amplified noise levels, producing the highest values across all engine loads. This may be due to the impact of LH1 on octane rating and combustion intensity. Conversely, adding LH2 reduced noise levels, particularly at 50% and above engine loads, where it consistently provided the lowest noise levels. This reduction can likely be attributed to LH2's superior knock resistance and stabilizing effects on combustion. LH2 demonstrated its effectiveness in maintaining or reducing noise levels compared to gasoline, particularly under high-load conditions. This makes LH2 a promising additive for quieter engine operation. On the other hand, LH1's tendency to increase noise levels may limit its suitability for applications requiring low-noise operation. In summary, noise levels increased with engine load for all fuel blends. Adding DCM and LH1 contributed to higher noise levels, with LH1 causing the largest increases. In contrast, LH2 consistently reduced noise levels, particularly for 50% and above engine loads. At 100% load, LH2 achieved a 1.51% reduction in noise compared to gasoline. These findings highlight LH2's potential to improve engine noise characteristics, particularly under higher load conditions, while LH1 may require further optimization to reduce its noise-increasing effects.

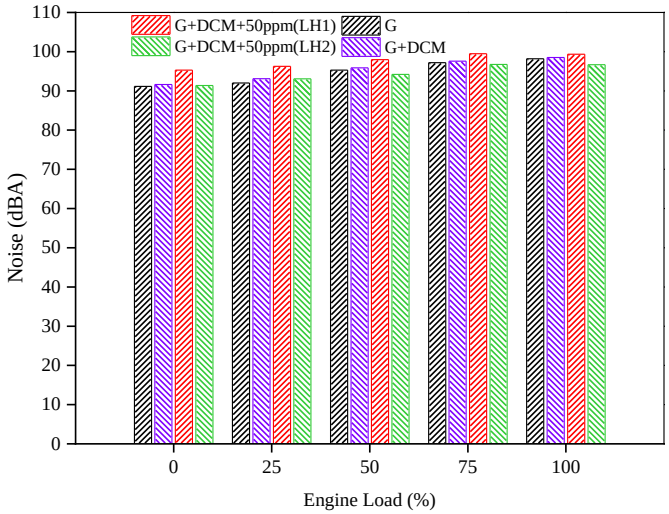

Figure 4. Variation of noise for various test fuels at different load conditions (50 ppm additive)

The vibration values of 50 ppm additives for different engine loads and fuel blends are presented in Figure 5. As engine load increased, vibration levels generally increased for all fuel blends. This trend aligns with the expected behavior due to the higher mechanical and combustion stresses at higher loads.

The lowest vibration level (33.4 m/s²) was observed at no-load conditions with gasoline. The closest result was obtained with a 50 ppm addition of LH2 (33.78 m/s²), showing only a 1.14% increase compared to gasoline. The highest vibration level (38.3 m/s²) was recorded with LH1, resulting in a 14.67% increase compared to gasoline. Gasoline again exhibited the lowest vibration (39.29 m/s²), while the highest vibration (53.95 m/s²) was recorded with LH1 at 25% engine load. LH1 caused a 37.32% increase compared to gasoline. At 50% load, The lowest vibration (48.68 m/s²) was observed with LH2, while the highest vibration (71.93 m/s²) was recorded with LH1. LH2 achieved a 24.64% improvement, whereas LH1 caused an 11.34% deterioration compared to gasoline. The lowest vibration level (83.63 m/s²) was achieved with LH2, while the highest vibration (94.25 m/s²) occurred with LH1 at full load. The addition of DCM led to a general increase in vibration levels compared to gasoline due to its density and viscosity, which may influence combustion dynamics and increase the risk of knocking. 50 ppm LH1 further amplified vibration levels, particularly at lower engine loads, likely due to its effects on octane rating and combustion characteristics. Conversely, LH2 demonstrated significant vibration reductions at 50% and above engine loads. This reduction is likely due

to LH2's high knock resistance and its stabilizing effect on combustion. The combination of DCM+50 ppm LH2 consistently resulted in reduced vibration levels at higher engine loads, making it a promising additive for mitigating engine vibrations in heavy-duty applications. The use of LH1, while beneficial for certain performance parameters, may require optimization to prevent excessive vibrations, particularly at lower engine loads. LH2 shows potential for improving engine stability and reducing vibrations, especially in scenarios requiring high-load operation. DCM alone increases vibration levels due to its physical properties affecting combustion. DCM+50 ppm LH1 exacerbates vibrations, particularly at low loads, due to its influence on octane and combustion dynamics. DCM+ 50 ppm LH2 demonstrates the ability to reduce vibrations at higher loads, likely due to its superior knock resistance.

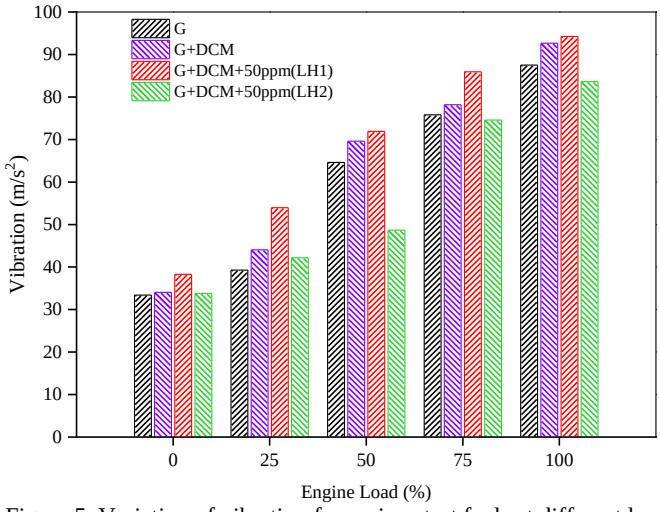

Figure 5. Variation of vibration for various test fuels at different load conditions (50 ppm additive)

The results for noise levels across different fuel blends and engine loads are shown in Figure 6. The measurements at loads ranging from 0% to 100% indicate noticeable variations among the fuel mixtures. Noise levels of G ranged from 91.15 dBA at 0% load to 98.18 dBA at 100% load. A gradual increase in noise levels is observed with the increasing engine load, consistent with expectations due to higher combustion pressures and mechanical stresses. Noise levels of G+DCM were slightly higher than the baseline, ranging from 91.64 dBA at 0% load to 98.52 dBA at 100% load. The inclusion of DCM resulted in a marginal increase in noise, likely due to its lower energy content and differing combustion characteristics compared to pure gasoline. Adding 100 ppm, LH1 led to noise levels slightly higher than G+DCM, ranging from 91.83 dBA at 0% load to 100.99 dBA at 100% load. The increase in noise could be attributed to the chemical properties of LH1, which may alter the combustion process and result in increased acoustic emissions. LH2 showed the highest noise levels among all mixtures, ranging from 92.03 dBA at 0% load to 99.19 dBA at 100% load. The higher noise levels may indicate that LH2 affects the combustion process differently than HL1, possibly leading to more intense pressure fluctuations within the engine cylinder. For all fuel blends, noise levels increased with engine load, reflecting the impact of higher thermal and mechanical loads on noise generation. The rate of noise increase appeared more pronounced for LH1 and LH2 blends compared to the baseline and DCM blends, suggesting that the additives amplify noise at higher loads. While DCM alone had a negligible effect on noise levels, the combination of DCM with LH1 and LH2 caused noticeable increases in noise, particularly under full-load conditions. LH2 consistently produced higher noise levels than HL1 at all load conditions, suggesting that its combustion characteristics may differ significantly. Overall, while the 100 ppm addition of LH1 and LH2 resulted in increased noise levels, particularly at higher engine loads, these changes need to be weighed against potential fuel efficiency and emissions benefits.

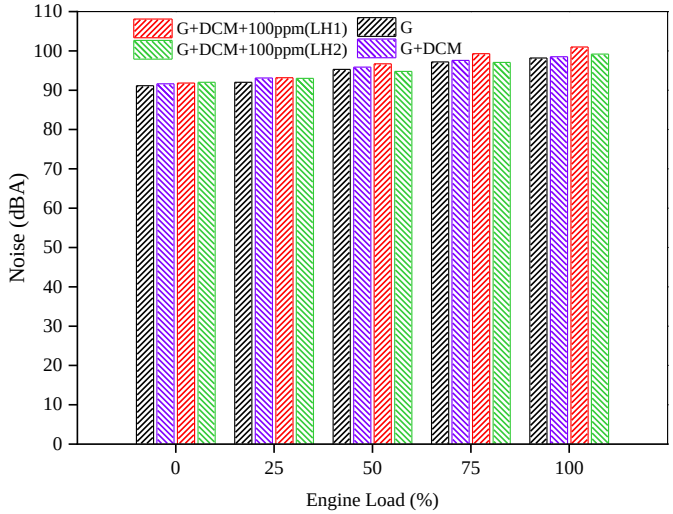

Figure 6. Variation of noise for various test fuels at different load conditions (100 ppm additive)

The vibration levels for the different fuel mixtures and engine loads are shown in Figure 7. Measurements, expressed in terms of acceleration (m/s²), were recorded at loads ranging from 0% to 100%. Vibration levels increased from 33.40 m/s² at 0% load to 87.50 m/s² at 100% load for Gasoline. The steady increase in vibration with engine load reflects typical engine behavior, where higher loads induce greater mechanical forces and dynamic imbalances. Vibration levels for G+DCM were slightly higher than the baseline, ranging from 34.05 m/s² at 0% load to 92.67 m/s² at 100% load. The addition of DCM marginally altered the engine's combustion characteristics, leading to slightly higher vibrations across all load conditions. The addition of LH1 at 100 ppm resulted in higher vibration levels at lower loads (e.g., 41.2 m/s² at 0%) but comparable levels to G+DCM at full load (87.4 m/s² at 100% load). The sharp increase in vibration at lower loads suggests that LH1 affects combustion stability, potentially introducing uneven forces during operation. LH2 showed distinct behavior, with vibration levels ranging from 39.53 m/s² at 0% load to 85.51 m/s² at 100% load. Notably, LH2 exhibited lower vibration levels than both G and G+DCM at higher loads (e.g., 85.51 m/s² vs. 87.5 m/s² for G at 100% load), indicating a stabilizing effect under high-load conditions. Across all fuel blends, vibration levels increased with engine load due to greater mechanical stresses and dynamic forces. While the additives caused variations in vibration levels, the overall trends were consistent across all blends. LH1 resulted in the highest increase in vibration at lower loads, possibly due to its impact on combustion dynamics. LH2 demonstrated a stabilizing effect at higher loads, reducing vibrations compared to the baseline fuel. DCM increased vibration levels slightly compared to

pure gasoline, likely due to its lower energy content and its effect on combustion efficiency. Vibration levels across all fuels showed a predictable increase with load, emphasizing the influence of mechanical stresses and combustion pressure fluctuations. The increased vibration levels at lower loads with LH1 suggest potential issues with combustion stability, which may require further optimization of additive concentration. The lower vibration levels at higher loads with LH2 highlight its potential as a stabilizing agent for engines operating under heavy-duty conditions. Higher vibrations can impact engine durability and user comfort, so balancing additive benefits with potential drawbacks is crucial.

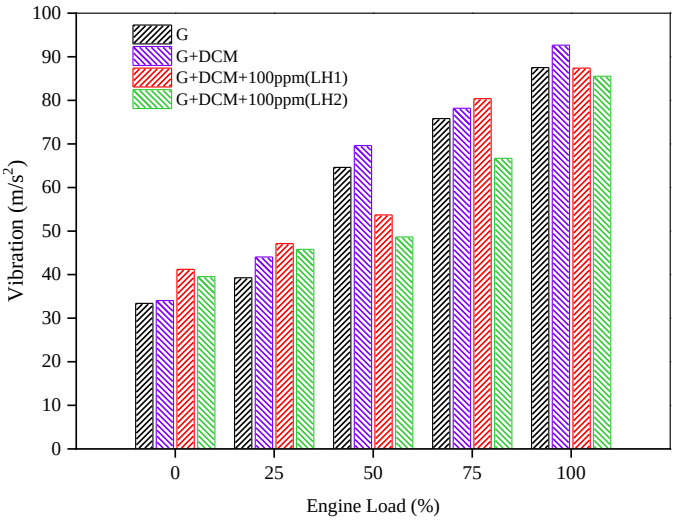

Figure 7. Variation of vibration for various test fuels at different load conditions (100 ppm additive)

4. Conclusions

The experimental results provide a detailed analysis of the effects of DCM and benzoylthiourea derivatives (LH1 and LH2) at concentrations of 25 ppm, 50 ppm, and 100 ppm on engine noise levels. Based on the data provided, key conclusions, including percentage improvements and deteriorations compared to pure gasoline, are as follows:

- Adding DCM to gasoline caused slight increases in noise levels across all engine loads. At no load, the noise increased by 0.53% compared to gasoline, while at 100% load, it increased by 0.34%. These increases are likely due to DCM's lower energy content and higher density, leading to altered combustion dynamics.
- Adding DCM+LH1 25 ppm, Noise levels increased by 1.62% at no load and 1.65% at 100% load compared to gasoline. In addition to DCM+LH1 50 ppm, Noise levels rose by 4.55% at no load and 1.19% at 100% load compared to gasoline. In addition to DCM+LH1, 100 ppm LH1 caused the most significant increases in noise levels. Noise levels increased by 6.77% at no load and 2.87% at 100% load compared to gasoline. The results indicate that LH1 consistently increases noise levels, intensifying the effects at higher concentrations. The volatile nature of LH1 and its impact on combustion dynamics likely contribute to these increases.
- Adding DCM+LH2 25 ppm noise levels decreased by 2.77% at no-load and 2.47% at 100% load compared to gasoline. At DCM + LH2 50 ppm, LH2 continued to reduce noise but with slightly less impact. Noise levels decreased by 0.21% at no-load and 1.51% at 100% load compared to gasoline. At 100 ppm, HL2 provided the best performance: Noise levels decreased by 0.78% at no load and 1.98% at 100% load compared to gasoline. These results highlight that HL2 is an effective additive for reducing noise levels, particularly at 25 ppm and 100 ppm concentrations. Its high knock resistance and ability to stabilize combustion contribute to its noise-reducing effects.
- DCM alone causes slight increases in noise levels and has minimal effect compared to LH1 additives. LH1 consistently increases noise levels, making it less desirable for noise-sensitive applications. Its effects worsen at higher concentrations, suggesting a need for optimization. LH2, particularly at 25 ppm and 50 ppm, significantly reduces noise levels compared to gasoline at high loads, making it the most promising additive for reducing engine noise.

The impact of benzoylthiourea additives on engine noise and vibration remains under investigation. Analyzing the effects of these additives on gasoline and diesel engines, particularly at varying concentrations, could provide valuable contributions to the existing body of literature.

Acknowledgment

The authors would like to thank the Department of Chemistry at Mehmet Akif Ersoy University for its contributions.

Nomenclature

IC	Internal Combustion
SI	Spark Ignition
DCM	Dichloromethane
dBA	Decibel
LHV	Lower Heating Value
BSFC	Brake Specific Fuel Consumption

Conflict of Interest Statement

The authors declare that there is no conflict of interest in the study.

CRediT Author Statement

Sertaç Coşman: Conceptualization, Supervision, Writing-original draft, Software **Samet Çelebi:** Conceptualization, Supervision, Writing-original draft, Writing - review & editing, Methodology

References

1. Reitz, R., & Duraisamy, G. (2015). Review of high efficiency and clean reactivity controlled compression ignition (RCCI) combustion in internal combustion engines. Progress in Energy and Combustion Science, 46, 12-71. https://doi.org/10.1016/j.pecs.2014.05.003
2. Dahham, R., Wei, H., & Pan, J. (2022). Improving Thermal Efficiency of Internal Combustion Engines: Recent Progress and Remaining Challenges. Energies. https://doi.org/10.3390/en15176222
3. Yue, Z., & Liu, H. (2023). Advanced research on internal combustion engines and engine fuels. Energies, 16(16), 5940. https://doi.org/10.3390/en16165940

4. Leach, F., Kalghatgi, G., Stone, R., & Miles, P. (2020). The scope for improving the efficiency and environmental impact of internal combustion engines. Transportation Engineering, 1, 100005. https://doi.org/10.1016/j.treng.2020.100005
5. Ardebili, S. M. S., Solmaz, H., & Mostafaei, M. (2019). Optimization of fusel oil–Gasoline blend ratio to enhance the performance and reduce emissions. Applied Thermal Engineering, 148, 1334-1345. https://doi.org/10.1016/j.applthermaleng.2018.12.005
6. Velmurgan, V., Kumar, J. R., & Thanikaikarsan, S. (2020). A survey NVH analysis of three cylinder passenger vehicle. Materials Today: Proceedings, 33, 3532-3536. https://doi.org/10.1016/j.matpr.2020.05.442
7. Kumar, P. (2023). Methods to Reduce the Noise and Vibration of Engine. International Journal for Research in Applied Science and Engineering Technology, 11(4). https://doi.org/10.22214/ijraset.2023.50067
8. Tüccar, G. (2018). Experimental study on vibration and noise characteristics of a diesel engine fueled with mustard oil biodiesel and hydrogen gas mixtures. Biofuels, 12, 537 - 542. https://doi.org/10.1080/17597269.2018.1506631
9. Elkelawy, M., Bastawissi, H. A. E., El Shenawy, E. A., & Soliman, M. Effect of Organic Compounds Additives for Biodiesel Fuel blends on Diesel Engine Vibrations and Noise Characteristics, 8(1), https://digitalcommons.aaru.edu.jo/erjeng/vol8/iss1/26
10. K Bharath, B., & V, A. M. S. (2024). Effect of ternary blends on the noise, vibration, and emission characteristics of an automotive spark ignition engine. Energy Sources, Part A: Recovery, Utilization, and Environmental Effects, 46(1), 11073-11094. https://doi.org/10.1080/15567036.2020.1788673
11. Wirawan, T. S., Putra, A. E. E., & Aziz, N. (2021, December). Gasoline engine performance, emissions, vibration and noise with methanol-gasoline fuel blends. In IOP Conference Series: Earth and Environmental Science (Vol. 927, No. 1, p. 012027). IOP Publishing. https://doi.org/10.1088/1755-1315/927/1/012027
12. Ağbulut, Ü., Karagöz, M., Sarıdemir, S., & Öztürk, A. (2020). Impact of various metal-oxide based nanoparticles and biodiesel blends on the combustion, performance, emission, vibration and noise characteristics of a CI engine. Fuel, 270, 117521. https://doi.org/10.1016/j.fuel.2020.117521
13. Xu, Y., Rao, X., Guo, Z., Liu, Z., Yin, H., Hu, H., & Yuan, C. (2024). Effects of fuel composite additives on the vibration, wear and emission performances of diesel engines under hot engine tests. Engineering Failure Analysis, 160, 108156. https://doi.org/10.1016/j.engfailanal.2024.108156
14. Wei, J., He, C., Fan, C., Pan, S., Wei, M., & Wang, C. (2021). Comparison in the effects of alumina, ceria and silica nanoparticle additives on the combustion and emission characteristics of a modern methanol-diesel dual-fuel CI engine. Energy Conversion and Management, 238, 114121. https://doi.org/10.1016/j.enconman.2021.114121
15. Rao, K., Rao, B., & Babu, V. (2015). Heat release rate and engine vibration correlation to investigate combustion propensity of an IDI engine run with biodiesel (MME) and methanol additive as an alternative to diesel fuel. Biofuels, 6, 45 - 54. https://doi.org/10.1080/17597269.2015.1045275
16. Sani, M. S. M., Mamat, R., & Gani, A. (2022). Effect of vibration and noise on spark ignition engines of methanol fuel blended with gasoline. Journal of Scientific and Industrial Research, 81(01), 32-38. http://nopr.niscpr.res.in/handle/123456789/58875
17. Sharma, N., Patel, C., Tiwari, N., & Agarwal, A. K. (2019). Experimental investigations of noise and vibration characteristics of gasoline-methanol blend fuelled gasoline direct injection engine and their relationship with combustion characteristics. Applied Thermal Engineering, 158, 113754. https://doi.org/10.1016/j.applthermaleng.2019.113754
18. Borg, J., Watanabe, A., & Tokuo, K. (2012). Mitigation of noise and vibration in the high-pressure fuel system of a gasoline direct injection engine. Procedia-Social and Behavioral Sciences, 48, 3170-3178. https://doi.org/10.1016/j.sbspro.2012.06.1283
19. Keskin, A. (2010). The influence of ethanol–gasoline blends on spark ignition engine vibration characteristics and noise emissions. Energy sources, part a: recovery, utilization, and environmental effects, 32(20), 1851-1860. https://doi.org/10.1080/15567030902804749
20. Faraji, H., Heidarbeigi, K., & Samadi, S. (2021). Characterization of vibration and noise pollution of SI engine fueled with magnetized ethanol–gasoline blends by time–frequency methods. Noise & Vibration Worldwide, 52(11),356-364. https://doi.org/10.1177/09574565211030704
21. Uyumaz, A., Kilmen, A. B., & Kaş, M. (2024). An experimental study of the influences of lacquer thinner addition to gasoline on performance and emissions of a spark ignition engine. Engineering Perspective, 4(2), 54-59. http://dx.doi.org/10.29228/eng.pers.75965
22. Aydoğan, B. (2021). Combustion, performance and emissions of ethanol/n-heptane blends in HCCI engine. Engineering Perspective, 1(1), 5.
23. Schroeder, D. C. Thioureas. Chemical Reviews, 55(1), 181-228, New Jersey, 1954. https://doi.org/10.1021/cr50001a005
24. Mukiza, J., Braband, H., Bolliger, R., Blacque, O., Alberto, R. and Nkurunziza, J. B. (2021). A novel benzoylthiourea derivative with a triazinethione moiety: Synthesis and coordination with the organometallic fac-[Re (CO) 3]+ core. Inorganica Chimica Acta, 516, 120116. https://doi.org/10.1016/j.ica.2020.120116
25. Saeed, A., Flörke, U. and Erben, M. F. (2014). A review on the chemistry, coordination, structure and biological properties of 1-(acyl/aroyl)-3-(substituted) thioureas. Journal of Sulfur Chemistry, 35(3), 318-355. https://doi.org/10.1080/17415993.2013.834904
26. Plutín, A. M. et al. (2016). Anti-Mycobacterium tuberculosis activity of platinum (II)/N, N-disubstituted-N′-acyl thiourea complexes. Inorganic Chemistry Communications, 63, 74-80. https://doi.org/10.1016/j.inoche.2015.11.020
27. Yang, W., Liu, H., Li, M., Wang, F., Zhou, W. and Fan, J. (2012). Synthesis, structures and antibacterial activities of benzoylthiourea derivatives and their complexes with cobalt. Journal of inorganic biochemistry, 116, 97-105. https://doi.org/10.1016/j.jinorgbio.2012.08.001
28. Keskin, A., Ocakoglu, K., Resitoglu, I. A., Avsar, G., Emen, F. M. and Buldum, B. (2015). Using Pd (II) and Ni (II) complexes with N, N-dimethyl-N′-2-chlorobenzoylthiourea ligand as fuel additives in diesel engine. Fuel, 162, 202-206. https://doi.org/10.1016/j.jinorgbio.2012.08.001
29. Keskin, A., Yaşar, A., Yıldızhan, Ş., Uludamar, E., Emen, F. M. and Külcü, N. (2018). Evaluation of diesel fuel-biodiesel blends with palladium and acetylferrocene-based additives in a diesel engine. *Fuel*, 216, 349-355. https://doi.org/10.1016/j.fuel.2017.11.154

30. Gao, L., Geng, C., Teng, B., Xiang, H., Wen, X., Yang, Y. and Li, Y. (2024). Improvement of octane number in FCC gasoline through the extraction with urea/thiourea complex based on property analysis. Industrial Chemistry & Materials, 2, 613-621. https://doi.org/10.1039/D4IM00005F
31. Yeşilkaynak, T., Özpınar, C., Emen, F. M., Ateş, B., & Kaya, K. (2017). N-((5-chloropyridin-2-yl) carbamothioyl) furan-2-carboxamide and its Co (II), Ni (II) and Cu (II) complexes: Synthesis, characterization, DFT computations, thermal decomposition, antioxidant and antitumor activity. Journal of Molecular Structure, 1129, 263-270. https://doi.org/10.1016/j.molstruc.2016.09.083
32. Yeşilkaynak, T., Muslu, H., Özpınar, C., Emen, F. M., Demirdöğen, R. E. and Külcü, N. (2017). Novel thiourea derivative and its complexes: synthesis, characterization, DFT computations, thermal and electrochemical behavior, antioxidant and antitumor activities. Journal of Molecular Structure, 1142, 185-193. https://doi.org/10.1016/j.molstruc.2017.04.049
33. Yang, N. (2014). Dichloromethane. Encyclopedia of Toxicology (Third Edition), Manchester University, Fort Wayne, IN, USA. https://doi.org/10.1016/B978-0-12-386454-3.01218-5
34. Gültekin, E., Calam, A., & Şahin, M. (2023). Experimental investigation of trimethyl borate as a fuel additive for a SI engine. Energy sources, part a: recovery, utilization, and environmental effects, 45(1), 419-433. https://doi.org/10.1080/15567036.2023.2171516
35. Özer, S. (2021). Effects of alternative fuel use in a vehicle with TSI (turbocharged direct-injection spark-ignition) engine technology. International Journal of Green Energy, 18(12), 1309-1319. https://doi.org/10.1080/15435075.2021.1904406

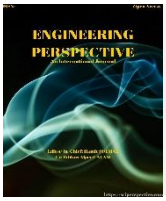

e-ISSN:2757-9077

ENGINEERING PERSPECTIVE

https://sciperspective.com/ Research Paper

Adaptive PID Controller Design for Velocity Control of a Hydrogen Internal Combustion Engines using RBF Neural Networks

Quang Truc Dam[1,*], Fatima Haidar[1]

[1] *Capgemini Engineering, Research & Innovation Direction, 12 rue de la Verrerie, 92190, Meudon, France*

ABSTRACT

Achieving precise velocity control in ICEs is crucial for optimizing performance, fuel efficiency, and reducing emissions. However, the nonlinear dynamics and uncertainties inherent in ICE systems pose significant challenges for conventional control methods. In this paper, we propose an adaptive approach integrating a Proportional-Integral-Derivative (PID) controller with Radial Basis Function Neural Networks (RBFNN) to address these challenges effectively. The proposed controller architecture comprises two main components: a RBFNN designed to estimate modeling uncertainties, such as unknown friction and external disturbances impacting the ICE structure, and a primary PID controller responsible for regulating velocity. The RBFNN serves as a dynamic estimator, continuously learning and adapting to variations in system dynamics, thereby enhancing the controller's robustness and adaptability. By accurately capturing the nonlinearities and uncertainties inherent in ICEs, the RBFNN contributes to improved control performance and stability. To validate the efficacy of the proposed approach, extensive numerical simulations are conducted using MATLAB Simulink. The simulations involve various operating conditions and scenarios to comprehensively evaluate the controller's performance. Additionally, the proposed methodology is compared against conventional PID methods documented in the literature to assess its superiority in terms of robustness, tracking accuracy, and disturbance rejection. The results demonstrate that the adaptive PID controller utilizing RBFNNs outperforms traditional PID approaches, exhibiting superior velocity regulation and disturbance rejection capabilities. Moreover, the proposed methodology showcases promising potential for real-world implementation in ICE-based systems, offering enhanced control performance and efficiency. Overall, this study contributes to advancing the field of control engineering by introducing a novel adaptive control strategy tailored specifically for velocity control in internal combustion engines, leveraging the capabilities of RBFNNs to mitigate uncertainties and improve overall system performance.

Keywords: Internal Combustion Engine (ICE); MATLAB-Simulink; Proportional-Integral-Derivative (PID); Radial Basis Function Neural Networks (RBFNN), Hydrogen.

History
Received: 19.04.2024
Accepted: 13.01.2025

How to cite this paper: Dam, Q.T., Haidar, F., (2025). Adaptive PID Controller Design for Velocity Control of a Hydrogen Internal Combustion Engines using RBF Neural Networks. Engineering Perspective, 5 (1), 41-48. http://dx.doi.org/10.29228/eng.pers.76280

Author Contacts
**Corresponding Author*
e-mail addresses :Quang-truc.dam@capgemini.com , Fatima.haidar@capgemini.com ,

1. Introduction

The internal combustion engine (ICE) stands as a pinnacle of modern engineering, revolutionizing transportation, and power generation since its inception [1-3]. It represents a marvel of human innovation, converting the chemical energy stored in fossil fuels into mechanical energy through controlled combustion within a confined space. Among the various types of internal combustion engines, the four-stroke internal combustion engine emerges as a cornerstone in automotive and industrial applications, owing to its efficiency, reliability, and versatility.

Four-stroke internal combustion engines operate on a systematic cycle of intake, compression, power, and exhaust strokes, each meticulously orchestrated to harness energy from fuel and propel machinery forward. This cyclic process not only ensures optimal power output but also minimizes waste and environmental impact compared to alternative engine designs.

Four-stroke internal combustion engines are predominant choices in the field of conventional and hybrid vehicles due to their superior energy efficiency compared to two-stroke engines [1-3]. This preference stems from multiple factors, including the fact that a four-

stroke engine generates power only once every two revolutions, resulting in lower fuel consumption compared to two-stroke engines, which require one revolution for a complete power stroke. This fundamental difference in how four-stroke and two-stroke engines generate power has significant implications in terms of fuel economy and emission reduction.

Four-stroke engines also offer the additional advantage of producing fewer emissions and providing a more constant torque than their two-stroke counterparts. This is attributable to the more complex design of four-stroke engines, which allows them to optimize the combustion process and minimize energy losses.

Regarding spark ignition (SI) engines, they primarily operate on gasoline, although they can also use ethanol as an alternative fuel, making them more energy versatile. The main components of SI engines include the intake and exhaust manifold, intake and exhaust valves, spark plug, piston, coolant, cylinder, crankcase, connecting rod, and crankshaft. Each component plays a crucial role in the overall operation of the engine, contributing to its performance and efficiency.

In this study, we extend the scope of conventional internal combustion engine technology by adapting it for hydrogen fuel utilization. Hydrogen, as a clean and sustainable energy carrier, offers a compelling alternative to fossil fuels, enabling combustion with zero carbon emissions. Unlike traditional hydrocarbon-based fuels, hydrogen combustion primarily produces water vapor, significantly reducing greenhouse gas emissions and contributing to environmental sustainability. The adaptation of internal combustion engines to hydrogen fuel presents unique challenges, including optimizing fuel injection strategies, mitigating pre-ignition risks, and ensuring efficient combustion dynamics. By leveraging advanced control methodologies, we aim to develop an adaptive speed control system tailored for hydrogen-powered ICEs, enhancing their performance, stability, and efficiency. This transition toward hydrogen-based internal combustion engines aligns with global efforts to decarbonize transportation and industrial applications while preserving the advantages of well-established ICE technology.

Motivated by its widely used in many applications, the study of controlling this motor. The design of speed controller for internal combustion engines (ICE) has garnered much attention in the automation community due to its crucial role in improving engine performance and efficiency. In recent studies [4-5], researchers have focused on implementing PID controllers specifically tailored to control the speed of ICEs. These controllers offer a robust and versatile solution to maintain desired speeds under various operating conditions, thereby contributing to enhancing engine operation and energy efficiency.

In another notable initiative [6], a sophisticated control system designed for engine speed and torque, using a linear quadratic regulator (LQR) approach, was introduced. This system employs first-order transfer functions with delay, demonstrating successful implementation and validation across the operational spectrum of both diesel and spark ignition engine dynamometer sets [7]. The use of LQR methodology underscores the importance of advanced control techniques in optimizing engine performance and ensuring smooth operation under diverse load conditions.

Furthermore, the application of Model Predictive Control (MPC) has proven to be a promising avenue for enhancing the accuracy and adaptability of speed control systems for ICE [8-10]. In [11] an adaptive sliding mode controller is proposed for controlling the air-fuel ratio of an ICE. Moreover, in a recent breakthrough [12], deep learning methodologies were integrated into the MPC controller design process, demonstrating the potential of innovative techniques in optimizing engine performance and efficiency. Additionally, the exploration of Secure Deep Reinforcement Learning (SDRL) in [13] highlights ongoing efforts to develop robust and reliable control strategies capable of ensuring both optimal performance and operational safety of ICE operations. These diverse approaches collectively contribute to advancing the state of the art in speed control systems for internal combustion engines, offering insights and innovative solutions to optimize engine performance and enhance overall operational efficiency.

Motivated by these works, in this paper, one shall propose another approach using the advantage of radial basic functional neural network for design an adaptive PID controller for speed control of an ICE.

2. Dynamic model of an H_2-ICE

The key components of internal combustion engines can be analyzed to enhance understanding of their operation and interrelation. This deepens the knowledge base of engineers and researchers, paving the way for technological advancements and improvements in engine design and energy efficiency. To simplify the control design process, the dynamic model of an internal combustion engine (ICE) can be divided into two sub-dynamic models. First, the combustion dynamics, which include all the equations describing processes from air and fuel intake via the environment and fuel injectors to the combustion process. This process generates engine torque, which drives the crankshaft. Second, the crankshaft dynamic model, where the engine torque serves as an input for rotating the crankshaft. This rotation represents the motion of the ICE, with engine speed corresponding to the rotation speed of the crankshaft.

2.1. Combustion Dynamic Model

The combustion model starts by taking the air from the environment to send to the chamber, this controls the amount of air flowing into the engine in response to the driver's accelerator pedal action.

The mass flow rate ($\dot{m}_{air}$) is determined as following Eq. (1) [14]:

$$\dot{m}_{air} = \frac{A_{eff} P_{upstr}}{\sqrt{R T_{upstr}}} \Psi(P_{ratio}) \quad (1)$$

Where P_{ratio} is the ratio of downstream pressure (P_{dowstr}) and upstream pressure (P_{upstr}).

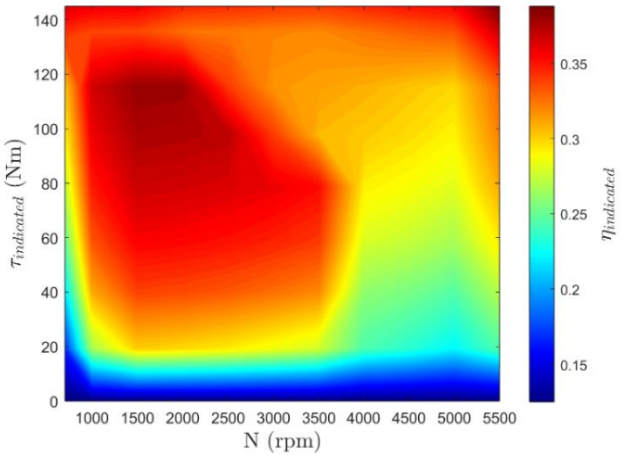

Figure 1. Charging Efficiency Coefficient [20].

$$\Psi(P_{ratio}) = \begin{cases} \sqrt{\gamma\left(\frac{2}{\gamma+1}\right)^{\frac{\gamma+1}{\gamma-1}}} & if:\ P_{ratio} < \left(\frac{2}{\gamma+1}\right)^{\frac{\gamma}{\gamma-1}} \\ \sqrt{\frac{2\gamma}{\gamma-1}\left(P_{ratio}^{\frac{2}{\gamma}} - P_{ratio}^{\frac{\gamma+1}{\gamma}}\right)} & if: \left(\frac{2}{\gamma+1}\right)^{\frac{\gamma}{\gamma-1}} < P_{ratio} < P_{lim} \\ \frac{P_{ratio}-1}{P_{lim}-1}\sqrt{\frac{2\gamma}{\gamma-1}\left(P_{lim}^{\frac{2}{\gamma}} - P_{lim}^{\frac{\gamma+1}{\gamma}}\right)} & if: P_{lim} < P_{ratio} \end{cases} \quad (2)$$

Where $P_{upstr} = P_{abt} = 101325$ Pa is the ambient pressure. $\Psi(P_{ratio})$ is the based follow correlation and is the function of P_{ratio} calculates the based on the different conditions of flow.

$$P_{ratio} = \frac{P_{dowstr}}{P_{upstr}} \quad (3)$$

Where P_{lim} is the pressure ratio limitation, $\gamma = 1.4$ is the ratio of specific heats

A_{eff} is the effect area, and is calculated as follows:

$$A_{eff} = \frac{\pi}{4} {D_{thr}}^2 C_{thr}(\theta_{thr}) \quad (4)$$

$$\theta_{thr} = \Theta_{ct\_thr}\frac{90}{100} \quad (5)$$

Where θ_{thr} is the open angle of the throttle valve(in degree), Θ_{ct_thr} is the percentage of throttle body that open, D_{thr} is the throttle diameter at opening, $C_{thr}(\theta_{thr})$is the discharge coefficient. To calculate the fuel flow in the hydrogen (H_2) internal combustion engine, one utilizes the characteristics of the fuel injector along with the fuel injector pulse-width. The model for fuel flow is expressed as:

$$\dot{m}_{fuel} = \frac{NS_{inj}P_{winj}N_{cyl}}{c_{ps}1000 * 60} \quad (6)$$

Where N represents engine speed in rpm, S_{inj} denotes the fuel injector slope, N_{cyl} signifies the number of engine cylinders, c_{ps} stands for the crankshaft revolutions per power stroke.

In the SI engine the indicated torque means that the torque or power of the engine is evaluated in the scope of thermodynamics (pressure and volume of cylinder), not including any mechanical losses in the whole power development and transmission process conceptually illustrates pressure variation in a cylinder along with crankshaft rotation angle. This torque is calculated as follows [11]:

$$\tau_{indicated} = \frac{P_{indicated} * 60}{2\pi N} \quad (7)$$

Where $P_{indicated}$ is the indicated power and can be calculated as:

$$P_{indicated} = \dot{m}_{fuel} * LHV\eta_{indicated} \quad (8)$$

Where $\eta_{indicated}$ is the engine indicated load efficiency as well as a function of engine speed (N) and indicated torque ($\tau_{indicated}$) as depicted in Figure 1

2.2. Crankshaft Model

The Crankshaft model demonstrates the indicated torque generated by the combustion reaction inside the chamber acts on the crankshaft, which then case the movement of crankshaft, hence generate the rotation movement of ICE. This relation is described as in the following equation:

$$\dot{\omega}(t) = -J^{-1}S(\omega)J\omega + J^{-1}(\tau_{control} + \tau_{uncertainties}) \quad (9)$$

Where ω is the rotation rate of the ICE, J is the crankshaft's moment of initial, $\tau_{control}$ is the indicated torque, $\tau_{uncertainties}$ is the unknown factor such as friction, engine load.

Because the crankshaft rotate in single axe, then we have $-J^{-1}S(\omega)J\omega = 0$, now set $\Gamma = J^{-1}\tau_{uncertainties}$, then we have the new dynamic equation of ICE is as:

$$\dot{\omega}(t) = J^{-1}\tau_{control} + \Gamma \quad (10)$$

3. Controller Design

In the previous section, we have developed the model of ICE H2 as well as its mathematical model. In this section, we shall focus on develop a controller for controlling the velocity of the ICE using Fuel injector pulse-width and Throttle valve's angle as control input.

Unlike the direct control scheme, using injector pulse-width and Throttle valve's angle as control input require a cascade control structure to control the velocity of ICE.

The controller structure is given in Figure. 2. The controller consist of two controllers, namely Inner loop controller and outer loop controller. The outer loop controller will be in charge of calculating the needed torque for controlling the velocity of ICE, this value then will be considered as desired value for the inner loop controller. The inner controller then uses the calculated torque valued given by the outer controller to calculate the needed injector pulse-width ($average\ value$) and Throttle valve's angle for obtaining the desired torque. It is worth noting that, using the cascade structure requires the inner controller loop responses faster than the outer control loop.

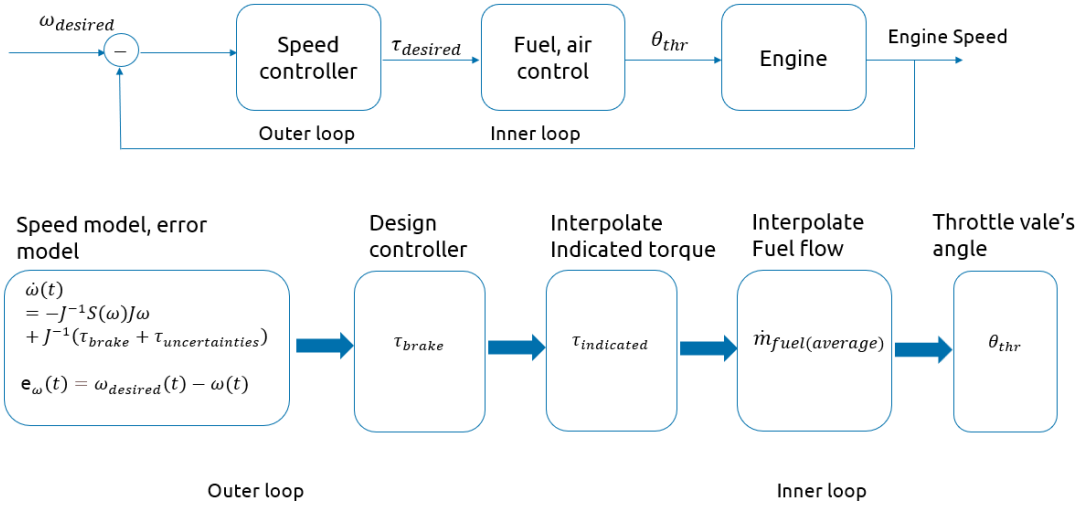

Figure 2. Control structure of ICE velocity controller.

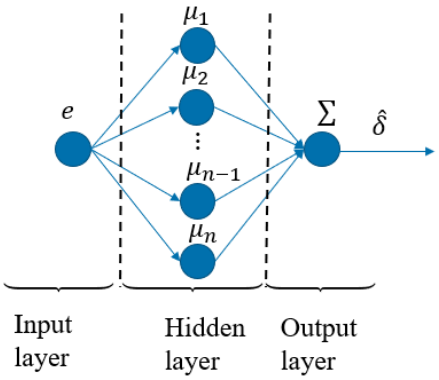

Figure 3. RBF neural network structure.

3.1. Outer loop controller

The objective of the outer controller to calculate the request torque based on the desired rotation velocity of the crankshaft.

Now let us define the controller tracking error as following:

$$e = \omega_{desired} - \omega \tag{11}$$

From (10,11) one gets:

$$J\dot{e} = -\tau_{control} - J\Gamma + J\dot{\omega}_{desired} \tag{12}$$

Let's define now $\delta = -J\Gamma + J\dot{\omega}_{desired}$ then (12) can be rewritten as follow:

$$J\dot{e} = -\tau_{control} + \delta \tag{13}$$

Remark 1: Taking into account that the function δ is unknown, the control input $\tau_{control}$ cannot be derived directly from (13). To overcome this drawback, an artificial neural network using RBFNN will be employed to estimate the unknown function δ.

For this sake, we propose to use the RBF neural network for estimating the value of δ ($\hat{\delta}$), The model of this neural network is given in Figure 4.

The RBFNN structure consists of three layers, namely the input, the output, and the hidden layer.

- Input Layer: The input to the network is the error signal, denoted as e. This signal is propagated to the hidden layer.
- Hidden Layer: The hidden layer contains n radial basis neurons, each corresponding to a radial basis function (RBF). These neurons compute the response to the input using a Gaussian activation function, which is defined as:

$$\mu_i(e) = exp\left(-\frac{\|e - r_i\|}{\eta_i}\right) \tag{14}$$

where r_i is the center of the radial basis function for neuron i, and η_i is the width of the Gaussian function. The output of the hidden layer can be represented as:

$$\mu(e) = [\mu_1(e) \quad \cdots \quad \mu_n(e)]^T \tag{15}$$

- Output Layer: The output layer produces the final output δ, which is a weighted sum of the hidden layer activations, plus an approximation error term e_{rbf}. Mathematically, this is expressed as:

$$\delta = W\mu(e) + e_{rbf} \tag{16}$$

Where W is the ideal weigh matrix and e_{rbf} is the approximation error. Based on the neural network theory, since the number of nodes is chosen suitable, this approximation error will be bounded. However, the ideal weigh matric (W) is unknown, therefore, for calculating the estimation of Γ one needs to estimate the value of W, this estimation is given as $\widehat{W}$, Hence the estimation of δ is given as:

$$\hat{\delta} = \widehat{W}\mu(e) \tag{17}$$

Based on this estimation, we propose the Robust controller using the Lyapunov theorem as follows:

$$\tau_{control} = K_1 e + K_2 \int e dt + K_3 sign(e) + \hat{\delta} \quad (18)$$

Assumption 1: The function δ is smooth and bounded.

Assumption 2: The neural network estimation error e_{rbf} is assumed to be small, unknown, and bounded by the following bounds:

$$\exists \epsilon_{erbf} \ll, \in \mathbb{R}^+, \max_{t \geq 0} \left\| e_{rbf} \right\| \leq \epsilon_{erbf} \quad (19)$$

Theorem 1: Consider the system (10) under the assumption 1,2. If the controller gains are design such as:

$$K_1, K_2 > 0; \;\; K_3 > \epsilon_{erbf} \quad (20)$$

And the estimation of weight matrix is designed such as:

$$\dot{\widehat{W}} = \mu(e) e \quad (21)$$

Then the stability of the controller will be ensured, which lead to the tracking control error e will converge to zero exponentially.

Remark 2: This approach separates all unidentified factors and model parameters from the control signal, enabling us to develop the controller independently. A similar technique is described in [15]. It's important to mention that besides employing Neural Networks (NN) for handling unknown factors, another commonly utilized method involves using observers to estimate these unknown factors, as explained in [16-19].

Remark 3: The controller suggested in this study, as shown in Eq. (18) and Eq. (21), operates regardless of the model parameters. Consequently, it can be applied to various systems beyond just Internal Combustion Engine (ICE) systems.

The proof of this theorem will be given in the following equations. Let us define $\widetilde{W} = W - \widehat{W}$ and $\tilde{\delta} = \delta - \hat{\delta}$, from Eq. (17) and Eq. (18) one gets:

$$\tilde{\delta} = \widetilde{W} \mu(e) + e_{rbf} \quad (22)$$

Consider the follows Lyapunov function:

$$V = \frac{1}{2} J e^2 + \frac{1}{2} K_2 \left(\int e dt \right)^2 + \frac{1}{2} tr\left(\widetilde{W}^T \widetilde{W} \right) \quad (23)$$

From Eq. (13), Eq. (18), Eq. (21), Eq. (26) one gets:

$$\begin{aligned} \dot{V} &= e\left(-K_1 e - K_2 \int e dt - K_3 sign(e) + \delta - \hat{\delta} \right) \\ &\quad + K_2 e \int e dt - \; tr\left(\widetilde{W}^T \dot{\widehat{W}} \right) \\ &= e\left(-K_1 e - K_2 \int e dt - K_3 sign(e) + \widetilde{W} \mu(e) \right. \\ &\quad \left. + e_{rbf} \right) + K_2 e \int e dt \\ &\quad - \; tr\left(\widetilde{W}^T \mu(e) e \right) \end{aligned} \quad (24)$$

Taking into account the fact that $e\widetilde{W}\mu(e) - \; tr\left(\widetilde{W}^T \mu(e) e\right) = 0$. From (19) and (20) one gets: $e\left(e_{rbf} - K_3 sign(e)\right) \leq 0$. Hence, one can derive:

$$\dot{V} \leq -K_1 e^2 \leq 0 \quad (25)$$

3.2. Inner loop controller (Torque controller)

Based on the Eq. (6) to Eq. (8) we can derive the desired fuel mass flow rate as follows:

$$\dot{m}_{fuel} = \frac{\tau_{control} 2\pi N}{60 LHV \eta_{indicated}} \quad (26)$$

Based on Eq. (7), we can then determine the desired air mass flow rate as follows:

$$\dot{m}_{air} = \dot{m}_{fuel} AFR \quad (27)$$

Then the desired effect area is determined based on Eq. (2) as follows:

$$A_{eff} = \frac{\dot{m}_{air} \sqrt{R T_{upstr}}}{P_{upstr} \Psi(P_{ratio})} \quad (28)$$

Hence, based on Eq.(6), the desired open angle of throttle valve is given as:

$$\theta_{thr} = C_{thr}^{-1} \left(\frac{4 A_{eff}}{\pi {D_{thr}}^2} \right) \quad (29)$$

4. Results and Discussion

In this section, a simulation validation of our proposed controller will be carried out using MATLAB Simulink. The main goal of these simulations is to demonstrate the effectiveness of our controller in terms of handling the effect of the external unknown disturbances as well as the parametric uncertainties which may affect outer loop model. Then a comparison with the classic PID controller is considered The parameters of ICE using in this simulation is given in Table 1.

Table 1. Parameter of ICE.

Parameters	Values	Units
T_{upstr}	300	K
P_{upstr}	101325	Pa
R	287	J/(kg*K)
γ	1.4	-
D_{thr}	50	mm
S_{inj}	6.4516	mg/ms
LHV	47300000	J/kg
N_{cyl}	4	-
c_{ps}	2	rev/stroke

4.1. PID controller design

To design the PI controller for controlling the crankshaft dynamics, as governed by Eq. (10), we utilized pidtune provided by MATLAB. This tool facilitated the automatic tuning of the PI controller parameters, providing an optimized response for the system. Through this process, we ensured that the PI controller achieved the desired balance between stability, response time, and error minimization for the crankshaft control. The results PID tuner tool

gives the following results for the PI controller ($K_p = K_1 = 6.666$, $K_i = K_2 = 1.167$).

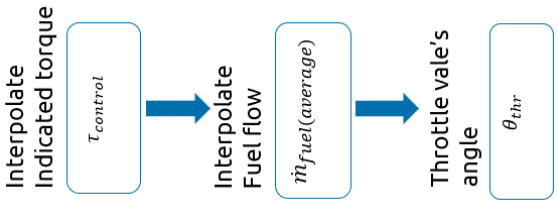

Figure 4. Torque control diagram.

4.2. Simulation results

The objective of this study is to analyze the speed tracking performance of the proposed controller in comparison to a conventional PID controller, particularly under the influence of disturbances. A combination of step and sinusoidal reference signal (Figure 5) were selected to evaluate the controller's performance across various dynamic conditions. The step signal simulates a sudden change in system demands, reflecting typical scenarios in real-world engine control systems where abrupt shifts in load or speed occur. In contrast, the sinusoidal component tests the controller's ability to track a continuously varying signal, mimicking situations where engine speed gradually fluctuates, such as during acceleration and deceleration cycles. This input aims to assess the system's robustness and adaptability under both steady-state and transient operating conditions. The engine's performance is evaluated under conditions of friction and external disturbances. Specifically, the friction effects impacting the engine are depicted in Figure 6, while the external disturbances, including factors such as environmental variations and load changes, are shown in Figure 7. These figures represent the challenges the controllers must overcome to maintain accurate speed tracking. The study aims to demonstrate the effectiveness of the proposed controller in managing these disturbances, ensuring superior speed tracking performance when compared to the traditional PID controller.

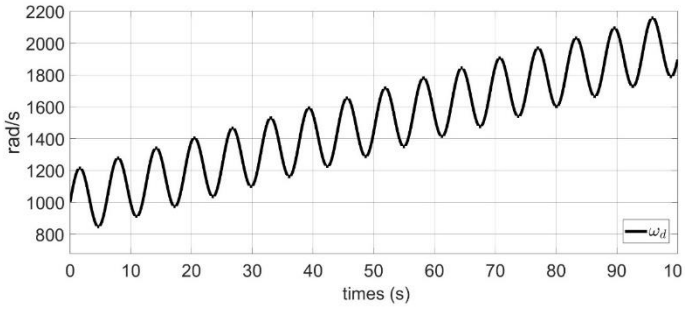

Figure 5. Desired value for controller design.

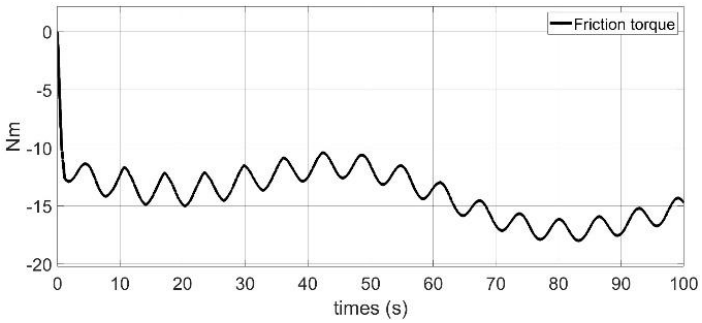

Figure 6. The friction affected to the system (10) during the simulation.

The tracking control performances of both the PID and the PID RBFNN, proposed in this study, are showcased in Figures 8 and 9. These figures demonstrate that all proposed controllers successfully fulfill the trajectory tracking task. However, a noticeable disparity emerges in the effectiveness between the PID and the proposed method. Specifically, the results from the PID exhibit less efficiency compared to the proposed approach. It becomes evident that the controller suggested in this study enables the maintenance of the ICE at the desired speed with a relatively minimal tracking error. This observation underscores the superior performance of the proposed method in ensuring precise speed control, highlighting its potential for enhancing operational stability and efficiency within the ICE system.

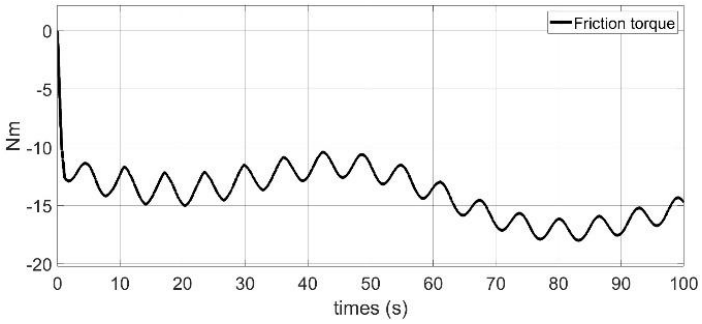

Figure 7: The external disturbance torque affected to the system (10) during the simulation.

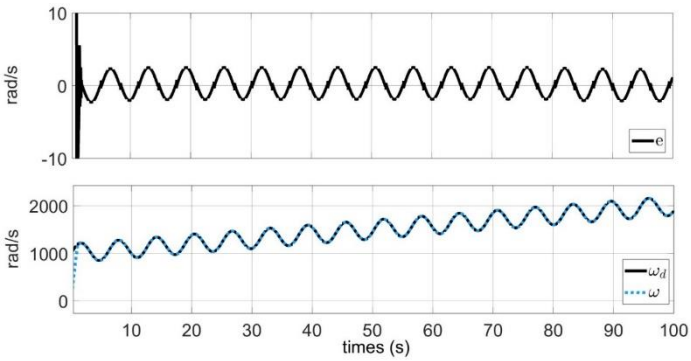

Figure 8: Simulation results for velocity tracking using RBFNN PID controller.

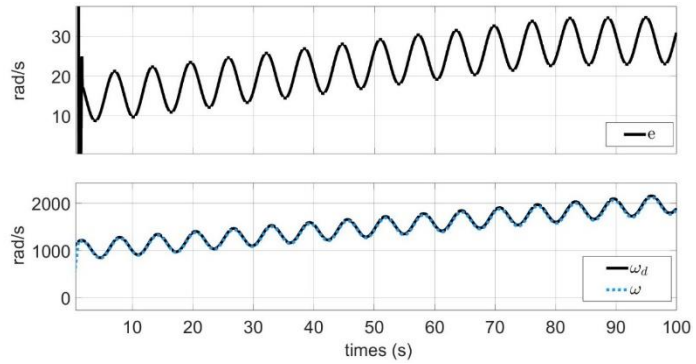

Figure 9. Simulation results for velocity tracking using classical PID controller.

Figure 10 illustrates the output torque of the Internal Combustion Engine (ICE) compared to its desired value derived from equation (18). This depiction showcases the effectiveness of our method in achieving precise torque control, ensuring consistency and accuracy in torque regulation. The close alignment between actual and desired torque values signifies the method's robustness. This precise torque control facilitates smooth speed tracking within the ICE system, enhancing operational efficiency and performance stability. Thus, Figure 10 serves as visual evidence of our method's ability to regulate torque output effectively, leading to improved speed tracking and overall system performance in ICE applications.

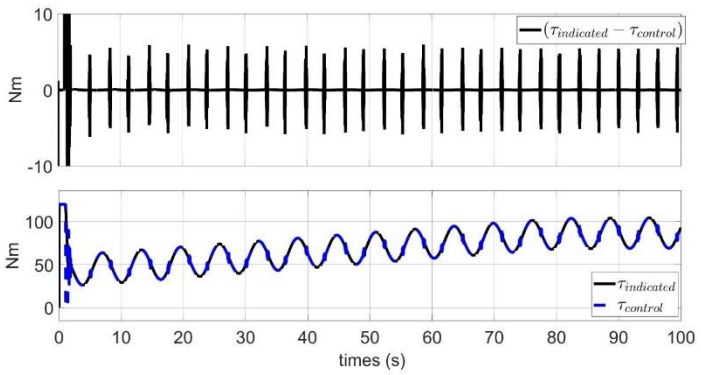

Figure 10. Engine torque and its desired value using RBFNN PID controller.

5. Conclusions

This paper proposed an adaptive controller for speed control on an ICE subject to bounded disturbances, model uncertainties and unknown parameters. The controller law is designed based on the PID technique. The unknown part is estimated using adaptive neural network using radius basic functional technique. The relevance of our proposed method, in terms of compensating the effects resulting from the disturbance, model uncertainties and unknown parameters, have been demonstrated through simulation results performed on the ICE system. To show the performance of our proposed observer, a comparison with the classic PID controller is conducted.

Acknowledgment

This work was carried out at Altran Prototypes Automobiles (APA) as a part of the Intelligence & Innovation Powertrain project within the Capgemini Engineering Research and Innovation Department.

Conflict of Interest Statement

Q-T.D and F.H contributed equally. All authors have given approval to the final version of the manuscript. The authors declare that there is no conflict of interest in the study. The authors would also like to thank Guillaume Guilbert who have contributed immensely for the part of the project.

CRediT Author Statement

Quang Truc Dam: Writing original draft & formal analysis - review & editing, supervision, project administration & validation. **Fatima Haidar:** Review & validation.

References

1. Ehsani, M., Gao, Y., Longo, S., & Ebrahimi, K. (2018). Modern electric, hybrid electric, and fuel cell vehicles (3rd ed.). CRC Press.
2. Stone, R. (1992). Introduction to internal combustion engines (2nd ed.). The Macmillan Press LTD.
3. Heywood, J. B. (2018). Internal combustion engine fundamentals (2nd ed.). McGraw-Hill Education.
4. Nise, N. S. (2015). Control systems engineering (7th ed.). Wiley.
5. Gao, D., Lei, Y., Zhu, H., & Ni, J. (2015). Constant speed control of four-stroke micro internal combustion swing engine. Chinese Journal of Mechanical Engineering, 28(5), 971–982. https://doi.org/10.3901/CJME.2015.0512.070
6. López, J. D., Espinosa, J. J., & Agudelo, J. R. (2011). LQR control for speed and torque of internal combustion engines. IFAC Proceedings Volumes, 44(1), 2230–2235. https://doi.org/10.3182/20110828-6-IT-1002.02176
7. Norouzi, A., Heidarifar, H., Shahbakhti, M., Koch, C. R., & Borhan, H. (2021). Model predictive control of internal combustion engines: A review and future directions. Energies, 14(19), 6251. https://doi.org/10.3390/en14196251
8. Gordon, D. C., et al. (2022). End-to-end deep neural network based nonlinear model predictive control: Experimental implementation on diesel engine emission control. Energies, 15(24), 9335. https://doi.org/10.3390/en15249335
9. Di Cairano, S., Doering, J., Kolmanovsky, I. V., & Hrovat, D. (2014). Model predictive control of engine speed during vehicle deceleration. IEEE Transactions on Control Systems Technology, 22(6), 2205–2217. https://doi.org/10.1109/TCST.2014.2309671
10. Norouzi, A., Heidarifar, H., Shahbakhti, M., Koch, C. R., & Borhan, H. (2021). Model predictive control of internal combustion engines: A review and future directions. Energies, 14(19), 6251. https://doi.org/10.3390/en14196251
11. Souder, J. S., & Hedrick, J. K. (2004). Adaptive sliding mode control of air–fuel ratio in internal combustion engines. International Journal of Robust & Nonlinear Control, 14(6), 525–541. https://doi.org/10.1002/rnc.901

12. Norouzi, A., et al. (2022). Deep learning-based model predictive control for compression ignition engines. arXiv preprint. https://doi.org/10.48550/ARXIV.2204.00139
13. Norouzi, A., Shahpouri, S., Gordon, D., Shahbakhti, M., & Koch, C. R. (2023). Safe deep reinforcement learning in diesel engine emission control. Proceedings of the Institution of Mechanical Engineers, Part I: Journal of Systems and Control Engineering, 237(8), 1440–1453. https://doi.org/10.1177/09596518231153445
14. Heywood, J. B. (1988). Internal combustion engine fundamentals. McGraw-Hill.
15. Dam, Q. T., Thabet, R. E. H., Ali, S. A., Guerin, F., & Tang, Y. (2023, September 27). Adaptive neural network-based sliding mode controller for trajectory tracking of a quadrotor UAV. TechRxiv. https://doi.org/10.36227/techrxiv.24174771.v1
16. Dam, Q. T., Thabet, R. E. H., Ali, S. A., Guérin, F., & Ghani, H. A. (2023). A high-gain observer design for nonlinear system with delayed measurements: Application to a quadrotor UAV. IFAC-PapersOnLine, 56(2), 6739–6744. https://doi.org/10.1016/j.ifacol.2023.10.379
17. Dam, Q. T., Thabet, R. E. H., Ali, S. A., & Guerin, F. (2024). Observer design for a class of uncertain nonlinear systems with sampled-delayed output using high-gain observer and low-pass filter: Application for a quadrotor UAV. IEEE Transactions on Industrial Electronics, 71(1), 933–942. https://doi.org/10.1109/TIE.2023.3247786
18. Dam, Q. T., Thabet, R. E. H., Ali, S. A., & Guerin, F. (2022, June). Filtered high-gain observer design for a class of nonlinear systems subject to delayed measurements: Application to a quadrotor UAV. 2022 American Control Conference (ACC), Atlanta, GA, USA. IEEE. https://doi.org/10.23919/ACC53348.2022.9867537
19. Dam, Q. T., Thabet, R. E. H., Ali, S. A., Guérin, F., & Hugo, A. (2021, June). Continuous–discrete time high gain observer design for state and unknown inputs estimations of quadrotor UAV. 2021 European Control Conference (ECC), Delft, Netherlands. IEEE. https://doi.org/10.23919/ECC54610.2021.9655232
20. Dam, Q. T., Haidar, F., Mama, N., & Chennapalli, S. J. (2024). Modeling and simulation of an internal combustion engine using hydrogen: A MATLAB implementation approach. Engineering Perspective, 4(3), 108–118. http://dx.doi.org/10.29228/eng.pers.76219